



K A U N O
TECHNOLOGIJOS
UNIVERSITETAS

2008

ISSN 1822-5721

MEDICAL PHYSICS in the BALTIC STATES

PROCEEDINGS OF THE 6th INTERNATIONAL
CONFERENCE ON *MEDICAL PHYSICS*

Kaunas, Lithuania
9-11 October, 2008



MEDICINOS FIZIKA



**LUND
UNIVERSITY**



**Lithuanian State Science and Studies
Foundation**

ISSN 1822-5721

KAUNAS UNIVERSITY OF TECHNOLOGY

MEDICAL PHYSICS IN THE BALTIC STATES

Proceedings of the 6th International Conference on Medical Physics

**Kaunas, Lithuania
9-11 October, 2008**

Executive editor: **D.Adlienė**

CONFERENCE IS ORGANIZED BY:

Kaunas University of Technology
Malmö University Hospital, Lund University
Society of Medical Physicists
Lithuanian Radiation Protection Centre
Kaunas Medical University Hospital

PROGRAM COMMITTEE

Diana ADLIENĖ - Kaunas University of Technology, *chairwoman*
Sören MATTSSON - Lund University, Malmö University Hospital, *chairman*
Ričardas ROTOMSKIS – Vilnius University
Albinas MASTAUSKAS – Lithuanian Radiation Protection Centre
Elona JUOZAITYTĖ – Medical University of Kaunas

ORGANIZING COMMITTEE

Lena ANCEVIČIENĖ – Kaunas University of Technology
Jurgita LAURIKAITIENĖ – Kaunas University of Technology

CONFERENCE IS SUPPORTED BY:

Lithuanian State Science and Studies Foundation
Kaunas University of Technology
Malmö University Hospital
Lithuanian Radiation Protection Society
JSC “Medicinos fizika”
JSC “LOKMIS”
JSC “Kodmeda”

Papers included in the Proceedings were referred by independent peer referees



Prof. Sören Mattsson
Lund University,
Malmö University Hospital/ Sweden

was inaugurated as

the Doctor Honoris Causa
of
Kaunas University of Technology

on 8 October 2008.

**Medical physicists society around the Baltic Sea
congratulates our professor with this award !**

Short introduction

Lars Johan Sören Mattsson was born on 3 October 1943 in Harplinge, Hallands län, Sweden

At present time he is professor of Medical Radiation Physics at Lund University and deputy head of the Department of Radiation Physics at Malmö University Hospital

Sören Mattsson started his scientific career during the aftermath of the superpowers' testing of large nuclear weapons in the atmosphere with a considerable global distribution and fall-out of radioactive material. He began by studying the transport of various radionuclides in the food chain: lichen-reindeer-man in northern Sweden. Together with ^{137}Cs and other frequently occurring products, he also could include some very rare radionuclides like ^{22}Na (using sum coincidence counting) and ^{155}Eu and other rarely occurring gamma-emitters (introducing Ge(Li)-gamma spectrometry for environmental samples). The interest for low-level gamma spectrometry, and photon spectrometry in general, led him into research related to x-ray fluorescence analysis applied *in vivo*. He pioneered the *in vivo* analysis of lead in bone (finger bone) and later the *in vivo* analysis of cadmium in kidney cortex. The same technique was later used for experimental studies of mercury in kidney cortex and of platinum (from the cytostatic agent cisplatin) *in vivo* in tumour tissue and in normal tissue in cancer patients. He also developed and used *in vivo* neutron activation analysis for the determination of total body and partial body protein (via nitrogen) of patients undergoing heavy surgery, radiotherapy or medical therapy.

In the field of clinical medical physics, it was natural for him to concentrate on nuclear medicine, scientifically starting with studies of radionuclide purity of radiopharmaceuticals. He initiated a number of new clinically oriented research projects, e.g. development of a new method for absolute determination of activity as well as depth of thrombi using the unique decay properties of ^{125}I (which was used to label fibrinogen taken up by the thrombi).

Becoming head of Medical physics department in Malmö and later professor and head of Medical physics department in Göteborg in 1983, he broadened his research into the optimal clinical use of x-rays (especially in paediatric radiology, mammography and bone imaging) as well as into radiation therapy by building up research groups in all areas of medical radiation physics, first in Göteborg and later in Malmö, to which he returned as professor and head of medical physics in 1988.

His current research interest concerns a continued interest for optimisation in medical x-ray imaging now in corporation with researchers at Kaunas University of Technology. He has a specific interest for digital technology and especially the development and testing of so called tomosyntes technique for low dose, 3D-imaging of breast and other organs and tissues. He has still an interest for radiation protection in general, including not only patients, but also personnel, and the general public. In the later field, projects related to the long-term variations of radioactive and stable elements in man and his environment is still going on. Examples are a number of ongoing projects related to the radiological consequences of releases from the nuclear industry as well as from the Chernobyl, a number of them in co-operation with researchers from Kaunas University of Technology. He is also currently developing new techniques for dosimetry in relation to radiation therapy (especially IMRT and proton therapy). Together with other research groups, he has pioneered the biomedical use of accelerator mass spectrometry for low level counting of ^{14}C for kinetic and dosimetric studies, including so called microdosing of pharmaceutical candidates, and recently for the determination of the age of specific cells using the “bomb-pulse technology”. The continued work related to the estimation of dose to patients from radiopharmaceuticals is still an important project with a considerable international interest and impact.

Sören Mattsson was awarded with:

Erna Ebeling Award of the Swedish Society of Medicine in 1992 for “an important research regarding radiation and radioactive substances in man and his environment as well as for an important development of new measurement technology and diagnostic methods for radioactive tracers and x-rays”;

Bo Lindell Award (“Mark of Honour”) of the Nordic Society for Radiation Protection in 2003. The Bo Lindell Award is every 3rd year given to “a person, who the Society wants to acknowledge for his/her great merits within radiation protection demonstrated through many years promotion of radiation protection theoretically and/or practically or in other ways significantly has promoted the aim of the Society”.

CONFERENCE PROGRAM

Thursday, 9 October 2008

RADIOLOGY SEMINAR

Šiauliai Regional Hospital, Darželio g. 10, Šiauliai

- 11.00-13.00** *David Sjöström* (Copenhagen University Hospital, Denmark). Acceptance, Commissioning and QA in Radiotherapy - Experiences from Herlev
Sören Mattsson (Lund University, Malmö University Hospital, Sweden). Protonen therapy
Diana Adlienė (Kauno Technologijos Universitetas, Lithuania). Patient's dosimetry during mammography screening in Lithuania: investigation results and problems
Darius Mikšys (JSC "LOKMIS", Lithuania). Products for radiation protection and monitoring

Friday, 10 October 2008

- 09.00-10.00** Registration of participants at Kaunas University of Technology
Studentų g. 50–325F, Kaunas
- 10.00-10.15** Opening of the conference. *Rymantas Kažys*, Vice Rector of Kaunas University of Technology, *Vytautas Janilionis*, Dean of the Faculty of Fundamental Sciences; *Sören Mattsson*, Lund University, Malmö University Hospital, *Diana Adlienė*, Kaunas University of Technology

Session 1, Chair: prof. Diana Adlienė

- 10.15-11.00** *S. Mattsson and D. Adlienė*. Current development and future of medical physics
11.00-11.15 *D. Kaškelytė, A. Čiburys, S. Bagdonas, G. Streckytė, R. Rotomskis and R. Gadonas*. Fiber-optics based laser system for 2-D fluorescence detection and optical biopsy
11.15-11.30 *V. Kulvietis, I. Janutytė, S. Bagdonas, V. Karabanovas, R. Rotomskis*. Effect of medium pH on stability of quantum dots: spectroscopic study and biological implications

Coffee break 11.30-12.00

- 12.00-12.15.** *J. Puišo, J. Laurikaitienė, A. Guobienė, D. Adlienė, I. Prosyčėvas*. Silver nanoparticles for gamma dosimetry
12.15-12.30 *V. Poderys, V. Jašinskas, R. Žemaitienė, R. Rotomskis*. Artificial intraocular lenses surface investigation by atomic force microscope
12.30-12.45 *Yu. Dekhtyar, M. Romanova*. ZrO₂ glass films influenced by ultraviolet radiation
12.45-13.00 *V. Punys, M. Zikas*. Grey scale measurements of video displays

Time for the lunch 13.00 – 14.00

Session 2. Chair: prof. Sören Mattsson

- 14.00-14.30** *K. Stenström*. Nuclear weapon-produced ^{14}C – applications and limitations of bomb-pulse dating
- 14.30-14.45** *R. Druteikienė, B. Lukšienė*. Chemical speciation of plutonium and its environmental fate
- 14.45-15.00** *G.A. Adlys*. Radiotoxicity of nuclear fuel
- 15.00-15.30** *H. Uusijärvi, M. Sydoff, M. Söderberg, S. Leide-Svegborn, S. Mattsson*. Optimising PET/CT and SPECT/CT investigations. The MADEIRA project
- 15.30-15.50** *L. Johansson*. Experiences from planning of a cyclotron and a PET/CT-unit

Coffee break 15.50-16.20

Session 3. Chair: Anatoli Vladimirov

- 16.20-16.50** *H. Nyström*. Skandionkliniken: the Swedish centre for proton therapy
- 16.50-17.10** *A. Katashev, A. Meijers and S. Popov*. Use of the laser beam for markerless tracking of the patient breathing motion for respiratory gated radiotherapy
- 17.10-17.30** *S. Plaude, A. Meijers, S. Popov, A. Miller and Yu. Dekhtyar*. The impact of the detector size effects in regions of high dose gradients on point dose measurements.
- 17.30-17.45** *V. Andrijaitienė, D. Adlienė*. Possible application of verification methods in gamma therapy

19.00-22.00 Get-together party
“Perkūnas House“, Aleksoto g. 6, Kaunas

Saturday, 11 October 2008

08.30-09.30 Registration of participants at Kaunas University of Technology
Studentų g.50-325F, Kaunas

Session 4. Chair: dr. Judita Puišo

- 09.30-10.00** *I. Pruul, A. Vladimirov, K. Kepler*. Image quality assurance of medical LCD displays based on AAPM TG 18 acceptance protocol
- 10.00-10.15** *J. Kepler, K. Kepler*. Comparison of quality control methods in computed tomography and adaptation for testing laboratory
- 10.15-10.30** *J. Žiliukas, L. Krynkė, D. Adlienė*. Evaluation of patient doses in CT examinations
- 10.30-11.45** *P. Gabrilevičius, M. Laurikaitis*. Stability check of X-ray therapy unit: from the fifties up to to-days use
- 10.45-11.00** *E. Skripkaitė, J. Laurikaitienė, G.A. Adlys*. Comparison of calibration methods in nuclear medicine
- 11.00-11.15** *V. Minialga*. Light radiation parameters of commonly used high intensity light emitting diodes

11.15-11.30 Final remarks by Sören Mattsson

Coffee 11.30-12.00

MAMMOGRAPHY SEMINAR

Saturday, 11 October 2008

National mammography screening program: gathered experience

- 11.30-12.00** Registration to the seminar at Kaunas University of Technology
Studentų g. 50- 325F, Faculty of Fundamental Sciences
- 12.00-12.10** Introduction. ***Representatives of Association of Radiologists, Lithuanian Radiation Protection Society and Society of Medical Physicists***
- 12.10-12.40** ***J.Kurtinaitis***. Atrankinės mamografinės patikros įtaka krūties vėžio išaiškinamumo rodikliams (The impact of mammography screening on the evaluation of breast cancer)
- 12.40-13.10** ***D.Bartuškaitė***. Atrankinės mamografinės patikros dėl krūties vėžio programa: gydytojo radiologo požiūris (Mammography screening program – a view of radiologist)
- 13.10-13.40** ***I.Cibulskaitė, D.Adlienė***. Pacientų dozės atrankinių mamografijos patikrų metu: rezultatai ir problemos (Patient's doses during mammography screening examinations: results and problems)
- 13.40-14.00** ***J.Žiliukas***. Radiacinės saugos aspektai mamografinių tyrimų metu (Aspects of radiation protection in mammography screening)
- 14.00** **Discussions**

CURRENT DEVELOPMENT AND FUTURE OF MEDICAL PHYSICS

Sören MATTSSON*, Diana ADLIENĖ**

* Medical Radiation Physics, Malmö University Hospital and Lund University, Malmö, Sweden;

** Department of Physics, Kaunas University of Technology, Kaunas, Lithuania

Abstract: Medical physics is a branch of applied physics. It uses concepts and methods of physics to help diagnose and treat human disease. Medical physics plays an essential role in medical imaging, radiation therapy of cancer and in radiation protection.

Medical imaging, which is a prerequisite for all modern hospital and health care, is today one of the fastest growing areas in medicine, exemplified by CT-, MR- and PET-imaging for anatomical, functional and molecular information.

Radiation therapy is unique among the cancer treatment modalities because it can be modulated in space and in time (4D). Spatial modulation will be facilitated by recent technological advances in image guided treatment planning and delivery to be optimised for the individual patient.

Radiation protection involves the protection of patients as well as of occupationally exposed persons in all areas of society as well as of the general public. Radiation protection has many things in common with X-ray imaging, nuclear medicine and radiation therapy: basic physics and technology, radiobiology, radiation detection and dosimetry, risk considerations and information.

The future of medical physics is dependent on cutting-edge innovations in physics and technology. It is also highly related to the future of medicine and its research challenges. This means that medical physics has to go into individualisation of therapy (incorporation of biological information, early treatment response assessment), combination therapies, translational research and simulations of complex systems (like tumour and vascularisation and response to therapies).

Keywords: medical physics, development, future, imaging, radiation therapy, radiation protection, multidisciplinary work, CPD.

1. Introduction

Medical physics is a branch of applied physics. It uses concepts and methods of physics to help diagnose, treat and prevent disease [1]. Some medical physicists develop cutting-edge technologies in the physics laboratory, while others are clinically working professionals who apply these technologies in the clinic and help diagnose and treat disease. They ensure the safety of a large number of patients, occupationally exposed persons and the general public.

2. Medical imaging

Medical imaging is together with molecular medicine among the fastest growing areas within medicine. It covers a number of techniques such as computed tomography (CT), magnetic resonance imaging (MRI), ultrasound (US), nuclear medicine (NM) including positron emission tomography (PET) and single photon tomography (SPECT) and several methods in optical imaging. Traditionally, and most often also today,

medical imaging is used for noninvasive mapping of anatomy and for detection and localisation of a disease. However, the new medical imaging techniques (PET/CT, SPECT/CT, MRI, PET/MRI, ultrasound) produce important biological information about physiology, organ function, biochemistry, metabolism, molecular biology and even functional genomics. These new methods can combine the ability to measure and quantify biological processes with the ability to localise the measured parameter in a high quality anatomical image [2]. Furthermore, advanced imaging techniques have developed into advanced methods for treatment as an alternative to surgery: e.g. coronary angioplasty, and treatment of aortic and cerebral aneurysms.

Medical imaging research has a crucial role to play in the development of better and more personalised care with the important benefits of being non-invasive and offering whole-body anatomical information and co-localisation of the disease process and the relevant biological measurements.

The important and exciting progress in biotechnology, nanomedicine and new innovative therapies is highly dependent on integration with medical imaging for successful application into clinical practice [2].

3. Radiation therapy

Accurate target delineation and image guidance are essential for precision radiation therapy. Developments in multimodality and 4D imaging techniques, as described above, provide opportunities to improve tumour localisation as well as improved tumour and normal tissue delineation. They are extremely helpful in dose planning and contributes to reduce set up variations and treatment margins. Proper use of these technologies can provide sparing dose to normal tissue and permit safer escalation of tumour doses [3].

IMRT

Technical developments in the form of inverse treatment planning and dynamic multi-leaf collimation systems have given radiotherapy the ability to deliver conformal and intensity-modulated radiotherapy (IMRT). A computer-controlled linear accelerator sweeps a narrow slit of radiation across the tumor from five to nine angles around the patient, one angle at a time. Clinical implementation of IMRT, especially image-guided IMRT, is in a state of rapid evolution. Linac based CT systems and applications of megavoltage (MV) imaging systems have opened new possibilities for improved radiation therapy. A new variant of the so-called volumetric modulated arc therapy (VMAT) technique, involving IMRT delivery during gantry rotations, has recently been introduced. The novel technique Rapid ArcTM promises further benefit to patients by offering the same treatment in half the time. The dose is delivered over a single gantry rotation with dynamically varying MLC-positions, dose rate and gantry speed. The technique is expected to have advantages in sparing normal tissue compared to multi-field IMRT. Helical TomoTherapy®, one of the latest steps in this development, is an IMRT technique whose design is based on beam angle optimization and MVCT-based delivery verification. The technique has the potential to permit full clinical development of adaptive radiotherapy and conformal avoidance.

Respiratory gating

For targets in the thoracic and abdominal regions, the organ motion due to breathing limits the precision of radiotherapy. Field sizes must be sufficiently large to include tumour motion and this means a limitation in the dose that can be delivered. Respiratory-gated beam delivery is intended to limit the irradiation to selected parts of the respiratory cycle, and thereby enable reduction of the required treatment field margins. Treatments of breast cancer, lung and liver tumours are examples where respiratory gating is an advantage.

Proton therapy, IMPT

The major advantage of proton treatment over conventional radiation is that the energy of protons can be directed and deposited in tumour volumes in a three-dimensional pattern from each beam used. In this way the dose to the tumour can be increased while reducing the dose to surrounding normal tissues. The ultimate goal is to do fully automated three-dimensional intensity modulated proton therapy (IMPT). This allows the dose to be increased beyond that which less-conformal radiation will allow. The overall effect potentially leads to fewer harmful side effects, more direct impact on the tumor, and increased tumor control.

New accelerator developments

Protons are normally accelerated in cyclotrons or synchrotrons. A novel compact IMPT system is now under development [4]. The basis of the design is the dielectric wall accelerator (DWA) system being developed at the Lawrence Livermore National Laboratory. The DWA uses fast switched high voltage transmission lines to generate pulsed electric fields on the inside of a high gradient insulating acceleration tube. High electric field gradients are achieved by the use of alternating insulators and conductors and short pulse times. The system will produce individual pulses that can be varied in intensity, energy and spot width. The system can be sited in a conventional linac vault and provide intensity modulated rotational therapy. The IMPT planning system will optimize delivery characteristics.

In the longer time perspective, the possibility for laser acceleration of charged particles might be a way to construct an ultra-compact accelerator system. This is a technology that is radically different from the conventional accelerator-based approach. It reduces the overall system size and weight by more than one order of magnitude. The characteristics of the particle beams (protons) make them suitable for a class of therapy that might not be possible with the conventional accelerator, such as the ease for changing pulse intensity, the focus spread, and the dose delivery in general.

Biological modelling

Some of the major impacts in radiation therapy will come from biological modelling and new fractionation schemes [3]. Dose escalation may improve the local control. Boosting most of the target may significantly increase tumour control probability for a small increase in risk of necrosis where a substantial proportion of the target volume can be boosted [3].

For the future, Bentzen [5] proposes that radiation therapy is optimized through personalized prescriptions of the 4D dose distribution using molecular risk profiling and functional imaging, a method that he calls theragnostic radiation oncology. The aim is to provide the clinical basis for rational prescription of non-uniform dose distributions in individual patients. Molecular risk profiling will be directly linked to research related to the outcome of the treatment, mainly based on data from clinical trials, which are based on

high-quality dosimetric and clinical outcome data. Most work so far, has been based on immunohistochemical markers or DNA gene expression arrays, but is expanding into proteomics and metabolomics.

In the future, it will also be important to try to model the effects and outcome of a specific treatment. Bioeffect modelling includes the modelling of dose-response relationships, linear-quadratic time-dose-fractionation models and normal tissue complication probability (NTCP)/tumor control probability (TCP) models. It will also be important to continue to design, conduct, analyse and interpret randomized controlled trials.

The fact that substantial research efforts into predictive radiation oncology so far have produced very little in terms of clinically applicable assays may change with the development of novel high-throughput assays that are of potential interest in a radiation oncology [5].

Examples of assays, which show promise in radiation oncology applications are single nucleotide polymorphisms, immunohistochemical markers, and DNA microarray gene signatures. Some recent studies suggest a differential treatment response between tumor stem cells and other tumor cells. If this is a general pattern, then future predictive assays may have to be performed on stem cells rather than on unselected tumor cells.

4. Radiation protection

Both natural and man-made sources of ionising radiation contribute to human exposure and poses a risk to human health [6]. Exposure of the population to natural radiation is to some extent unavoidable and medical use of radiation is now an indispensable part of modern healthcare. The exposure of workers, and to a smaller extent of the public, to low levels of radiation from nuclear energy production and other industrial uses of ionising radiation have become an integral part of our society. These uses are heavily regulated. Radiation protection standards rely on current knowledge of the risks from radiation exposure. Any over-, or under-, estimation of these risks could lead either to unnecessary restriction or to a lower level of health protection than intended.

Protection in medicine

Medical procedures represent the largest source of human-made radiation exposures. There are 2 000 million medical x-ray investigations and 300 million dental x-ray investigations made each year in the world. Most of them (3/4 and 9/10 respectively) are carried out on 1/4 of the world's population (for which the medical investigations give an effective dose per capita of 1.2 mSv/year). On top of that there are 32 million investigations in diagnostic nuclear medicine and 5.5 million treatments per year in radiation therapy. In our part of the world, there has been a dramatic change of CT-investigations (more procedures, more scans per procedure). Today CT accounts for around 5-15% of the investigations but gives rise to dominating contribution to the collective dose from diagnostic radiology. Interventional procedures, increasingly being used to

replace surgery, can lead to very high local skin doses, in some cases exceeding the threshold for deterministic effects. For most X-ray examinations, there are still too large inter-hospital variations in doses for the same type of examination. On the other hand, the development in mammography (in many countries used for repeated breast cancer screening) shows how real improvements can be done. The average glandular dose has been reduced from 100 mGy (3 projections) in the 1970's with direct film to 1 mGy as a standard today (screen/film or digital) and a potential for 0.4-0.6 mGy with the most recent digital technique.

The different imaging and treatment modalities present a number of potential hazards for the patient and the environment. The problem with ionizing radiation in x-ray and nuclear medicine investigations is well known and needs to be continuously followed. There are also concerns about potential hazards from magnetic resonance imaging when moving to higher field strengths and from ultrasound when moving to higher frequencies and intensities.

Care for the personnel in radiology was the start of radiation protection. Today there are 2.7 million occupationally exposed persons of which 3/4 works in the health care sector. The doses are very low in diagnostic radiology, somewhat higher in nuclear medicine and still somewhat higher at nuclear power stations. For personal dosimetry, there are some remaining dosimetric problems related to the weighting of the neutron components in reactor environments, at waste handling and at high-energy accelerators for radiotherapy and physics research.

Radiation protection in a broader perspective

The field of radiation protection is broad [6]. The scientific basis is, however, the same: basic radiobiology, radiation detection and dosimetry, risk considerations and need to inform other people. It might also be helpful when we form our own views on radiation protection if we can refer and compare to other areas than our own.

The protection of man will continue to dominate our efforts with a priority for the youngest individuals (including embryo and fetuses), which we believe are the most sensitive to radiation. Today we are around 6 000 million people in the world. Our natural exposure gives an effective dose of 2.4 mSv per capita, the main sources being cosmic radiation, terrestrial gamma rays, ingestion of naturally occurring radionuclides (⁴⁰K) and radon daughters in indoor air. Seen on a global scale, we can hardly change that value much, just locally try to reduce the highest exposures. With increasing standard of living, man-made radiation sources such as radiation in medicine, releases from nuclear industries, high-level waste, consumer products and accidents will play an increasing role. All of us do still have reasons to be afraid of the military use of nuclear weapons. The risk that nonnational groups or individuals use primitive nuclear weapons or "dirty bombs" has become real today and we cannot neglect the risk for new large reactor accidents. It is necessary to continue the efforts to improve our preparedness for all these situations.

Up to now the radiation protection criteria have been based on minimising the risk to humans. Today, the efforts are closely related to the discussion about a sustainable environment which most of us welcome. It is a challenge to obtain tools to assess and evaluate long-term consequences of radiation exposure to the whole biosphere. Today much work is going on to define a limited set of reference organisms with their relevant reference dose models and data sets. We have to realise that this is a real long term project, with many parallels to the development of a “standard man”, standard human biokinetic models and dose catalogues for man which have been done during the last 30 years.

5. Challenges in research

For success in research in medical physics it is necessary to create true multi- and interdisciplinary research environments and/or network where physicists, physicians, physiologists, chemists, mathematicians, molecular biologists, computer scientists and other technologists and technicians work closely together on the same research projects [7]. These challenges can only be overcome through close collaboration between universities and major research centres to obtain a wide range of high-level competence, to achieve a research environment of sufficient size and to obtain the necessary funding for infrastructure and large research projects.

A particular challenge is to achieve an increased collaboration between imaging specialists (radiologists, nuclear medicine physicians, medical physicists) and the clinicians with knowledge of different organ systems and diseases. The clinicians also know the special needs of imaging in relation to the disease areas they specialise in and the workflow in clinical departments. Traditionally, medical imaging has been an activity where an imaging specialist makes a well-founded evaluation of the patient's disease, based on visual inspection of a limited number of images. However, we now see an exponential increase in the number of images acquired for each patient and the possibility of using the images as raw data for quantification in order to measure relevant parameters describing organ function, physiology and molecular biology. Medical imaging research must address these changes through focusing on Information and Communication Technology solutions for decision support for radiologists, nuclear medicine physicians and other physicians, and also focusing on improved quantification of imaging results and biomarkers. The latter is also important for longitudinal follow-up of patients and comparison of results between centres in multicentre clinical trials.

In the field of radiation protection, there has been a decline in research capacity during the last decades, but the increasing application of ionising radiation in medicine and plans to establish new nuclear plants now accentuate the need to revitalise the field [8]. There is now an increasing awareness that many countries have lost key competences and are no longer capable of independently retaining their current research activities

in radiation sciences, with implications for effectively fulfilling operational and policy needs and obligations.

6. Challenges in learning and teaching

In the past, the rate of change was low and a qualified individual became so for life. To meet today's needs and obligations, we need to continuously maintain our training and education. There is a need for an educational initiative for continuous personal development (CPD), an activity designed to enhance knowledge, skills, attitudes and competences required for the clinical and practical work. It needs to be documented and have measurable outcomes. Moreover, currently all scientific fields, in the same way as medical physics – are approaching a multidisciplinary paradigm. In order to keep up with the development of any field, an individual has to learn the latest changes in technology, imaging sciences, algorithm design, computing techniques, cell and molecular biology etc.

7. Summary

Medical physics is at the forefront of the development of the dynamic field of medical imaging. Medical physics is pioneering the radiation oncology of the future. Medical physics ensure the safety of a large number of patients, occupationally exposed persons and the general public.

8. References

1. Mattsson S, Adliene D. The role of medical physicist in health care and radiation protection. *Sveikatos mokslai* 2(33), 41-43, 2004, ISSN 1392-6373
2. Brunetti A., Cuocolo A. European science foundation calls for more and better medical imaging research. *Eur J Nucl Med Mol Imaging* 35, 1749–1757, 2008
3. Paliwal B. Medical physics practice in the next decade. *J. Med. Phys.* 31(3), 98-108, 2006
4. Caporaso G J, Mackie T R, Sampayan S et al. A compact linac for intensity modulated proton therapy based on a dielectric wall accelerator. *Physica Medica* 24, 98-101, 2008
5. Bentzen S. M. From cellular to high-throughput predictive assays in radiation oncology: Challenges and opportunities. *Semin Radiat Oncol* 18, 75-88, 2008
6. Mattsson S. The Bo Lindell Lecture. Radiation protection among populations, patients, personnel, plankton and plants – What can we learn from one another? In: Paile W. (Ed.). *Radiation Protection in the 2000S – Theory and Practice*. Nordic Society for Radiation Protection. STUK-A195, Vantaa 2003, pp. 16-22
7. Jeraj R. The future of physics in medicine and biology. Lecture at the Nordic Association for Clinical Physics NACP2008 Symposium, Aarhus, Denmark June 4-5 2008
8. HLEG. Draft Report of High Level Expert Group of European Low Dose Risk Research, 8 September 2008 (<http://www.hleg.de/dr.pdf>)

FIBER-OPTICS BASED LASER SYSTEM FOR 2-D FLUORESCENCE DETECTION AND OPTICAL BIOPSY

Dalia KAŠKELYTĖ*, Arūnas ČIBURYS*, Saulius BAGDONAS*, Giedrė STRECKYTĖ*,
Ričardas ROTOMSKIS**, Roaldas GADONAS*

* Department of Quantum Electronics & Laser Research Center, Vilnius University, Saulėtekio al. 9, c. 3, LT-10222
Vilnius, Lithuania;

** Laboratory of Biomedical Physics, Institute of Oncology of Vilnius University, P. Baublio g. 3, LT-08406 Vilnius,
Lithuania

Abstract: A fiber-optics based laser system design for depth probing measurements of the fluorescence of green fluorescence protein (GFP) marked biological objects is described. A model layered system consisting of rhodamine G6 gelatin-milk slice inserted between chicken breast tissue slices was used to characterize the performance of the constructed system. Localization of the 3 mm thickness fluorescing slice was evaluated with the probe needle tip by registration of fluorescence spectra at various probing depth.

Keywords: fluorescence, fiber-optic probe.

1. Introduction

There are many fields in biomedicine where fiber based optical probes are used for fluorescence diagnostics and imaging purposes (1-2). Fluorescence probes that can collect and distinguish depth-related spectroscopic information representing tissue optical signatures from native chromophores or used molecular markers have important diagnostic significance. Knowledge of the localization and distribution of fluorescing substance within the biological tissue as well as its specific optical signatures may improve the ability of fiber-optic spectroscopy to evaluate biochemical alterations or tissue viability during the real-time measurements.

The goal of this work was to construct the experimental fiber-optics based laser system, which is sensitive to the labeled object localized within tissue (cells) volume of about a few cubic millimetres. The premises of the present work deal with the problem of the detection of genetically modified cell lines labeled by fluorescent marker, green fluorescing protein (GFP), in heart tissue, which could confirm their survival and successful integration leading to possible regeneration of heart structures.

2. Materials and methods

We used cw diode-pumped solid state laser (DPSSL) operating at the wavelength 473 nm with tunable output power up to 15 mW for fluorescence excitation of

molecular markers inoculated into biological tissue. A spectrometer (Avaspec-2048, Avantes, Inc.) was used to register the fluorescence spectra detected at the given probing depth within the sample. The laser light and fluorescence registration are all coupled to fiber optics for guiding light into the sample and out of it. The structural arrangement of fluorescence excitation / collection unit is presented in Fig. 1.



Fig. 1. Set-up of constructed fiber-optics based laser system

Fluorescence excitation / collection unit set-up was specifically designed to perform fluorescence measurements in heart tissue based on GFP signal detection.

The performance of the fiber-optics based laser system is realized through the following steps: laser light is directed to the fluorescence excitation / collection guiding optical unit with the mirror (M). The excitation

light passes the excitation filter (F1) and being reflected from dichroic beamsplitter (DBS) is focused by the coupling lens (CL1) to the fluorescence excitation / collection optical fiber probe with the coupling effectiveness of about 92 %. The excitation and the collection of the fluorescence signal are realized through the same optical fiber (200 μm in diameter), the tip of which is specifically modified by inserting it into the 22 gauge needle thus enabling to prick the tissue sample for the detection of the fluorescence signal at different probing depths (Fig. 2).

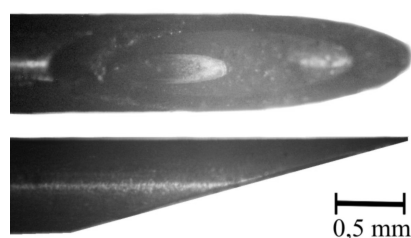


Fig. 2. Scheme of fluorescence collecting fiber tip inserted into the needle. The fiber probe tip is polished to form elliptical geometry with the active zone of about 0.5 mm along the x axis.

Fluorescence signals collected inside the biological tissue are guided back with the same fiber to the fluorescence excitation / collection optical unit, where spectral discrimination between the fluorescence signal and the fluorescence excitation light is realized by dichroic beamsplitter (DBS) and fluorescence cut-off filter (F2). The collection lens (CL2) focuses the fluorescence light into the optical fiber (200 μm in diameter) and guides the signal to the spectrometer. We used Brightline laser fluorescence LF488-A filter set (Semrock, Inc.) to ensure collection of GFP fluorescence signal in the spectral range from 500 nm to 545 nm (Fig.3).

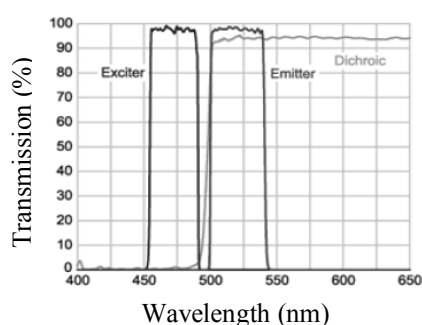


Fig. 3. Transmission characteristics of the Brightline laser fluorescence LF488-A filter set

In our work we measured the fluorescence intensity values by changing the inner position of the optical fiber probe in model system. We used chicken breast tissue and slices of gelatin (thickness was about 3 mm) containing rhodamine 6G with couple drops of milk as experimental layered system to detect the fluorescence of the marked object within the tissue. The data obtained by changing fiber probe's depth in the sample were used to construct 2D fluorescence intensity plots to

determine sensitivity of the fluorescence excitation / collection unit.

3. Results

The fluorescence intensity values of rhodamine 6G in gelatin layer were collected automatically by changing the depth of fiber probe within the sample every 0,7 mm. The sensitivity of the designed system during the measurements was sufficiently high to register the changes in the fluorescence signal of the marker while fiber probe was gradually moved from one tissue layer to the next deeper laying layer. Fig.4 shows the fluorescence intensity of rhodamine 6G collected by passing the needle fiber tip through the model layered sample, which is plotted as a depth and wavelength function. The measurements indicate that the fiber-optic probe collects information about the localization of the rhodamine 6G layer.

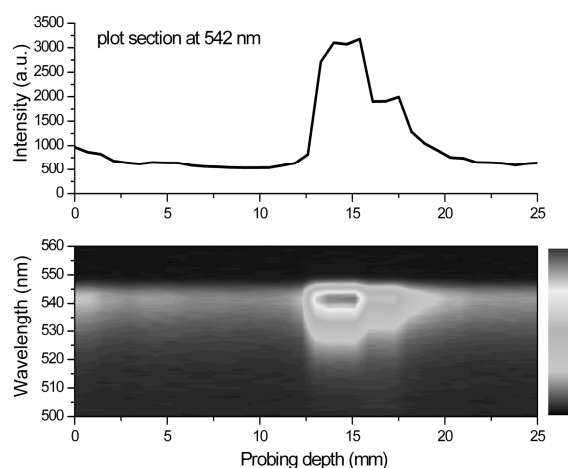


Fig. 4. Set of fluorescence intensity of rhodamine 6G marker layer collected at different fiber tip probing depths (bottom plot). Fluorescing rhodamine 6G – gelatin–milk layer (3 mm thickness) has been covered with the 13 mm thick slice of breast tissue. Upper plot represents distribution of the fluorescence intensity of the marker at 542 nm emission wavelength along the layered specimen.

Slight increase in the background fluorescence signal measured under the fluorescing layer was observed. It can be explained as a result of slight staining of the needle fiber tip caused by the rhodamine 6G, attached to it from the marked layer. The increased background fluorescence signal vanishes moving the needle deeper into the sample for about 2 mm.

4. Conclusions

The constructed fiber-optics based laser system could provide the real-time monitoring of fluorescing objects in biological tissue at various probing depths. The demonstrated ability to target accurately the position of the fluorescing rhodamine 6G gelatin-milk layer may improve the performance of fiber-probe fluorescence spectroscopy based equipment as a diagnostic tool for tracking GFP labeled stem cells in heart tissue.

5. Acknowledgements

This study has been supported by the Lithuanian State Science and Studies Foundation, the grant No. B-07041.

6. References

1. Utzinger U., Richards-Kortum R.. Fiber optic probes for biomedical optical spectroscopy. *J. Bio. Opt.* 8, 121-147, 2003.
2. Pfefer T.J., Schomacker K.T. etc. Light Propagation in tissue during fluorescence spectroscopy with single-fiber probes. *IEEE J. Select. Top. Quant. Electr.* 7(6), 1004-1012, 2001.

**EFFECT OF MEDIUM pH ON STABILITY OF QUANTUM DOTS:
SPECTROSCOPIC STUDY AND BIOLOGICAL IMPLICATIONS**

Vytautas KULVIETIS*, Ilma JANUTYTĖ**, Saulius BAGDONAS**, Vitalijus KARABANOVAS***,
Ričardas ROTOMSKIS***

* Laboratory of Biomedical Physics, Institute of Oncology of Vilnius University. P. Baublio g. 3, LT-08406 Vilnius, Lithuania;

** Laser Research Center, Vilnius University. Saulėtekio al. 9, c.3, LT-10222 Vilnius, Lithuania

Abstract: Some questions about quantum dots (QDs) stability in different media and effects on biological systems remain unrevealed. We investigated CdTe QDs stability dependence on medium pH using spectroscopic methods. The cytotoxicity of the particles was investigated on the osteosarcoma cells by means of a confocal microscope as well. Results show that CdTe QDs degrade in the acidic medium very fast, but demonstrate temporarily stability in higher pH solutions. The particles are toxic to living cells, which can be related to the release of heavy ions.

1. Introduction

Quantum dots (QDs) are photostable, bright fluorophores exhibiting optical properties, which are superior to the most organic dyes. They have high quantum yields, narrow photoluminescence emission bands, high absorbance and very broad effective Stokes shift. These particles have fluorescence maximum position, which depends on their size and, therefore, it can be easily tuneable. Thus, QDs of several different emission colours can be excited using a single wavelength for excitation [1]. More to add, they are easy to modify and functionalize for their applications in the biomedicine.

However, their stability and toxicity in living systems play a major role when determining if these particles can be used to label, identify, specify or even treat biological system effectively without disturbing its activity [2]. Those features are mainly determined by the chemical composition and charge of molecules forming superficial covering of QDs. Different external factors and interactions with surrounding environment may alter the physicochemical properties of the outer layer. Consequently, the behaviour of the particles in biosystems becomes more complex and more difficult to predict.

Nowadays this problem is not solved yet. One of the reasons is the wide range of available QDs as well as the variety and complexity of the surface composition. On the other hand, these particles are applied for different biological needs, each of which is specialized

and, therefore, it becomes difficult to compare the results from different experiments [3-5].

Changes in physicochemical properties of QDs are reflected in their absorption and fluorescence spectra and can be studied using various spectroscopic methods. For instance, QDs stability can be monitored by the following fluorescence spectra parameters: the maximum peak position, the maximum peak intensity and the spectral width of the band [6,7].

The effect of the aqueous medium pH on the physicochemical properties of water soluble CdTe QDs was spectroscopically evaluated in the present study.

2. Materials and methods

CdTe quantum dots (fluorescence $\lambda_{\max}=630\pm 5$ nm and $\lambda_{\max}=710\pm 5$ nm) covered with mercaptopropionic acid (MPA) were purchased from PlasmaChem GmbH, Germany. The stock solution of quantum dots was prepared by diluting crude powder in distilled water to get $c=10^{-8}$ M. Then, it was further diluted to $c=10^{-9}$ M either in the distilled water or saline, depending on the experimental group. The pH of saline was adjusted to the value of interest by titrating it with KOH or HCl. The specimens were prepared at various pH values ranging from 4.0 to 13.8, which was measured using Pt/H pH-meter pH315i/SET. The fluorescence spectra of each solution were recorded at different time intervals from preparation (up to 14 days). All specimens were kept at room temperature.

The fluorescence spectra were recorded using *Perkin Elmer LS 50 B* luminescence spectrophotometer. The 390 nm wavelength was chosen for the QD excitation. Human osteosarcoma U2-OS cells were chosen for imaging experiments using two types of QDs. Cells were maintained in RPMI containing 10% FCS, 10,000 U/L Penicillin, 100 mg Streptomycin at standard conditions at 37°C, 5% CO₂.

Two types of QDs were used for cell incubation: CdTe ($\lambda_{\text{max}}=630$ nm was chosen for optimized visualization) and CdSe/ZnS (core/shell).

CdSe/ZnS QDs emitting at 537 nm were purchased from Evident Technologies, USA. The particles were modified with 11-mercaptopundecanoic acid (MUA) following the technique published before [8].

The cells used for incubation with QDs were seeded in chambered cover-slips (NUNC) one day before the experiment.

Confocal imaging for living cells was done using a Zeiss laser scanning microscope (LSM510) equipped with a He-Ne and an Argon ion lasers and emission filter sets for the detection of FITC signals (BP530/20) as well as for Rhodamine signals (LP 580, LP 625). Scanning was controlled by the Zeiss LSM software (version 3.2) and individual colour channels were recorded subsequently to minimize cross talk. The images were further processed using the software LSM 510 (Carl Zeiss Inc). All measurements with confocal microscope were performed in the *Department for Single Cell and Molecule Techniques, Leibniz Institute for Age Research - Fritz Lipmann Institute, Jena, Germany*.

3. Results

3.1. Spectroscopic study

First of all the stability of QDs was investigated in the distilled water. The pH values of the experimental QDs solutions slightly differed from each other being in the range of 6.5-6.8.

The fluorescence spectra measured at initial time had a peak at 710 nm (Fig. 1). The temporal measurements indicated that at the beginning the QDs fluorescence intensity increased slightly during about two hours and no shift of the fluorescence peak was observed. Afterwards the fluorescence intensity started decreasing and the fluorescence peak shifted gradually up to 600 nm (on day 14th). The spectra become wider, indicating the formation of new energetic levels (Fig. 1).

In contrast, when the QD were diluted in saline (pH 6.5-6.8) the fluorescence decreased much faster (Fig. 2). The fluorescence peak was shifted from 710 nm up to 720 nm during first two hours. Further intensity decay of fluorescence band was faster too and was accompanied with a short-waved shift. Finally the spectral features of QDs in saline became similar as in distilled water (Figs. 1, 2).

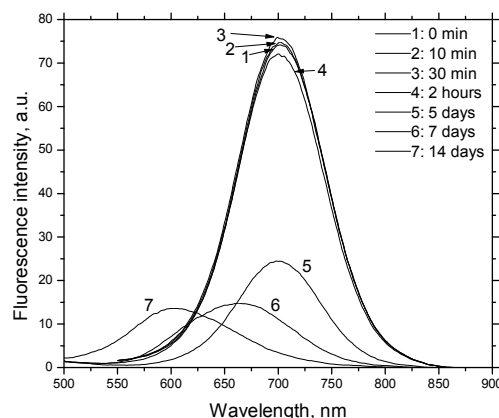


Fig. 1. The changes of fluorescence spectra of CdTe QDs in distilled water, $c=10^{-9}$ M, $\lambda_{\text{ex}}=390$ nm, pH=6.5.

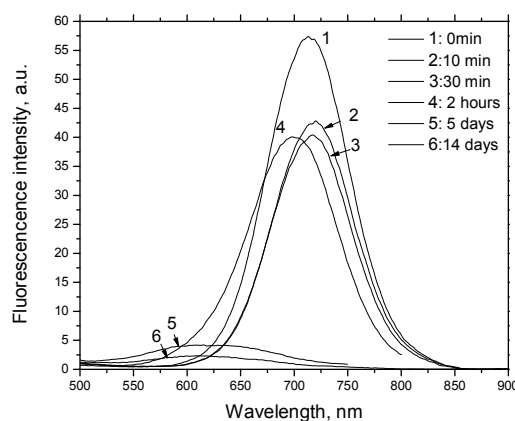


Fig. 2. The changes of fluorescence spectra of CdTe QDs in saline, $c=10^{-9}$ M, $\lambda_{\text{ex}}=390$ nm, pH=6.6.

Taking into account the preliminary results, further investigations of QDs stability in saline at different pH were performed during the first two hours after preparation of solutions. Figure 3 represents the dependence of relative QD fluorescence intensities on pH being measured at two time intervals.

Three regions of pH values can be distinguished according to the observed fluorescence intensity decay rate. The first region (pH 3-5) indicates the fastest fluorescence decrease, which leads to the complete fluorescence bleaching at lowest pH. The fluorescence properties resembled those measured at neutral pH in QD solutions, kept for several days. While initial decay rate at the region of pH 6-8 was almost the same as that at lower pH, it slowed down afterwards leading to the temporal stabilization of fluorescence intensity in about half an hour. The QD fluorescence intensity remained relatively stable or even increased slightly during the observation time in the third region (pH 8-12). Only strongly basic environment caused relatively slow fluorescence decay.

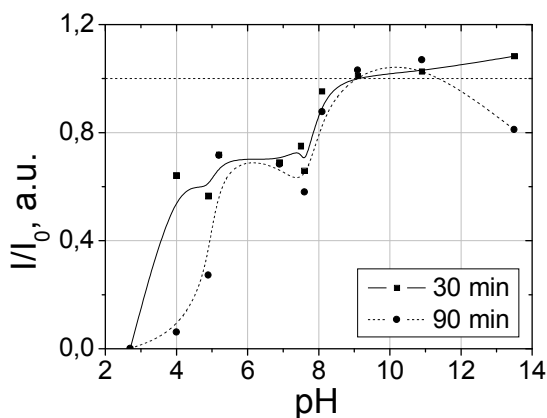


Fig. 3. The relative fluorescence intensity dependence on the pH of the medium at time intervals 30 and 90 minutes.

3.2 *In vitro* incubation with QDs

The cytotoxicity of CdTe QDs of the same type as those used in spectroscopic studies was checked on osteosarcoma cells. The QDs of another type with different shell properties were applied for comparative purposes. Imaging of the cells at different time after incubation revealed that CdTe QDs induced cell

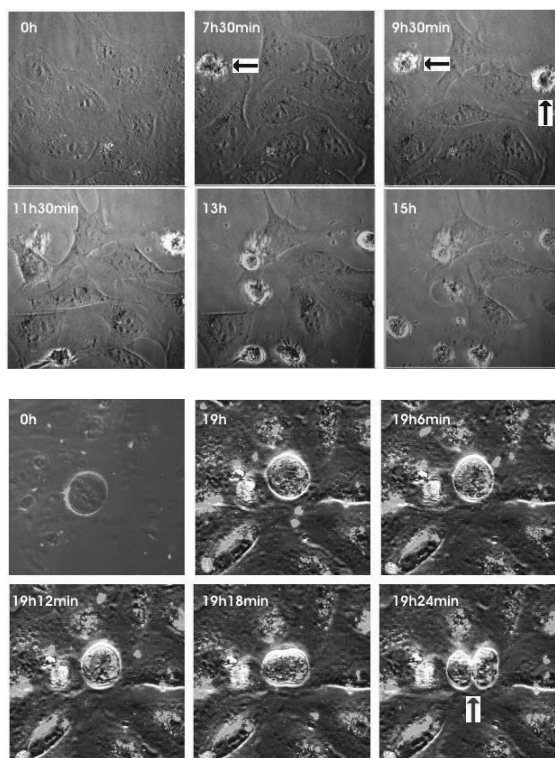


Fig. 4. Top: Significant reduction of the viable human osteosarcoma U2-OS cells (blue arrows) after different incubation time intervals with CdTe-MPA ($c = 2 \cdot 10^{-7} M$) QDs. Bottom: The division of the cells (red arrow) was observed after a 19h incubation with CdSe/ZnS-MUA ($c = 7 \cdot 10^{-6} M$) QDs. inactivation within 7 and half hours (Fig. 4. Top: blue arrows). On the contrary, cells in the presence of

CdSe/ZnS QDs had no effect on cell viability and even division (Fig. 4. Bottom: red arrow).

4. Discussion

Since QDs fluorescence spectra reflected their sensitivity to the surrounding medium, the spectroscopic changes can be related to the processes taking place at the surface of the CdTe particles.

It was found that the fluorescence intensity of QDs in neutral distilled water solution remains relatively stable for at least 2 hours. Meanwhile, it starts decreasing in saline just after solution preparation. This means that increased ionic strength in the case of saline reduces the interaction of protective MPA molecular layer with the QDs surface. Destabilized covering contributes to the fluorescence quenching, increases the possibility for particle aggregation and leads to decreased fluorescence quantum yield [7,9]. Since the size of the QDs determines the fluorescence peak position (1), the blue spectral shift indicates the reduced particle's size [10].

$$D = (9.8127 \cdot 10^{-7}) \lambda^3 - (1.7147 \cdot 10^{-3}) \lambda^2 + 1.0064 \lambda - 194.84 \quad (1)$$

In our case the fluorescence peak gradually shifts per $\Delta\lambda_{max} = 110$ nm. This shift reflects QDs diameter reduction per $\Delta d \approx 2,8$ nm. This means that outer part of the CdTe QDs material transformed into ionic Cd^{2+} and Te^{2-} form, which distributed in the medium.

Bold *et al.* announced about CdTe QDs spectral changes in several different buffering solutions. The group observed “blue” shift and “red” shift of the fluorescence peak. It is thought, that “blue” shift is related to the destruction of the QDs and the release of Cd^{2+} and Te^{2-} ions to the medium. Moreover, this shift was observed even when QDs were dissolved in the distilled water. The “red” shift was best expressed in the pH range of 6.5-7. This phenomenon may be related with the QDs aggregation, when the stabilizing ligands are dissociating from the surface and particles aggregate. The aggregation leads to the decrease in fluorescence intensity and the increase in the spectral width [7,9].

The results of QDs stability in different pH media clearly show that in strongly acidic solutions (pH<5) the CdTe QDs degrade rapidly and after few hours they are no more detectable spectroscopically. In solutions of higher pH QDs show higher physicochemical stability. These results indicate that QDs destabilization and destruction is dependent on the concentration of the H^+ ions, which presumably get involved into the strong interaction with the negatively charged MPA coating and the CdTe core. In stronger basic media (pH>8) there is an excess of OH⁻, which stabilizes the MPA layer and doesn't allow QDs to aggregate. These results are in agreement with other groups [9,11]. However, both the prolonged aggregation and degradation of CdTe QDs take place in all media.

Incubation of the osteosarcoma cells with the CdTe QDs clearly shows that these particles are toxic to the investigated biological system. Keeping in mind that the pH of the cancerous cells is slightly acidic (pH=5-7), the

cytotoxic effect could be provoked by the CdTe QDs destruction and the release of highly toxic Cd²⁺ and Te²⁻ ions to the medium. This fact strongly limits the use of these particles for biomedical applications and makes them not suitable for the imaging of living cells. Meanwhile, CdSe/ZnS QDs, having protective ZnS shell, had no effect on viability of cells and do not suppress its division.

5. Conclusions

This study demonstrated that physicochemical properties of CdTe QDs are sensitive to the ionic composition and the pH of the medium. In basic medium QDs are relatively stable, which is quite opposite in the acidic solutions, where they degrade rapidly, presumably releasing heavy metal ions to the microenvironment. The investigated CdTe QDs are cytotoxic and, therefore, they are not suitable for the fluorescence-based imaging of living cells.

6. Acknowledgements

The authors thank to Karl Otto Greulich and Paulius Grigaravicius from *Department for Single Cell and Molecule Techniques, Leibniz Institute for Age Research - Fritz Lipmann Institute, Jena, Germany* for their help performing experiments with cell cultures and valuable discussions. This study was partially supported by the European Structural funds, the grant No:BPD2004-ERPF-1.5.0-12-05/0035 / BPD-222.

7. References

1. Ballou B, Lagerholm BC, Ernst LA, Bruchez MP, Waggoner AS. Noninvasive imaging of Quantum Dots in mice. *Bioconjugate Chem* 2004. 15:79-86.
2. Karabanovas V, Zakarevicius E, Sukackaite A, Streckyte G, Rotomskis R. Examination of the stability of hydrophobic (CdSe)ZnS quantum dots in the digestive tract of rats. *Photochem. Photobiol. Sci.* 2008. 7:725 – 729.
3. Medintz IL, Uyeda HT, Goldman ER, Mattoussi H. Quantum Dot Bioconjugates for Imaging, Labelling and Sensing. *Nature Materials* 2005. 4:435-56.
4. Wu X, Liu H, Liu J, Haley KN, Treadway JA, Larson JP, Nianfeng G, Peale F, Bruchez MP. Immunofluorescent labeling of cancer marker Her2 and other cellular targets with semiconductor quantum dots. *Nature biotechnology* 2003. 21:41-6.
5. Bullen C, Mulvaney P. The Effects of Chemisorption on the Luminescence of CdSe Quantum Dots. *Langmuir* 2006. 22, 3007-3013.
6. Akerman ME, Chan WCW, Laakkonen P, Bhatia SN, Ruoslahti E. Nanocrystal targeting in vivo. *PNAS* 2002. 20(99): 12617-21.
7. Boldt K, Bruns OT, Gaponik N, Eychemüller A. Comparative examination of the stability of semiconductor quantum dots in various biochemical buffers. *J. Phy. Chem. B*, 2005. 110, 1959 – 1963.
8. Beganskiene A, Karabanovas V, Rotomskis R, Kareiva A. Synthesis of water soluble CdSe quantum dots. International conference on Organic Synthesis, Vilnius, Lithuania. June 29 - July 2, 2008.
9. Zhang H, Zhou Z, Yang B. The influence of carboxyl groups on the photoluminescence of mercaptocarboxylic acid – stabilized CdTe nanoparticles. *J. Phy. Chem. B* 2003. 107, 8 – 13.
10. Kuo YC, Wang Q, Ruengruglikit C, Yu H, Huang Q. Antibody-Conjugated CdTe Quantum Dots for *Escherichia coli* Detection. *J. Phys. Chem. C* 2008. 112, 4818-4824.
11. Pinaud F, Michalet X, Bentolila LA, Tsay JM, Doose S, Li JL, Iyer G, Weiss S. Advances in fluorescence imaging with quantum dots bio-probes. *Biomaterials* 2006. 27:1679-87.

SILVER NANOPARTICLES FOR GAMMA DOSIMETRY

Judita PUIŠO^{*,**}, Jurgita LAURIKAITIENĖ^{*}, Asta Guobienė^{*,***}, Diana ADLIENĖ^{*}, Igoris PROSYČEVAS^{**}

^{*}Department of Physics, Kaunas University of Technology, Studentų g. 50, LT - 51368, Kaunas, Lithuania

^{**}Institute of Physical Electronics, Kaunas University of Technology Savanorių pr. 271, LT-50131, Kaunas, Lithuania

^{***}International Studies Centre, Kaunas University of Technology, Mickevičiaus g. 37, LT - 44244, Kaunas, Lithuania

Abstract: Silver nanoparticles layers were fabricated using spin coating and UV irradiation of polyvinylpyrrolidone/Ag nanoparticle composite thin films on glass. The spontaneous aggregation of Ag nanoparticles was accompanied with the absorption peak due to surface plasmon resonance (SPR) at 410 nm. Gamma irradiation leads to partial coalescence of the nanoparticles with a corresponding shift of SPR towards longer wavelengths. Ag/PVP nanocomposites were investigated by UV-VIS and AFM.

Keywords: Silver, nanoparticles, PVP gamma rays, dose, UV-VIS, AFM

1. Introduction

Silver nanostructures hold great interest due to their unique properties and potential application in nanoelectronics, magnetic, biosensors, data storage, catalysis, surface enhanced Raman scattering and excellent antibacterial properties [1]. Dispersion of metal colloids can be produced in both aqueous and non-aqueous solvents. The latter are potentially more useful in preparation of polymer based nanocomposites [3]. Water soluble Ag nanoparticles/polymer composites were found to possess bioactive properties to suppress bacteria's growth [3-7]. It is very important taking in account the permanent lowering of antibiotic efficiency [4].

Ionizing radiation may control metal nanocrystal growth in various media as example is the photographic process in which visible light impinging on AgBr crystals forms the so-called latent image: photon absorption creates an electron - hole pair, then the components then migrate and are trapped on different sites and the electrons may reduce silver ions. The balance of the process depends on the redox interactions of photoinduced electrons and holes within the emulsion. Stookey and others controlled Ag nanoparticle nucleation by UV and X-ray irradiation in photosensitive glasses [5]. According [6, 7] radiolytic techniques provide several advantages over conventional chemical photochemical techniques, such as:

- a) Reduction of metal ions can be carried out without using excessive reducing agents or producing undesired by-products of the reductant.

- b) Rate of reaction can be controlled since the extent of reduction by radiation is well defined.
- c) Radiation can be employed for reduction irrespective of the presence of light-absorbing solutes and/or products.
- d) Reducing agent can be uniformly distributed in the solution.

Typically the silver nanoparticles are produced by gamma irradiation only at very higher doses from 1 up to 120 kGy [7].

In this work, the results of gamma irradiation effect to on morphology and plasmonic properties of silver nanocomposites are presented.

2. Experimental

Ag-PVP films were produced on the pre-treated glass substrates from the colloidal silver solution in PVP by spin coating. A 4 ml portion of aqua's 0.2 M AgNO₃ containing 20% PVP was prepared in ambient condition. Ag/PVP films were spin-coated from solutions of silver colloidal with "DYNAPERT PRECIMA" centrifuge. The spin speed was above 1800 rpms and spinning time was 30 s. The nanosilver-PVP films were dried in an oven (100 °C) for 10 min and irradiated by UV lamp 60 s.

⁶⁰Co isotope (1.17 and 1.33 MeV) of rotational - convergence gamma therapy source "ROKUS-M" was used as gamma irradiation source. The activity of ⁶⁰Co isotope source was 6.52·10⁺¹³ Bq. The decay time of Co is 5.3 years. The maximum distance between irradiated surface and the (SSD) is 75 cm ± 5 mm. The sample were placed table as a patient and irradiated as usual

medicine procedure under atmospheric pressure and ambient temperature. The field of irradiation was 10 x 10 cm².

The plasmonic properties and structure of Ag/PVP films were investigated by UV-VIS Avantes UV/VIS/NIR AvaSpec-2048. Morphology of silver – polymer structures was investigated with an Atomic force microscope (NANOTOP–206) operating in a contact mode (cantilever force constant 3N/m). Image processing and analysis of the scanning probe microscopy data was performed with a program “Surface View version 2.0”.

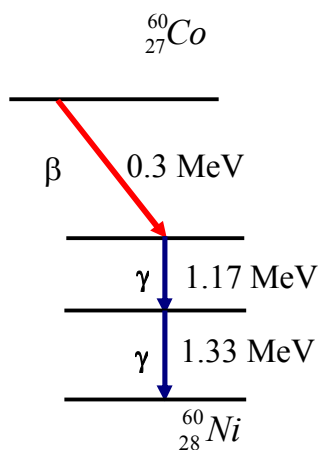


Fig. 1. ^{60}Co isotope decay scheme

The irradiation dose of Ag/PVP nanocomposites films varied from 2 to 50 Gy as it is presented in Table 1.

Table 1. Gamma irradiation doses

| Sample No | Dose, Gy |
|-----------|----------|
| 1 | 20 |
| 2 | 2 |
| 3 | 10 |
| 4 | 50 |
| 5 | 30 |
| 6 | 40 |

3. Results and discussion

The absorbance spectra of non-irradiated Ag/PVP films are presented in Fig.3. The surface plasmon resonance peak (SRP) was observed at 410 nm in absorbance spectra and indicated the spherical silver nanoparticles in PVP matrix. We found good agreement with other researches results [3-5] PVP in this case was as protecting agent of silver nanoparticles agglomeration and reductor also.

The absorbance spectra of Ag/PVP films after gamma irradiation procedure are presented in Fig 4. The influence of gamma irradiation to plasmonic properties of Ag/PVP nanocomposite was observed in absorbance spectra as red shift of SPR peaks from 409 nm to 415 nm and decreasing of SPR peaks intensity up to 30% and increasing of half - width of SPR peaks

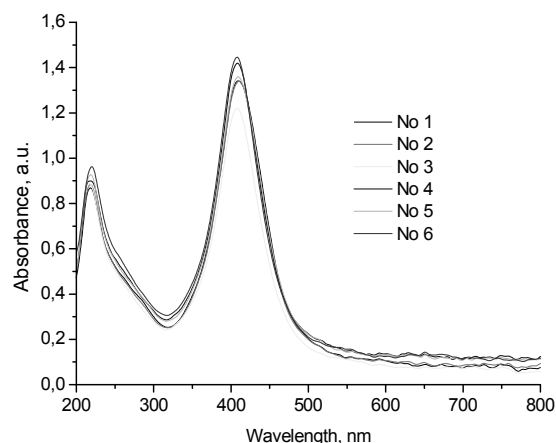


Fig. 2. Absorbance spectra of Ag/PVP nanocomposites films before gamma irradiation.

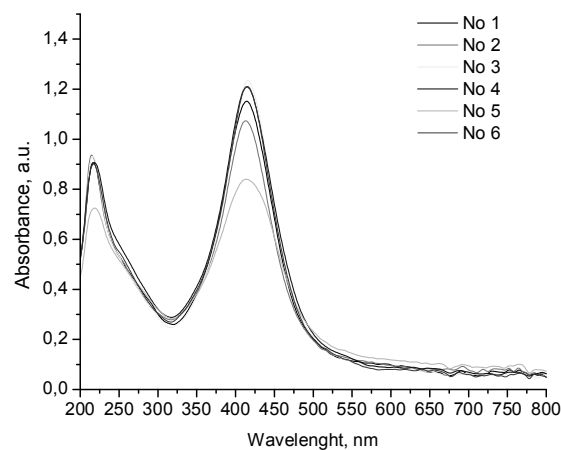


Fig. 3. Absorbance spectra of Ag/PVP films after gamma irradiation.

These results allow suggesting the growth of spherical silver nanoparticles in PVP matrix. The morphology of irradiated Ag/PVP nanocomposites is presented in Fig.4. The dependence of a roughness of Ag/PVP nanocomposites on the irradiation dose is presented in Table 2.

Table 2. Roughness of the samples after the irradiation

| Sample No | Dose, Gy | R _q , nm | R _{sk} , nm |
|-----------|----------|---------------------|----------------------|
| 0 | 0 | 15.30 | -0.59 |
| 2 | 2 | 5.92 | -0.06 |
| 4 | 50 | 2.72 | -0.23 |
| 5 | 30 | 4.10 | -0.58 |

We found that the main Ag/PVP nanocomposites structures are 3D (islands) structure. The gamma irradiation at lower doses (2Gy) induced changes in Ag/PVP morphology. The roughness decreases versus adsorbed doses more than 3.5 times and the surface became more flat.

4. Conclusions

The influence of gamma irradiation to plasmonic properties and morphology of Ag/PVP nanocomposites was absorbed at very lower adsorbed doses (from to 2 Gy). It allows using these structures for gamma treatment. The surface plasmon resonance dependent on the absorbed dose, but the changes in surface morphology of Ag/ PVP nanocomposites is very weak.

5. Acknowledgements

The Lithuanian Science and Study Foundation and COST action MP0803 have supported this work.

6. References

1. Stepanov, A.L. Quantitative analysis of surface plasmon interaction with silver nanoparticles.- *Optics Letters* **30**, No. 12, 2005, 1524-1526 p.
2. Choi N.K., Seo D. S., Lee J.K, Preparation and stabilization of silver colloids protected by surfactant.- *Materials forum*, **29**, 2005, 394-397 p.
3. Wang H., Qiao X., Chena J. and Ding S., Preparation of silver nanoparticles by chemical reduction method. -*Colloids and Surfaces A: Physicochemical and Engineering Aspects* **256**, 2005, 111-115 p.
4. Carotenuto G., Pepe G.P., and Nicolais L., Preparation and characterization of nano-sized Ag/PVP composites for optical applications.- *Eur. Phys. J. B* **16**, 2006 11-17 p.
5. http://www.csns.in2p3.fr/communication/rapports/ra2004/dossier_livre_pour_html/08_physique_des_solides/2_photographie_par_fais_72e.pdf
6. Choi S.-H., Zhang Y.-P., Gopalan A., Lee K.-P., Kang H.-D, . Preparation of catalytically efficient precious metallic colloids by γ -irradiation and characterization *Colloids and Surfaces A: Physicochem. Eng. Aspects* **256** (2005) 165–170 p.
7. Puišo J., Laurikaitienė J., Baltrušaitis V., Prosyčėvas I., Adlienė D., Guobienė A., Modification of Plasmonic Properties of Silver Nanocomposites by Gamma Irradiation. Program and material of the 4th International Conference “Radiation Interaction With Material And Its Use In Technologies 2008“, Kaunas, (2008). 72-75 p.

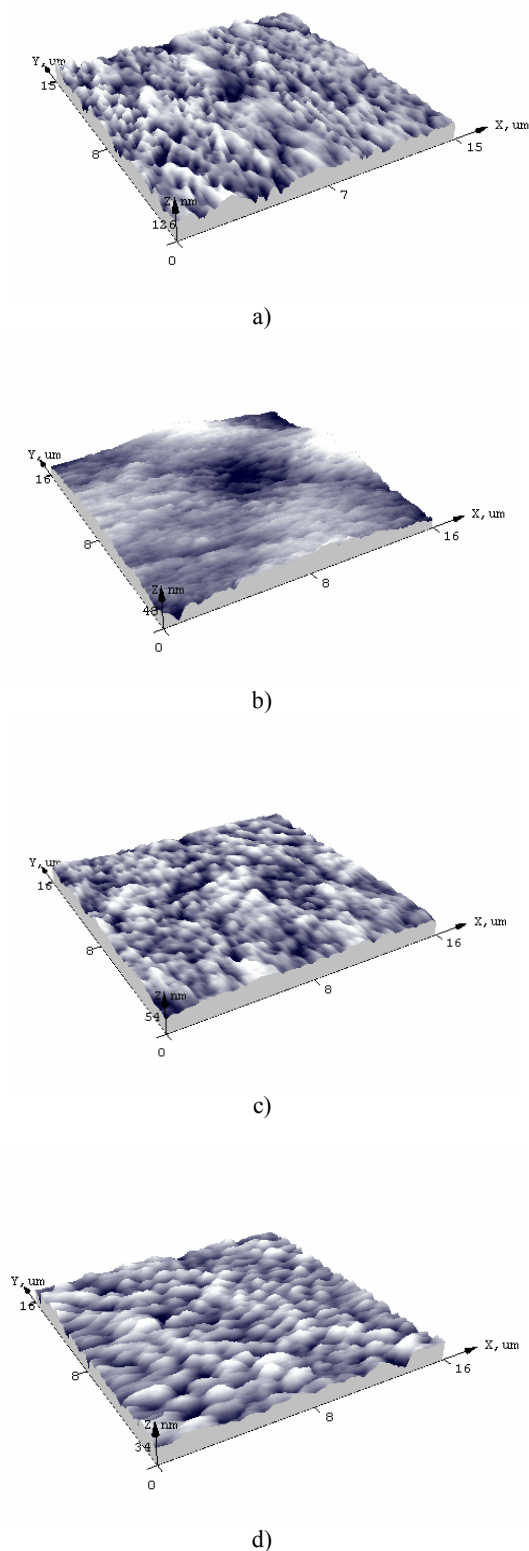


Fig. 5. Morphology of Ag/PVP nanocomposites irradiated by gamma rays a) 0 Gy, b) 2 Gy, c) 30 Gy, d) 50 Gy

ARTIFICIAL INTRAOCULAR LENSES SURFACE INVESTIGATION BY ATOMIC FORCE MICROSCOPE

Vilius PODERYS^{****}, Vytautas JAŠINSKAS^{**}, Reda ŽEMAITIENĖ^{**}, Ričardas ROTOMSKIS^{****}

^{*} Biophotonics Group, Laser Research Centre, Vilnius University, Saulėtekio al. 9, c.3, LT-10222 Vilnius, Lithuania;

^{**} Kaunas medical university ophthalmologic clinic, Kaunas, Lithuania;

^{***} Laboratory of Biomedical Physics, Institute of Oncology of Vilnius University. P. Baublio g. 3, LT-08406 Vilnius, Lithuania

Abstract: Posterior capsule opacification (PCO) is the main postoperative complication following cataract surgery. Different chemical and physical properties of the intraocular lens (IOL) surface material, such as the adhesiveness of the material to the capsule and the surface roughness, are considered to be responsible for PCO. In this study we used atomic force microscope to measure IOL surface roughness and showed that lenses made from different material has different roughness.

Keywords: Intraocular lens, atomic force microscopy, surface characterization.

1. Introduction

With the introduction of small-incision cataract surgery, requirements for intraocular lens (IOL) have rapidly evolved. The IOL material (chemical composition) and surface, however, remains a critical factor influencing IOL biocompatibility – host and implant (IOL) interaction. The implant of IOLs following cataract surgery induces a response of the part of the lens epithelial cells (LECs) (proliferation, migration, differentiation and fibrotic transition of LECs, thus may influence the extent and severity of posterior capsule opacification (PCO)) and a foreign-body reaction to the IOL. IOL material and surface properties are also of relevance for the adherence of white blood cells and microorganisms. Since the IOL can cause two different specific responses following cataract surgery – foreign body response at the level of the uvea and fibrotic and pearl response at the level of the lens capsule, two different types of reactions can be distinguished: the uveal and the capsular.

Uveal biocompatibility. Because of surgical trauma the blood-aqueous barrier will be disrupted and monocytes and macrophages will migrate from the uveal vessel walls into the aqueous. These cells may adhere to the anterior IOL surface and the density of them reflects the biocompatibility of the IOL material. Monocytes transform into small round cells which mainly reflect the early postoperative reaction to the surgical trauma [1]. These cells are usually present in the first few days-weeks after surgery. The trend of small-round-cell

reaction is similar in eyes with implanted IOLs of different material (silicone, hydrophobic acrylic, hydrophilic acrylic, polymethyl-methacrylate (PMMA) [1], heparin-surface-modified (HSM) PMMA [2]) even in high-risk eyes like patients with uveitic or diabetes. Epithelioid and foreign-body giant cells (FBGCs) are formed by the differentiation and fusion of macrophages. They reflect the lasting non-specific immunological foreign-body reaction. These cells accumulate on the IOL surface, usually found in eyes with a prolonged inflammatory reaction and are an indicator of the uveal bio-incompatibility of IOL materials. Data of studies showed that IOLs made from hydrophobic acrylic material more easily induce a foreign-body reaction in high risk eyes (uveitic or glaucomatous) and thus can be considered to be less uveal biocompatible [1]. Modification of IOL surface by improving hydrophilicity can enhance of surface biocompatibility. Linnola et al. showed that acrylic hydrophobic IOLs have a significantly higher concentration of fibronectin (FN) adhered to the surface than silicone, PMMA, and hydrogel lenses [3]. Fibronectin is a specialized protein of extracellular matrix involved in cell adhesion and migration. Increased adhesion of FN to the acrylic hydrophobic IOL is probably a main reason this lens has a higher tendency to have FBGCs on its surface than IOLs of different materials. From the other side, the other clinical studies data [4] and our long-lasting clinical experience show that acrylic hydrophobic lenses provide very good postoperative clinical outcomes in

healthy and high-risk eyes (low grade inflammatory cell adhesion, even lower than HSM PMMA IOLs) and can be indicated in patients with pathologies predisposing to blood-aqueous barrier damage like uveitic, diabetes, pediatric patients.

Capsular biocompatibility. In ophthalmic literature capsular biocompatibility is defined as the reaction of LECs and lens capsule to IOL material. It is generally seen as the ability to inhibit proliferation and migration of LECs and so to lower PCO development [5]. The incidence and intensity of anterior and posterior capsular opacification are thus parameters of capsular biocompatibility. Acryl and silicone are the most frequently used materials at present. During the last years many studies have shown that acrylic IOLs and new generation silicone IOLs have very low PCO rate [6]. Hydrophobic/hydrophilic surface properties are important parameters in capsular biocompatibility. The effect on PCO of the same material but with different affinity to water can differ dramatically, e.g. hydrophobic and hydrophilic acrylics. Hydrophobic materials induce more fibrous transformation of the LECs. LECs proliferating between the anterior capsule and the IOL surface undergo fibrous metaplasia, leading to opacification of anterior capsule (ACO) [1, 7]. ACO is an important parameter for IOL biocompatibility. Hydrophobic IOLs also show more fibrosis of the posterior capsule (fibrotic PCO) [1]. Hydrophilic materials support LEC proliferation better or may incite LEC growth on IOLs surface, with less or no fibrotic metaplasia. It results less ACO and less development of fibrotic PCO, but significantly more Elschnig's pearls formation (regenerative type of PCO) [1] which produces more visual disturbances than fibrotic PCO type and because of that clinically is more important. Therefore hydrophilic acrylic material has good uveal but bad capsular biocompatibility and hydrophobic acrylic material lower uveal but better capsular biocompatibility. The ideal biomaterial should not induce a foreign-body reaction of the uvea, and should inhibit LEC's proliferation.

Numerous authors have pointed out the importance of lens material after demonstrating that acrylic and second-generation silicone IOLs are associated with less PCO than polymethylmethacrylate (PMMA) lenses [8,9]. The different physical properties of the optic surface of the lens biomaterial, such as the adhesiveness of the material to the capsule and the surface roughness, are considered to be responsible for this clinical observation [10]. However, the mechanism by which the IOL biomaterial influences LEC behaviour is not well understood and requires further investigation by analyzing the IOL surface or the mechanical properties of the IOL [11].

Because biocompatibility reflects the interaction between the material's surface and cells, cellular responses to cataract surgery may be influenced by the surface properties of the IOL. This study analyzed the surface roughness of 4 lens materials used in ophthalmic surgery. The aim of this paper was to extend the knowledge of the physical properties of the surface optic of currently available IOLs through atomic force microscopy technology, which can explore IOL surfaces

and provide information with a nanometre spatial resolution.

2. Materials and methods

A commercially available atomic force microscope diInnova (Veeco instruments inc., USA) was used to take 3-dimensional (3-D) images. RTESP cantilevers (Veeco instruments inc., USA) with a tip curvature of >10 nm and a nominal spring constant of 40 Newton/meter (N/m) were used. The measurements were performed in tapping mode in air.

Five types of posterior chamber IOLs (5 different manufacturers) were examined: 1- PMMA, 3- hydrophobic polyacrylic, 1- hydrophilic polyacrylic, 1- silicone and 1- silicone lens coated with gold. One sample of each IOL type was used for analysis. The IOL was removed from its pack, placed on a magnetic stainless-steel sample holder and fixed to it with scotch tape.

All images were acquired at a scan rate of 1 Hz per line with a 512 pixel x 512 pixel image definition. Image processing included flattening (2nd order) to remove the background slope caused by the irregularities of the piezoelectric scanner. The analysis was performed using the SpmLabAnalysis software (Veeco instruments inc., USA). The surface morphology was evaluated to obtain information on average peak to peak distance, average angle of valley and the root mean square (1) of the roughness within a given area of the height data.

$$RMS = \sqrt{\frac{1}{N} \sum_{i=1}^N (Z_i - Z_{av})^2} \quad (1)$$

here Z_i – heigth at pixel i , N – number of pixels in image, Z_{av} - average height.

For each sample, the roughness measurements and peak/valley analysis were performed on 4 reference areas of $5\mu\text{m} \times 5\mu\text{m}$ high-quality images on different IOL surface locations to verify the reproducibility of the observed features.

3. Results

Typical images of all investigated IOLs are presented in fig. 1.

Surfaces of all investigated IOLs were relatively smooth, but AFM images of different lenses differed (even in case of lenses made of same material). In order to get quantitative differences between lenses we performed surface roughness and peak/valley analysis. Calculated quantitative IOLs surface parameters are summarized in table 1.

By calculated parameters we tried to divide all investigated IOLs in to groups. First group – the most flat lenses consisted of all hydrophobic acryl lenses. Hydrophilic acryl, silicon and silicon coated with gold got in to second group. Lens made of PMMA had highest roughness parameters and belonged to third group.

Despite all three hydrophobic acryl lenses were made by different manufacturers, they were least rough from all

investigated lenses. Roughness (RMS) of all hydrophobic acryl lenses was very similar: 2,2 nm, 2,2 nm and 1,3 nm. Peak/valley analysis showed, that these lenses had smallest valley angle of all investigated IOLs (0.5°, 1.4° and 0.5°). Average peak to peak distance was similar for first and third hydrophobic acryl lenses (65 nm and 75 nm), but for second lens it was bigger (110 nm). According to roughness analysis all these three lenses are quite similar, but one can see that AFM images of these lenses looks differently. First lens has some bigger (approx 150 nm in diameter and 15 nm in height) and smaller (approx 45 nm in diameter and 3 nm in height) dots on its surface. These dots may be debris (this lens was non sterile sample), but it also can be caused by some special manufacturing process (these dots are very similar in size and distribution all over the sample, that should not be in case of debris). Second lens has deep hollows (up to 20 nm).

IOLs made of silicon, hydrophilic acryl and silicon coated with gold got into second group. Roughness of these was bigger than in case of hydrophobic acryl lenses. Roughness (RMS) of these lenses was quite similar: 5.0nm (silicone lens), 5.8nm (hydrophilic acryl lens) and 6.0nm (silicone coated with gold lens). Despite similar surface roughness peak to peak distance, average angle of valley and AFM images are different. Average peak to peak distance of silicone lens is small (66,7 nm) and angle of valley is quite big (5.6°). This lens also has some round structures on it. Like in case of hydrophobic acryl lens, these structures can be caused by manufacturing process or it can be debris. Hydrophilic acryl lens has numerous grooves with different orientation on its surface (probably made by polishing the lens). Surface of lens made of silicon with gold coating looks like made of lots of small islands. Islands has no regular shape, grooves separating islands are not straight. This lens was custom made (commercially not available) by evaporating a thin layer of gold on the lens surface. These small islands could be island of gold that formed after evaporation.

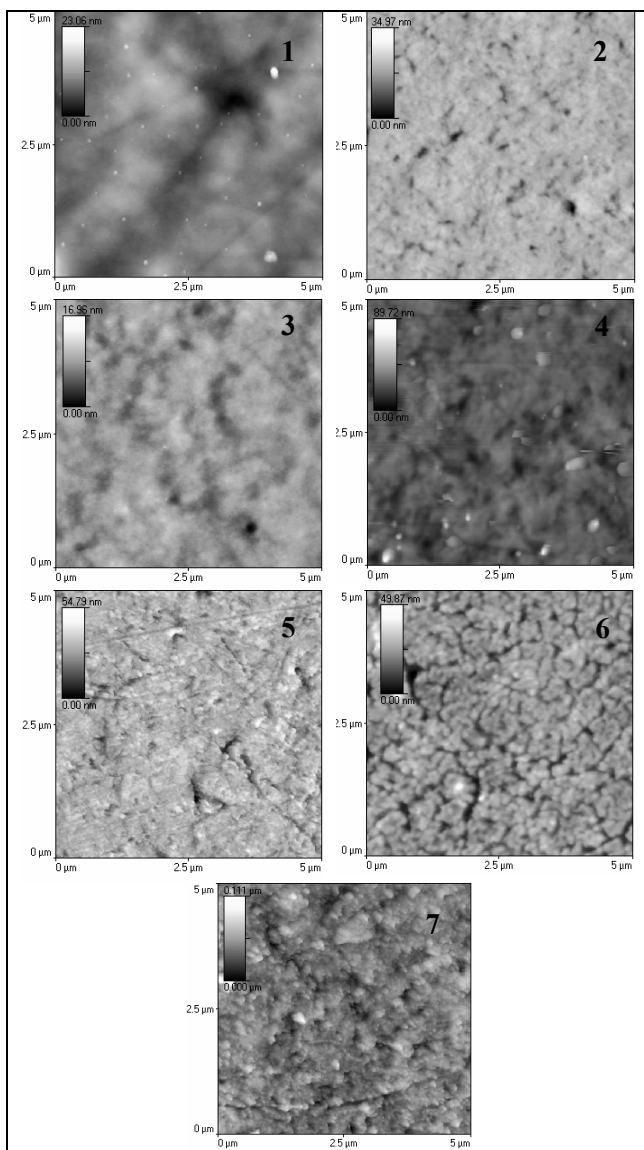


Fig. 1 Typical AFM images (5 μm x 5 μm view) of investigated IOLs. 1, 2, 3 – hydrophobic acryl lenses, 4 – hydrophilic lens, 5 – silicon lens, 6 – silicon coated with gold lens, 7 – PMMA lens.

Table 1. Quantitative surface parameters of investigated IOLs, calculated from 5mm x5mm AFM scans.

| IOL | Peak/valley | | Roughness | | |
|--------------------------|-------------|-------|-----------|-----------------|------------------|
| | dist. | angle | RMS | h _{av} | h _{max} |
| Hydrophobic acryl | 65.0 | 0.5 | 2.2 | 8.3 | 25.5 |
| Hydrophobic acryl | 110.0 | 1.4 | 2.2 | 24.4 | 31.2 |
| Hydrophobic acryl | 75.0 | 0.5 | 1.3 | 7.7 | 19.2 |
| Silicon | 66.7 | 5.6 | 5.0 | 30.8 | 59.0 |
| Hydrophilic acryl | 145.0 | 1.9 | 5.8 | 27.8 | 77.9 |
| Silicon coated with gold | 155.0 | 3.3 | 6.0 | 22.4 | 56.3 |
| PMMA | 95.0 | 8.2 | 11.6 | 54.5 | 126.0 |

Third group consist of only one lens – lens made of PMMA. This IOL had the roughest surface of all investigated lenses. It had highest roughness RMS=11.6 nm, highest average and maximal height (h_{av}=54.5 nm, h_{max}=126.0 nm) and biggest average valley angle (8.2°).

4. Discussion

From the first implanted IOL (Harold Ridley) to now postoperative endophthalmitis remains the most feared complication of cataract surgery. Improvements in operative techniques and the introduction of new IOL materials and surface modifications have reduced the incidence of this dreaded complication at rate of 0.05%. Although this rate appears to be low, the consequences of prosthetic lens-associated endophthalmitis are potentially grave. IOL implantation is accompanied by mild inflammatory tissue reaction [3]. Immediately after implantation of a foreign body (IOL), the implant's surface characteristics are modified by immediate adsorption of a protein layer. It is known that adsorption

of biomolecules to the surface depends on the physicochemical properties (biocompatibility) of material. These properties include surface chemical composition, hydrophilicity, nanostructure of surface and etc. It was shown, that cell adhesion to surface depends on IOL material [12, 13], surface roughness [14] and surface hydrophilic/hydrophobic properties [15]. AFM is a very good tool for surface characterization. Lombardo et. al. [16] showed that it can be used to measure roughness of IOLs. In our study we measured roughness of seven different IOLs. We obtained, that surface roughness of lenses made of same material (despite the lenses were made by different manufacturers) is very similar. But it was clearly seen that surfaces of investigated hydrophobic acryl lenses are not exactly the same. This probably was caused by manufacturing process. The roughest lens in our study appeared to be PMMA lens and roughness of silicone, hydrophilic acryl and silicone coated with gold was intermediate. Our measured roughness of IOLs was slightly different from that reported in [16]. In case of PMMA it was bigger (11.6 nm compared to 7 nm), in case of hydrophobic acryl it was smaller (2.2 nm compared to 4.5 nm), in case of silicon it was nearly the same (5 nm compared to 4nm). These discrepancies could appear because lenses were made by different manufacturers (except for silicone lens).

Number of studies [14] showed that surface roughness is directly proportional to cell adhesion (the rougher is surface the cells adhere to it), and now smoothening of material if standard procedure in IOL manufacturing. According to roughness parameter hydrophobic acryl lenses are best IOL of all our investigated lenses and PMMA IOL was the worst. IOL made of silicon, hydrophilic acryl and silicon coated with gold had very similar roughness. Investigation of IOL made from different materials but with same roughness could help to find the best suitable material for IOL. Further improvement of IOL biocompatibility could also be done by modulating of surface nanostructure.

5. Conclusions

This study showed different surface features between the biomaterials of IOL optics, these differences were probably dependent on the lens fabrication processes. It is likely that surface optic topography of IOLs by different manufacturers varies depending on the different manufacturing processes used.

Surface topography of IOLs also influences cell adhesion to IOL. The detailed knowledge of the IOL's interfacial properties acquired with atomic force microscopy may be important in the development of more biocompatible IOLs.

6. Acknowledgements

This study has been supported by the European Structural funds, the grant No BPD2004-ERPF-1.5.0-12-05/0035 / BPD-222.

7. References

1. Abela-Formanek C, Amon M, Schauersberger J, Kruger A, et al. Results of hydrophilic acrylic, hydrophobic acrylic, and silicone intraocular lenses in uveitic eyes. *J Cataract Refract Surg* 2002; 28: 1141-1152.
2. Gatinel D, Lebrun T, Le Toumelin P, Chaine G. Aqueous flare induced by heparin-surface-modified poly(methyl methacrylate) and acrylic lenses implanted through the same-size incision in patients with diabetes. *J Cataract refract Surg* 2001; 27:855-860.
3. Kanagawa R, Saika S, Ohmi S, Tamura M, Nakao T. Presence and distribution of fibronectin on the surface of implanted intraocular lenses in rabbits. *Graefes Arch Clin Exp ophthalmol* 1990; 228: 398-400.
4. Tognetto D, Toto L, Minutola D, Ballone E, Di Nicola M, Di Mascio R, Ravalico G. Hydrophobic acrylic versus heparin surface-modified polymethylmethacrylate intraocular lens: a biocompatibility study. *Graefes Arch Clin Exp ophthalmol* 2003; 241: 625-630.
5. Apple DJ, Peng Q, Visessook N, Werner L, et al. Surgical prevention of posterior capsule opacification. Part 1: Progress in eliminating this complication of cataract surgery. *J Cataract Refract Surg* 2000; 26: 180-187.
6. Zemaitiene R, Jasinskas V, Auffarth GU. Influence of three-piece and single-piece designs of two sharp-edge optic hydrophobic acrylic intraocular lenses on the prevention of posterior capsule opacification: a prospective, randomised, long-term clinical trial. *Br J Ophthalmol*. 2007; 91:644-648.
7. Marcantonio JM, Rakic JM, Vrensen G, Duncan G. Lens cell populations studied in human donor capsular bags with implanted intraocular lenses. *Invest Ophthalmol Vis Sci* 2000; 41: 1130-1141.
8. Kurosaka D, Obasawa M, Kurosaka H, Nakamura K. Inhibition of lens epithelial cell migration by an acrylic intraocular lens in vitro. *Ophthalmic Res* 2002; 34:29-37.
9. Wejde G, Kugelberg M, Zetterstrom C. Posterior capsule opacification: comparison of 3 intraocular lenses of different materials and design. *J Cataract Refract Surg* 2003; 29:1556-1559.
10. Yamakawa N, Tanaka T, Shigeta M, et al. Surface roughness of intraocular lenses and inflammatory cell adhesion to lens surfaces. *J Cataract Refract Surg* 2003; 29:367-370.
11. Nishi O, Nishi K, Osakabe Y. Effect of intraocular lenses on preventing posterior capsule opacification: design versus material. *J Cataract Refract Surg* 2004; 30:2170-2176.
12. Kodjikian L, Burillon C, Lina G, et al. Biofilm formation on intraocular lenses by a clinical strain encoding the *ica* locus: a scanning electron microscopy study. *Invest Ophthalmol Vis Sci* 2003; 44:4382-4387.
13. Kodjikian L, Burillon C, Roques C, et al. Bacterial adherence of *Staphylococcus epidermidis* to intraocular lenses: a bioluminescence and scanning

- electron microcopy study. *Invest Ophthalmol Vis Sci* 2003; 44:4388-4394.
14. Tanaka T., Shigeta M., Yamakawa N, Usui M. Cell adhesion to acrylic intraocular lens associated with lens surface properties. *J. Cataract Refractive Surg.* – Vol. 31, August 2005.
15. Dick H. B., Frohn A., Augustin A. J., et al. Physicochemical Surface Properties of Various Intraocular Lenses. *Ophthalmic Res* 2001;33:303–309.
16. Lombardo M., De Santo M. P., Lombardo G., Barberi R., Serrao S. Analysis of intraocular lens surface properties with atomic force microscopy, *J Cataract refract. Surg.* – Vol. 32, August 2006.

ZrO₂ GLASS FILMS INFLUENCED BY ULTRAVIOLET RADIATION

Jurijs DEHTJARS*, Natalija POĻAKA*, Renata REISFELD**, Marina ROMANOVA*, Tsiala SARAI DAROV**, Aleksandrs SUDNIKOVĪČS*

*Riga Technical University, Riga, Latvia;

**Hebrew University of Jerusalem

Abstract: Zr oxide glasses are used for biomaterials that can be treated with radiation because of the necessity to improve health of the patient to whom glass is implanted. The aim of the research was to explore the influence of ultraviolet (UV) irradiation on the PbS ZrO₂ films. Photoemission spectra of the films after different UV irradiation doses were registered. It was found that the films could respond to the UV irradiation that signals on the damaging of the material.

Keywords: PbS ZrO₂ nanofilms, ultraviolet irradiation, photoemission spectra.

1. Introduction

Zr oxide glasses are used for biomaterials that can be treated with radiation because of the necessity to improve health of the patient to whom glass is implanted.

The research was targeted to examine photoemission spectra of radiated PbS ZrO₂ films depending on different concentration of PbS nanocrystals.

2. Specimens

The PbS ZrO₂ films were prepared by the sol-gel technology and had embedded lead sulphide (PbS) nanocrystals. [1] Samples with two different concentrations of PbS nanocrystals were available (10% and 20%). PbS ZrO₂ films were deposited on a glass substrate. Thickness of the films was <0.1-1 μm.

3. Experimental part

The samples were irradiated using xenon-mercury lamp (ultraviolet spectrum) with exposure 0 – 75 min. Then, the photoemission spectra of irradiated samples were recorded using ultraviolet spectroscopy method. For this the hand made spectrometer was in use. All measurements were provided at room temperature in vacuum 10⁵ torr.

4. Results

Photoemission spectra at different irradiation time are shown in Fig.1.

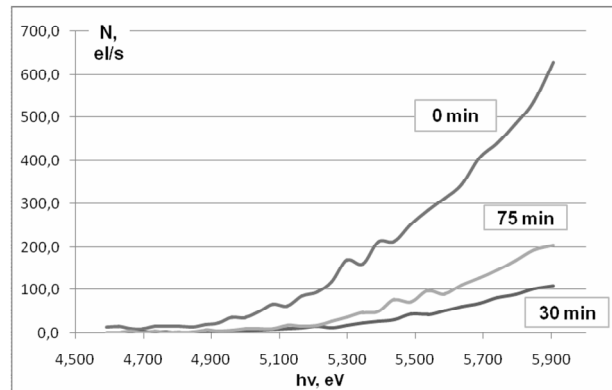


Fig. 1. Intensity of the emitted electrons at different irradiation time for the samples 20%PbS ZrO₂

Because the electrons (it was assumed) could escape both from the film and the substrate the photoemission spectra were separated in the log scale. As the results two straight lines for all specimens except those of the glass substrate were observed at the regions 4.90 – 5.30 eV and 5.30 – 5.91 eV, correspondingly. Photoemission process for each region was described by the equation:

$$N = A(h\nu - \varphi)^m \quad (1)$$

where N – current of the emitted electrons, el/s, A – a coefficient that connects to the density of electron states, m – a coefficient that deals with transitions channel between the initial and final states; $h\nu$ – photon energy, eV, φ – photoelectric work function, eV. The calculated results related to the parameters of the formula (1) are shown in Fig.2, Fig.3 and Fig.4.

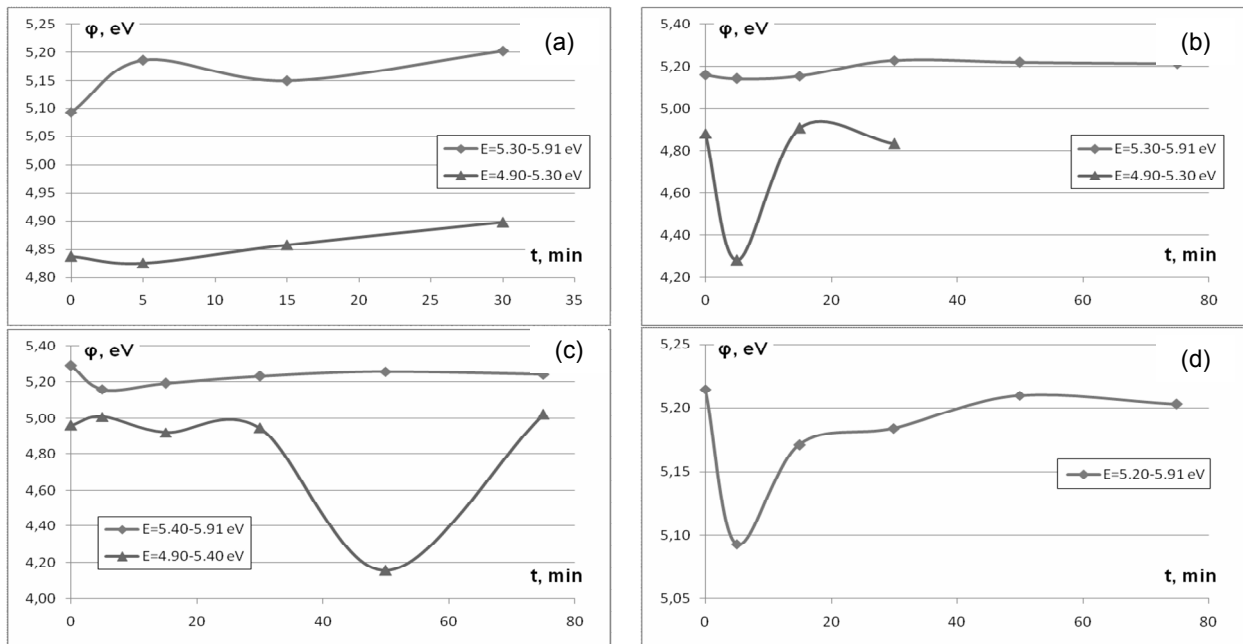


Fig. 2. The work function ϕ versus irradiation time t for the specimens (a) 10% PbS ZrO₂, (b) 20% PbS ZrO₂, (c) ZrO₂, (d) Glass substrate.

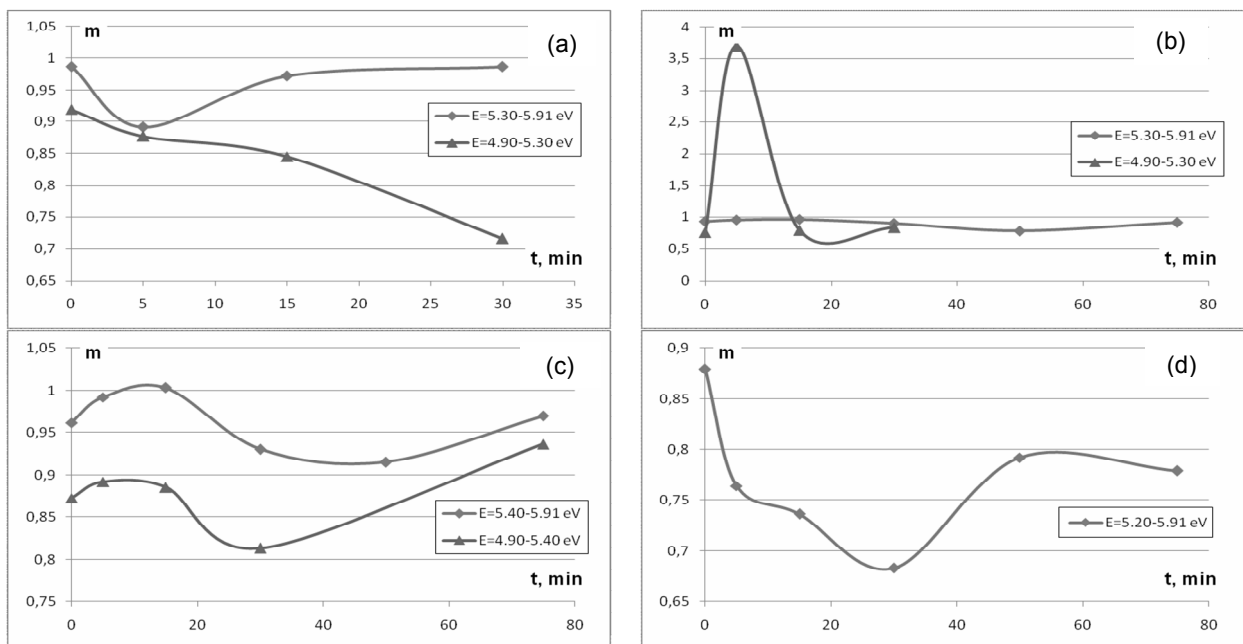


Fig. 3. The m coefficient versus irradiation time t for the specimens (a) 10% PbS ZrO₂, (b) 20% PbS ZrO₂, (c) ZrO₂, (d) Glass substrate.

The work function ϕ and the m coefficient don't change significantly with irradiation time. The A coefficient, however, changes.

The changes of the A coefficient for 20% PbS ZrO₂ film were compared with those of the glass substrate. The A coefficient of the glass substrate changes slightly in comparison with 20% PbS ZrO₂ film. The next step was to compare the same changes for 20% PbS ZrO₂ and ZrO₂ films. The behaviour of the changes is different for these both materials. Finally, the changes of the A coefficient for 10% PbS ZrO₂ and 20% PbS ZrO₂ films were compared. One can see that a value of the A coefficient drops noticeably upon an increase in

irradiation time when we consider a film with higher PbS concentration (20%).

That's why one could suppose that the behaviour of the A coefficient depending on irradiation time is contributed mainly by PbS nanocrystals.

The next step was to select photoemission signal of the PbS ZrO₂ nanofilm out of the whole registered signal. To achieve this, photoemission spectra of the glass substrate at different irradiation time were subtracted from the corresponding photoemission spectra of PbS ZrO₂/glass substrate samples. Obtained spectra ΔN for the 10% and 20% PbS ZrO₂ films with different irradiation time are shown in Fig. 5.

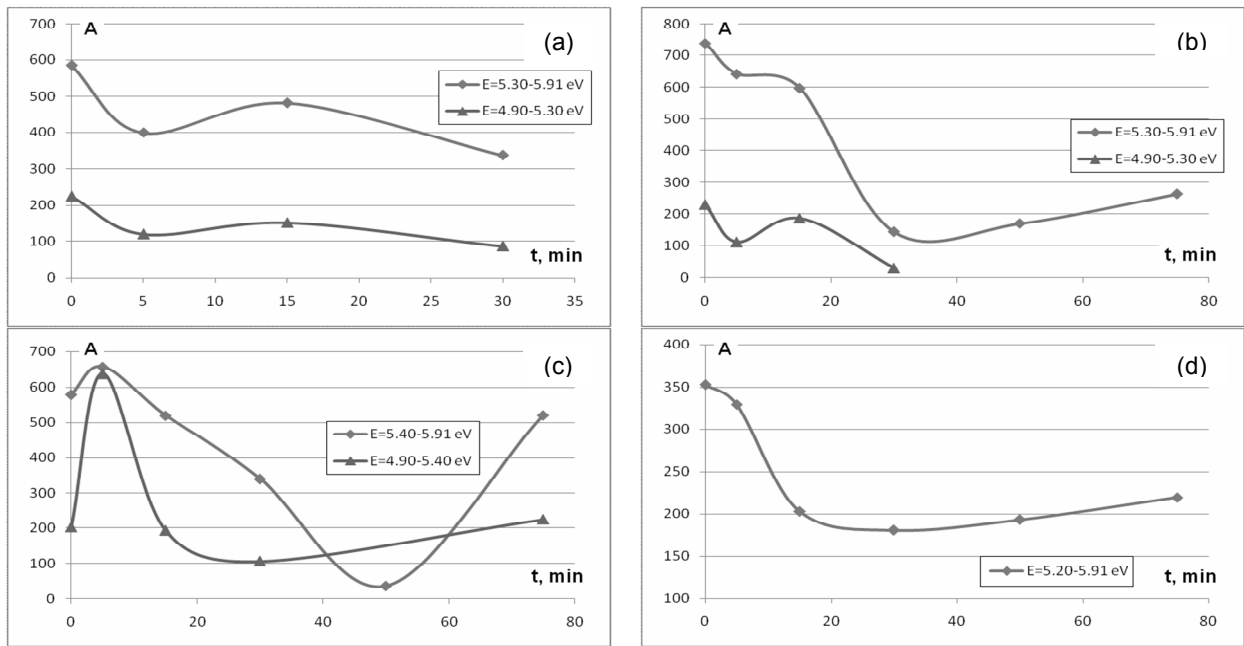


Fig. 4. The A coefficient versus irradiation time t for the specimens (a) 10% PbS ZrO₂, (b) 20% PbS ZrO₂, (c) ZrO₂, (d) Glass substrate.

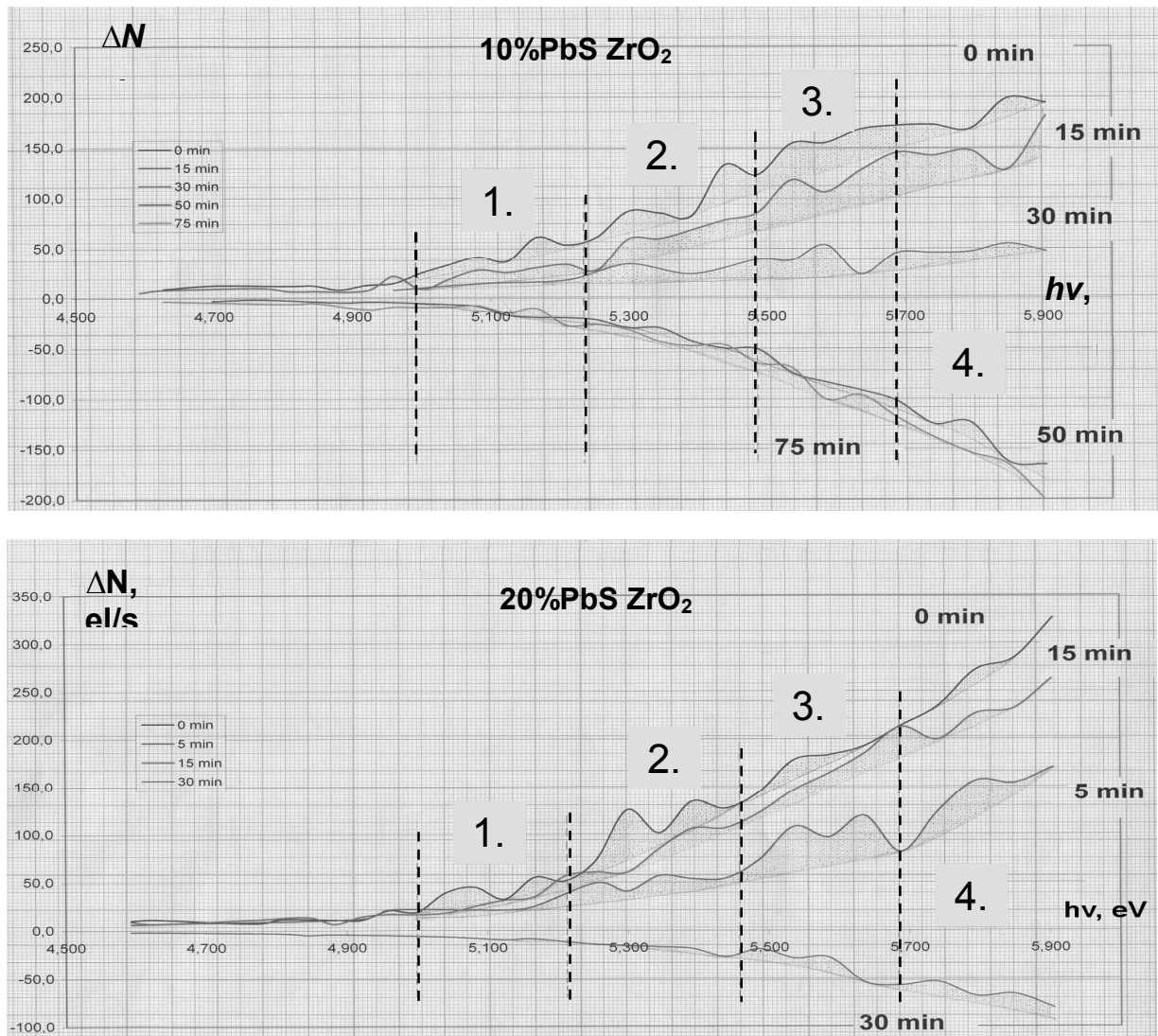


Fig. 5. Processing of photoemission spectra of the 10% and 20% PbS ZrO₂ films with different irradiation time

Table 1. Division of the photoemission spectra into photon energy regions

| | Region No. | | | |
|--------------------------|----------------|----------------|----------------|----------------|
| | 1. | 2. | 3. | 4. |
| 10% PbS ZrO ₂ | 4.99 – 5.23 eV | 5.23 – 5.49 eV | 5.49 – 5.69 eV | 5.69 – 5.90 eV |
| 20% PbS ZrO ₂ | 5.00 – 5.21 eV | 5.21 – 5.45 eV | 5.45 – 5.69 eV | 5.69 – 5.90 eV |

Photoemission spectra of the non-irradiated 10% and 20% PbS ZrO₂ films were divided into four regions that correspond to photon energies at which peaks occurred (Fig. 5).

The values of photon energy for each region are given in the Table 1.

A baseline was drawn for each spectrum (see Figure 5). Then the area between the peaks and a baseline was

calculated for each region. Dependence of the calculated area upon irradiation time for 10% and 20% PbS ZrO₂ films is shown in Fig. 6 and Fig. 7.

A linear approximation was done for each graph using Ms Excel Trendline option. R-squared value was displayed for the trendlines. The best results were observed for the samples with 20% PbS concentration within photon energy regions No. 1 and No. 2.

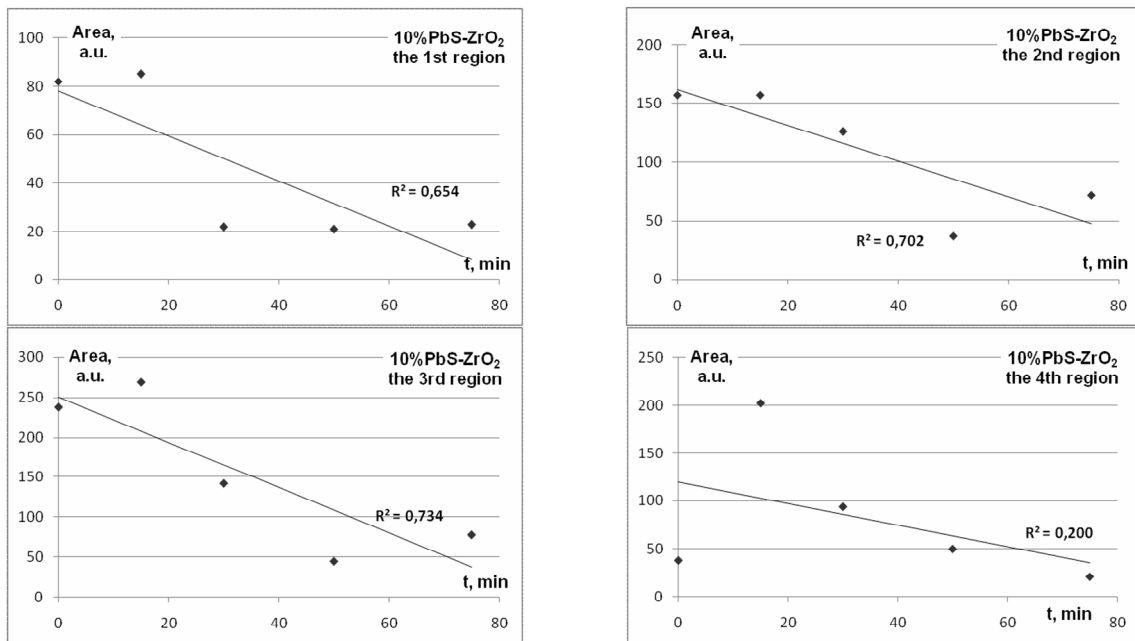


Fig. 6. Dependence of the area under photoemission peaks upon irradiation time for 10% PbS ZrO₂ films

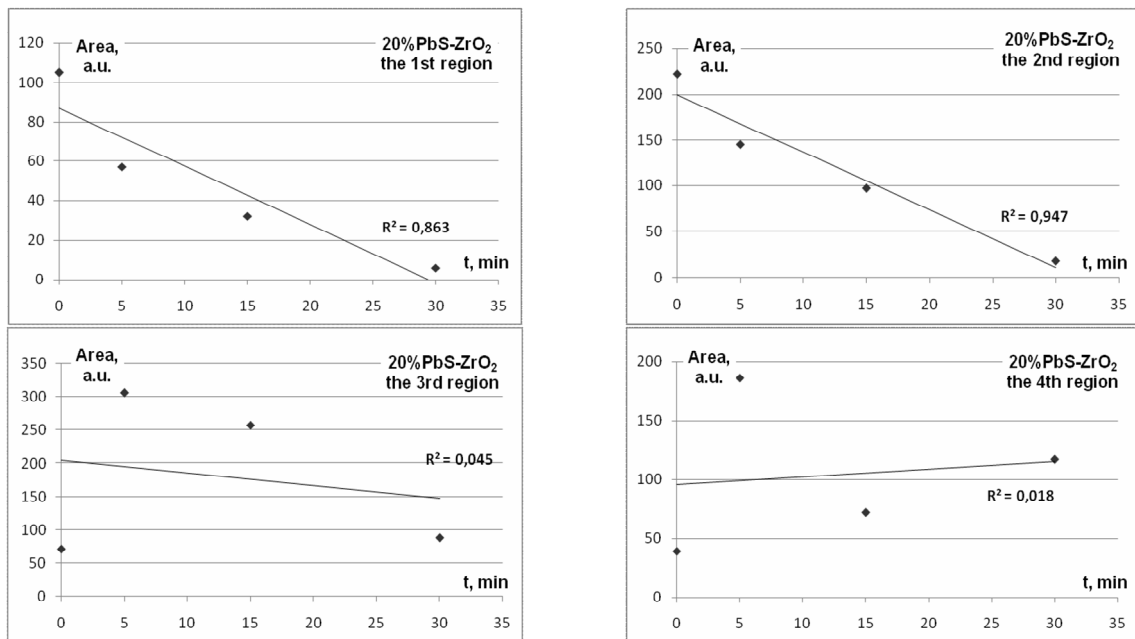


Fig. 7. Dependence of the area under photoemission peaks upon irradiation time for 20% PbS ZrO₂ films

In Figure 8 emission spectra ΔN of 10% and 20% PbS ZrO₂ films are provided for the equal irradiation time. One can see that the shapes of the spectra repeat themselves (peaks that repeat themselves on both spectra are marked with arrows). That means that the registered spectra are not of random nature.

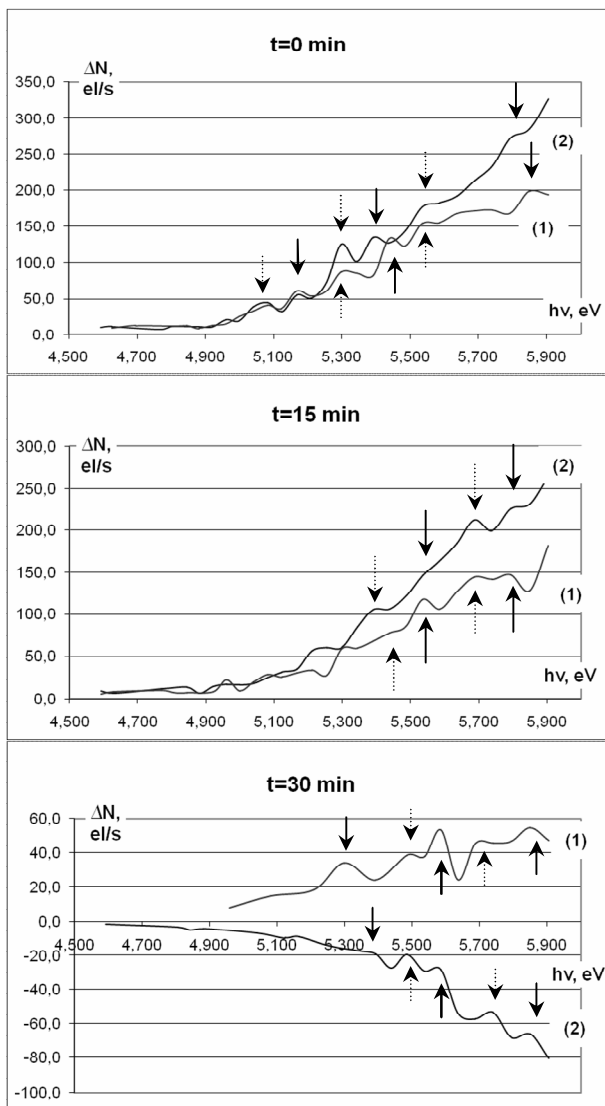


Fig. 8. Comparison of spectra ΔN of (1) 10% and (2) 20% PbS ZrO₂ films with equal irradiation time

Figure 9 demonstrates differences between spectra of the irradiated and non-irradiated specimens. The figure evidences that the specific features of the spectra result from UV radiation.

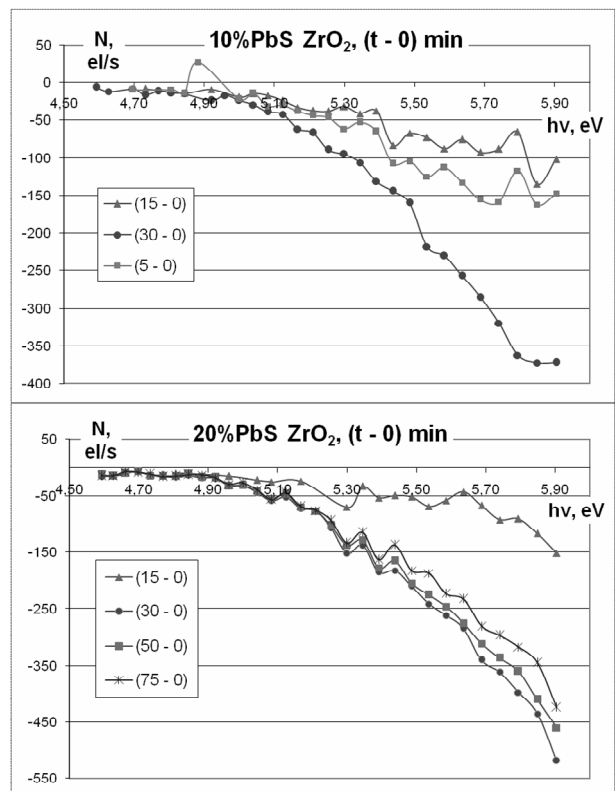


Fig. 9. Differences between the spectra of the irradiated and non irradiated specimens

5. Conclusion

The tested specimens demonstrated responses of some spectra maximums on radiation exposure. However, such the response has a negative correlation with exposure. This perhaps is because radiation destroys electron emission centres. The results allow us to assume that PbS nanodots or their environment are responsible for the above.

6. References

1. Sashchiuk A., Lifshitz E., Reisfeld R., et al. Optical and Conductivity Properties of PbS Nanocrystals in Amorphous Zirconia Sol-Gel Films // Journal of Sol-Gel Science and Technology, Vol. 24, Issue 1, 2002-05-01; 31-38.p.

GREY SCALE MEASUREMENTS OF VIDEO DISPLAYS

Vytenis PUNYS^{*,**}, Mindaugas ZIKAS^{**}

^{*} Department of Biophysics, Klaipėda University, Klaipėda, Lithuania;

^{**} Kaunas University of Technology, Kaunas, Lithuania

Abstract: An overview of a particular topic of quality assurance in diagnostic radiology is presented - the ways to display diagnostic images consistently on computer monitors, transmissive and reflective media. That might be achieved by calibrating imaging equipment according to the Greyscale Standard Display Function (GSDF). GSDF is based on the Barten model of human perception of just noticeable differences of greyscale. It is defined in the DICOM (Digital Imaging and Communication in Medicine) standard, as well as recommended by the IHE (Integrating the Healthcare Enterprise). Practical pilot implementation of such calibration tool is presented.

Keywords: digital radiology, consistent display of images, Barten model, GSDF, Greyscale Standard Display Function, DICOM.

1. Introduction

Digital imaging equipment is more and more widely used in the diagnostic radiology practice within the new member states of the EU. Diagnostic radiology departments are trying to become filmless – images are more reviewed on computer monitors, than on films. Those parts of quality assurance systems in radiology that were developed to ensure acceptable quality of images on films, should be extended into the field of computer monitors (so called softcopy imaging) and special printers, producing hard copies of images on sheets of special photo-paper and/or special transparent film without wet chemical development and fixation process.

The general goal is to ensure, that the same image leads to the same diagnostic decision regardless of the way it was presented to a radiologist (softcopy or hardcopy: transmissive or reflective). These three different ways of presenting an image for a user should be based on a single model of human eye perception of grayscale image, which might allow ensuring of normalised visualisation conditions (or standardised display functions).

2. The Standardized Display Functions

The standardized display functions, used to display images consistently, i.e. under normalised conditions, are described in the part 14 of the DICOM standard [1], which development was initiated and is being coordinated jointly by the American College of Radiologists (ACR) and the National Electrical Manufacturers Association (NEMA). Such functions

use the mathematical models to describe the human vision [2,3,4,5].

The human eye does not perceive absolute intensity values but quotients of intensity shades. It reacts more sensitive to the brighter areas than to the darker ones. Therefore, display functions are not linear but logarithmical, increasing more in the “brighter” areas than in the “darker” ones. For this reason the different shades of grey appear perceptually linear for an average human observer when an appropriate compensation function is applied.

There are several models developed for constructing Standard Display functions. Most relevant of them are:

- The group of colour-space models developed by the Commission Internationale de l’Eclairage (CIE) since 1931 [4],
- Grey scale oriented the Barten model [5].

The Barten model defining the Greyscale Standard Display Function (GSDF) introduces the concept of Just Noticeable Differences (JND). The luminance range seen by an average observer is divided into a fixed number of just distinguishable luminance values. The model determines the maximum number of shades of grey that can be visualised on a given display.

The CIE $L^*a^*b^*$ model which was developed at the International Polygraphic Commission (Commission Internationale de l’Eclairage) in 1976, is based on an equidistant colour system and is applicable for colour values. This system is more complicated than the Barten model, though the GSDFs of both systems differ only slightly.

As greyscale images are dominating in diagnostic radiology, the Barten model was applied to construct the GSDF in the DICOM standard.

2.1. The Barten model of just noticeable differences

As explained above, the GSDF is based on human Contrast Sensitivity. A Display Function that adjusts the brightness such that equal changes in pixel values will result in the same level of perceptibility at all driving levels of signals supplied to the monitor is “perceptually linearized”. Thus the GSDF incorporates the notion of perceptual linearization.

The employed data for Contrast Sensitivity are derived from Barten’s model of the human visual system [1,3,5]. Specifically, the GSDF refers to Contrast Sensitivity for the Standard Target consisting of a 2° by 2° square filled with a horizontal or vertical grating with sinusoidal modulation of 4 cycles per degree. The square is placed in a uniform background of Luminance equal to the mean Luminance L of the Target. The Threshold Modulation at which the grating becomes just visible to the average human observer defines the Contrast Sensitivity. The Luminance modulation represents the Just-Noticeable Difference (JND) for the Target at the Luminance L.

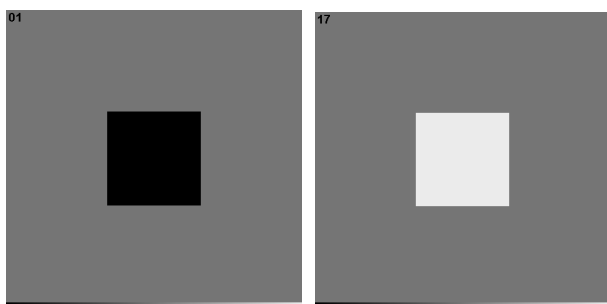


Fig.1. Test images representing the Standard Target for the measurement of Characteristic Curve of a Monitor

The GSDF is defined for the Luminance Range from 0.05 to 4000cd/m². The minimum Luminance corresponds to the lowest practically useful Luminance of cathode-ray-tube (CRT) monitors and the maximum exceeds the unattenuated Luminance of very bright light-boxes used for interpreting X-Ray mammography. The GSDF explicitly includes the effects of the diffused ambient illuminance.

The GSDF is defined by a mathematical interpolation of the 1023 Luminance levels derived from Barten’s model. It allows to calculate luminance, **L**, in candelas per square meter, as a function of the Just-Noticeable Difference (JND) Index, **j**:

$$\lg L(j) = \frac{a + c \cdot \ln(j) + e \cdot (\ln(j))^2 + g \cdot (\ln(j))^3 + m \cdot (\ln(j))^4}{1 + b \cdot \ln(j) + d \cdot (\ln(j))^2 + f \cdot (\ln(j))^3 + h \cdot (\ln(j))^4 + k \cdot (\ln(j))^5} \quad (1)$$

with

ln referring to the natural logarithm,

j the index (1 to 1023) of the Luminance levels **L_j** of the JNDs,

and coefficients

$$\begin{aligned} a &= -1.3011877, & b &= -2.5840191E-2, \\ c &= 8.0242636E-2, & d &= -1.0320229E-1, \\ e &= 1.3646699E-1, & f &= 2.8745620E-2, \\ g &= -2.5468404E-2, & h &= -3.1978977E-3, \\ k &= 1.2992634E-4, & m &= 1.3635334E-3. \end{aligned}$$

The logarithms to the base 10 of the Luminance **L(j)** are very well interpolated by this function over the entire Luminance Range. The relative deviation of any log(Luminance)-value from the function is at most 0.3%, and the root-mean-square-error is 0.0003. The continuous representation of the GSDF permits a user to compute discrete JNDs for arbitrary start levels and over any desired Luminance Range.

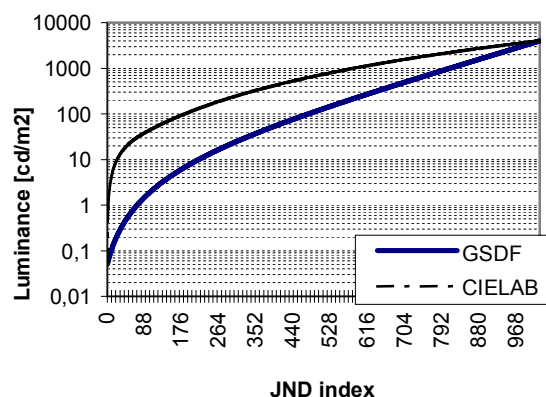


Fig.2. GSDF: the Barten model and the CIE L*a*b* curve

To apply the above formula to a device with a specific range of **L** values, it is convenient to also have the inverse of this relationship, which is given by:

$$j(L) = A + B \cdot \lg(L) + C \cdot (\lg(L))^2 + D \cdot (\lg(L))^3 + E \cdot (\lg(L))^4 + F \cdot (\lg(L))^5 + G \cdot (\lg(L))^6 + H \cdot (\lg(L))^7 + I \cdot (\lg(L))^8 \quad (2)$$

where

lg represents logarithm to the base 10,

$$A = 71.498068, \quad B = 94.593053,$$

$$C = 41.912053, \quad D = 9.8247004,$$

$$E = 0.28175407, \quad F = -1.1878455,$$

$$G = -0.18014349, \quad H = 0.14710899,$$

$$I = -0.017046845.$$

The Characteristic Curve of a Display System represents the Luminance produced by a Display System as a function of control signal to the monitor (DDL, device driving level) and the effect of ambient Illuminance. The Characteristic Curve is measured with Standard Test Patterns (see most black and most white images in Fig.1). In general, the Display Function describes:

- a) The Luminance (including ambient Illuminance) measured as a function of DDL for emissive displays such as a CRT-monitor/digital display controller system,
- b) The Luminance (including ambient Illuminance) as a function of DDL measured for a transmissive

medium hung in front of a light-box after a printer produced an optical density, depending on DDL, on the medium,

- c) The Luminance (including ambient light) as a function of DDL measured for a diffusely reflective medium illuminated by a office lights after a printer produced a reflective density, depending on DDL, on the medium.

By internal or external means, the system may have been configured (or calibrated) such that the Characteristic Curve is consistent with the GSDF.

Some Display Systems adapt themselves to ambient light conditions. Such a system may conform to the GSDF for the level of ambient Illuminance only, unless it had the capability of adjusting its Display Function without user-intervention so that it remains in conformance with the GSDF. Such systems are usually implemented in diagnostic grade medical monitors

2.2. Transmissive Hardcopy Printers

For transmissive hardcopy printing, the relationship between luminance, **L**, and the printed optical density, **D**, is:

$$L = L_a + L_0 \cdot 10^{-D} \quad (3)$$

where:

L_0 is the luminance of the light box with no film present, L_a is the luminance contribution due to ambient illuminance reflected off the film.

If film is to be printed with a density ranging from **D_{min}** to **D_{max}**, the final luminance will range between:

$$L_{min} = L_a + L_0 \cdot 10^{-D_{max}} \quad (4)$$

$$L_{max} = L_a + L_0 \cdot 10^{-D_{min}} \quad (5)$$

and the **j** values will correspondingly range from **j_{min} = j(L_{min})** to **j_{max} = j(L_{max})**.

If this span of **j** values is represented by an N-bit pixel value (P-Value or presentation value, is used in the DICOM as more generalised term), ranging from 0 for **j_{min}** to 2^N-1 for **j_{max}**, the **j** values will correspond to P-Values **p**

$$j(p) = j_{min} + \frac{p}{2^N - 1} \cdot (j_{max} - j_{min}) \quad (6)$$

and the corresponding **L** values will be **L(j(p))**.

Finally, converting the **L(j(p))** values to densities results in:

$$D(p) = -\lg\left(\frac{L(j(p)) - L_a}{L_0}\right) \quad (7)$$

2.3. Reflective Hardcopy Printers

For reflective hardcopy printing, the relationship between luminance, **L**, and the printed optical density, **D**, is:

$$L_{min} = L_0 \cdot 10^{-D} \quad (8)$$

where **L₀** is the maximum luminance obtainable from diffuse reflection of the illumination that is present.

If film is to be printed with a density ranging from **D_{min}** to **D_{max}**, the final luminance will range between:

$$L_{min} = L_0 \cdot 10^{-D_{max}} \quad (9)$$

$$L_{max} = L_0 \cdot 10^{-D_{min}} \quad (10)$$

and the **j** values will correspondingly range from **j_{min} = j(L_{min})** to **j_{max} = j(L_{max})**.

If this span of **j** values is represented by an N-bit P-Value, ranging from 0 for **j_{min}** to 2^N-1 for **j_{max}**, the **j** values will correspond to **p** as in (6), and the corresponding **L** values will be **L(j(p))**.

Finally, converting the **L(j(p))** values to densities results in

$$D(p) = -\lg\left(\frac{L(j(p))}{L_0}\right) \quad (11)$$

3. Measurements of video-displays

The above-described model was recommended for routine use by the IHE (“Integrating the Healthcare Enterprise”) framework, where the special software tools had been developed [6].

Though the software integration (for matching a Display to the GSDF) is rather simple task and the correction function can be implemented very efficiently using look-up tables, designated measurement equipment is not available in Lithuanian healthcare institutions.

The attempts to assess monitors have been carried out by the authors using the PTW Candelameter-1. It was found, that the equipment is not sensitive enough in the lower part of measurement range, and therefore should be used in different measurement (luxmeter) mode. That requires additional pre-processing of measurement data. Magnified by experimentally established coefficient (assuming the linear relationship), the data was entered into the IHE designed MS Excel forms, validating the measurements against the GSDF automatically (Fig.4).

The results of several measurements on different computer monitors showed, that they could be easily brought to near-GSDF operating mode by simple visual adjustments.

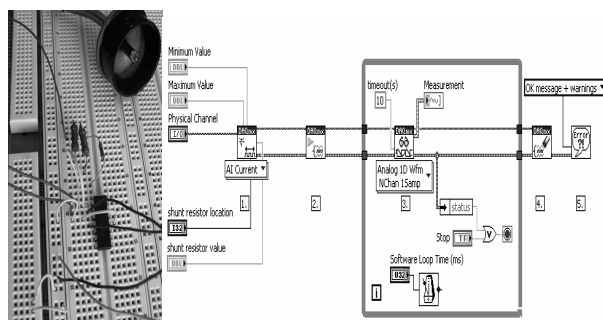


Fig.3. The prototype of the candelimeter in the virtualisation environment of the National Instruments, Inc.

**IHE Year 2
Softcopy Calibration Form**

Vendor / Device: NEC MultiSync V720 (po vizualaus derinimo)
 Date / Time: 2007-11-10, 09:05
 Performed by: KU Biofizikos stud. (Mindaugas Zikas)
 Ambient Light: 6,05

| | Lum [cd/m ²] | |
|------------------|--------------------------|--------------|
| measured DDL #1 | 0,16 | 0% (black) |
| measured DDL #2 | 0,20 | |
| measured DDL #3 | 2,55 | |
| measured DDL #4 | 5,09 | |
| measured DDL #5 | 10,19 | |
| measured DDL #6 | 13,05 | |
| measured DDL #7 | 19,10 | |
| measured DDL #8 | 25,78 | |
| measured DDL #9 | 34,38 | 50% (gray) |
| measured DDL #10 | 44,25 | |
| measured DDL #11 | 55,07 | |
| measured DDL #12 | 68,12 | |
| measured DDL #13 | 82,13 | |
| measured DDL #14 | 97,41 | |
| measured DDL #15 | 114,59 | |
| measured DDL #16 | 132,74 | |
| measured DDL #17 | 151,20 | 100% (white) |

determined Lmin: 0,16 cd/m²
 determined Lmax: 151,20 cd/m²
 calculated JNDmin: 177,50 (6,21 cd/m²)
 calculated JNDmax: 538,27 (157,25 cd/m²)
 calculated JND #: 360,77

overall Status: OK

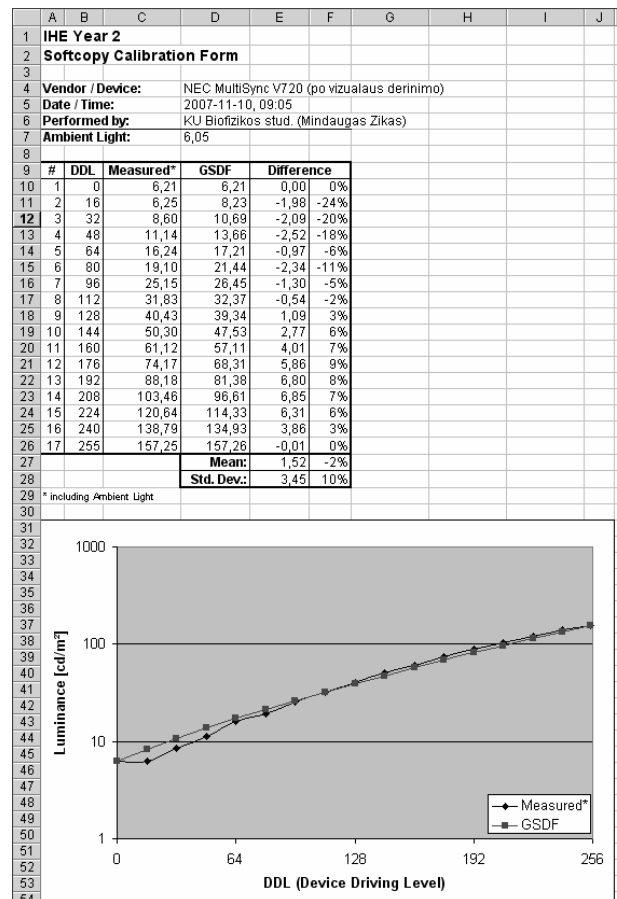


Fig.4. Screenshots of the IHE designed MS Excel forms with the entered data.

Furthermore, the attempt to design a measurement device was made using a photodiode and the measurement virtualisation environment (ELVIS and LabView) of the National Instruments, Inc. (see Fig.3). The calibration coefficient to convert the measurement results from current (in mA) to luminance (cd/m²) was set experimentally, by using the PTW Candelameter in the bright part of the measurement range.

The measurement results of CRT monitors obtained with the designed prototype were very similar to those, obtained using the PTW Candelameter-1.

However, the measurements of LCD displays (they are more and more widely used nowadays) require further investigation, as the measurement data were significantly lower, while the visual impression of display brightness was the same. The difference might be explained, e.g. by non-equally distributed in space light emission diagram of the LCD display.

4. Conclusions

1. The Greyscale Standard Display Function is based on Contrast Sensitivity of a human eye. It should be used for calibration (or at least adjustment) of imaging equipment in order to achieve normalised visualisation conditions and consistent image-base diagnostic conclusions.
2. By calibrating monitors and other devices, their performance becomes directly comparable. The continuous control over the device's lifetime allows detecting failures or degradation of the display quality.

3. Any means of calibration and quality control are better than the current situation when almost no standardized calibration is used in medical soft-copy imaging. In comparison with other fields like printing it is surprising that the introduction of these quality control techniques into the field of medical imaging takes so long.

5. References

1. ACR/NEMA. DICOM. PS3.14-2008: Grayscale Standard Display Function, NEMA, Rosslyn VA, 55p., 2008.
2. Marr D. "Vision". W.H.Freeman and Co, New York, 1982
3. Barten, P.G.J. Physical model for the Contrast Sensitivity of the human eye. Proc. SPIE 1666, 57-72 (1992)
4. Commission Internationale de l'Eclairage (CIE). CIE L*a*b* color space. In DIN 5033-3: Farbnessung; Farbmaßzahlen, 1992
5. Barten, P.G.J. Spatio-temporal model for the Contrast Sensitivity of the human eye and its temporal aspects. Proc. SPIE 1913-01 (1993)
6. J.Riesmeier, M.Eichelberg, P.Jensch. Quality control for softcopy environments using standardized display functions. In: Proceedings of the European Medical and Biological Engineering Conference EMBEC'99, Medical and Biological Engineering & Computing, vo.37, suppl. 2, pp.1546-1547, 1999.

NUCLEAR WEAPON-PRODUCED ^{14}C – APPLICATIONS AND LIMITATIONS OF BOMB-PULSE DATING

Kristina STENSTRÖM*

*Lund University, Department of Physics, Division of Nuclear Physics, Box 118, 221 00 Lund, Sweden

Abstract: Atmospheric nuclear weapons testing in the 1950's and early 1960's almost doubled the amount of ^{14}C in the atmosphere. The resulting ^{14}C bomb-pulse has shown to provide useful age information in *e.g.* forensic and environmental sciences, biology and geosciences. The technique is also currently being used for retrospective cell dating in man, to provide fundamental insight about the rate of formation of new cells in the human body. This paper describes the technique, some applications and discusses its limitations.

Keywords: ^{14}C , bomb-pulse dating, AMS

1. Introduction

The atmospheric testing of nuclear weapons added large amounts of the radioactive carbon isotope ^{14}C ($T_{1/2} = 5730$ years) during the mid and late 1950's and early 1960's. The highest level was observed in 1963, when the atmospheric ^{14}C specific activity was about twice the natural, the latter being about 230 Bq/kg C. Since 1963, the atmospheric ^{14}C specific activity has decreased due to uptake of CO_2 in oceans and biosphere, as shown in measurements of clean air CO_2 (see Fig. 1). The uptake of bomb ^{14}C in the biosphere forms the basis for bomb-pulse dating, which has found numerous applications in various areas of research. This paper presents an introduction to the technique and some of its applications. Limitations of the dating method are also addressed.

2. Production of ^{14}C in the atmosphere

^{14}C has existed in nature also before the nuclear era. It is produced naturally in the upper atmosphere through nuclear reactions between atmospheric nitrogen and neutrons generated in spallation reactions caused cosmic rays from space. Bomb- ^{14}C is produced by the same process but with neutrons originating from a nuclear detonation. The ^{14}C -atoms created – the natural as well as from bombs – are quickly oxidized into carbon dioxide, which through atmospheric circulation is mixed throughout the atmosphere. Prior to the nuclear era, the lower layers of the atmosphere contained *approximately* the same concentration of ^{14}C around the globe. For the bomb-pulse however, there are slight differences between the two hemispheres of Earth.

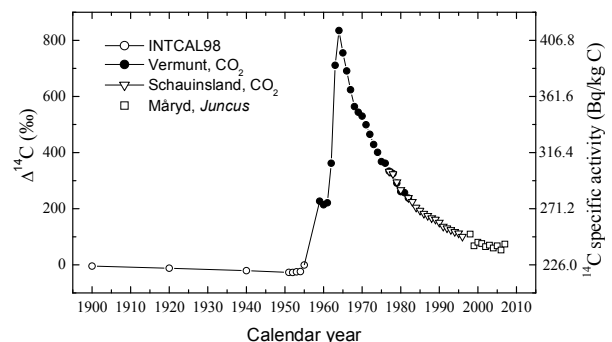


Fig. 1. ^{14}C specific activity in atmospheric carbon dioxide in the northern hemisphere during the 1900's. INTCAL98 are tree ring samples, while Vermont [1] and Schuainsland [1,2] are clean air data. Måryd is rush (*Juncus*), grown at the shore of a small pond at Måryd in southern Sweden [3].

^{14}C , natural as well a bomb- ^{14}C , also enters the biosphere and oceans. In the biosphere vegetation absorbs carbon dioxide, and as animals consume vegetation, ^{14}C will be incorporated into their tissues. To a first approximation, all living organisms contain about the same, very low concentration of ^{14}C : about 10^{-10} % of the total carbon supply is ^{14}C .

For organic material formed prior to the last century, the decreasing ^{14}C concentration after the death of the organism (due to radioactive decay) can be used to determine its age. This is known as radiocarbon dating, which was developed during 1945-1950, and which is

widely used in archaeology and geology. Willard Frank Libby, the inventor of the technique, received the Nobel Prize in chemistry in 1960 for his work on radiocarbon dating.

Traditional radiocarbon dating has an error of some tens of years, and cannot be used for dating of recent, modern material. The bomb-pulse, however, with its sharply declining curve, is ideal for dating of organic matter formed after 1963. The resolution the bomb-pulse dating is a subject discussed later in this paper.

3. Methods

In the early bomb-pulse applications, ^{14}C was quantified in gas proportional counters by measuring the beta decay from ^{14}C . Long measuring times (days) and large samples sizes (in the order of 1 g of carbon), limited the possible applications of the technique until accelerator mass spectrometry (AMS) was invented in the late 1970ies.

AMS, which quantifies ^{14}C by measuring the ratio between the carbon isotopes in a sample, is the most sensitive technique for measuring ^{14}C , see *e.g.* Ref. [4]. Because of its extremely high sensitivity, ^{14}C -AMS is an excellent tool for studies of natural processes and for tracer studies using bomb-pulse ^{14}C , especially if the sample material size is in the mg-size range or less (actually as little tens of micrograms of carbon can be measured with AMS). AMS is about 1000 times more sensitive than any radiometric method and has the outstanding ability to quantify ^{14}C down to levels of 10^{-18} moles, which is in the order of only one million molecules. Today, AMS is a fast-growing field of science with over 80 machines worldwide. The majority of them are used for ^{14}C dating.

4. Some applications of the bomb-pulse

Initially the bomb-pulse was mainly used for studies of the global carbon cycle, *e.g.* of the exchange rates of CO_2 between the atmosphere and the oceans. These studies have gained valuable information for climate research on the greenhouse effect.

Because ^{14}C is radioactive, studies were also performed to assess the radiation dose to the population from the bomb-pulse. In these studies, the bomb peak was also used to estimate turnover times of carbon in various biological tissues, see *e.g.* Refs. [5,6]. Already in 1972, Harkness and Walton recognized that the bomb-pulse can be an ideal kinetic tracer for various processes in the human body [6]. As an example, in one study (published in 1983) the bomb pulse was used to estimate the growth rate of human gall stones formed in the gallbladder [7].

Radiocarbon dating of modern objects using the bomb-pulse has found several other applications, *e.g.* in forensic science; Wild *et al* [8] has *e.g.* demonstrated that human hair is a good indicator of the year of death. Spalding *et al* reports on the use of bomb- ^{14}C in tooth

enamel to determine the age of unidentified victims [9]. The bomb-pulse has also been used to check vintages of wine to reveal wine forgeries [10,11] or demonstrate the presence of unauthorized additives in wine [11].

Zoppi *et al* [11] also reports on the use of the bomb-pulse to trace the distribution pathways of illicit drug samples, like cocaine and opium; ^{14}C analysis can reveal when these naturally derived drugs were produced, and consequently if they have been stockpiled or directly transferred to a market. Geyh has used the bomb-pulse for the identification of furs of illegally hunted animals, when court cases need to establish the year the animals were killed [12].

Lately, there has been an increasing interest to use the bomb-pulse for retrospective age determination of human cells, in order to provide fundamental insight on the formation of new cells in the body. Lovell *et al* have used to bomb-pulse to determine the age of senile plaques and neurofibrillary tangles in Alzheimer's disease [13], Spalding *et al* have performed investigations of the human brain [14] and the dynamics of fat cell turnover [15]. Lynnerup *et al* have studied the carbon turnover in the human eye lens crystallines [16].

Lately, so called bio-based testing using the bomb-pulse has been established. Bio-based testing can be used *e.g.* to protect the interests of bio-mass producers, by certifying that their products are free from cheaper, synthetic ethanol produced from petroleum resources.

5. Limitations of the bomb-pulse

Bomb-pulse dating uses precise measurements of the declining ^{14}C concentration in atmospheric CO_2 collected at clear air sites in different geographical zones (see *e.g.* [17,18]). However, what is not always recognized, the matter is complicated by in some cases significant local variations in the ^{14}C specific activity of air and variations in foodstuff. It is important to evaluate how these variations may introduce variations in ^{14}C specific activity between different individuals and how this affects the precision of bomb-pulse dating.

The main pathway by which ^{14}C enters the body is normally ingestion. The diet is thus the most important source of ^{14}C in man. Inhalation and dermal absorption are minor sources of ^{14}C in man, but may be significant for *e.g.* workers handling ^{14}C -labelled materials.

Variation of ^{14}C specific activity in diet may be one limiting factor for the precision of bomb-pulse dating. The variations may result from several different factors and sources. Obvious ones are average age of the food (giving different ^{14}C specific activity) and relative amount of the different ingested food components. Below some other factors and phenomena with the potential of affecting the ^{14}C levels in man are discussed.

5.1 Lowered environmental levels of ^{14}C

The first major anthropogenic effect on the ^{14}C levels in nature was initiated with the beginning of the industrial revolution. The large-scale combustion of fossil fuels (such as coal, gas and oil, which originate from very old geological reservoirs and in which essentially all radioactive carbon has decayed) introduced ^{14}C -free CO_2 into the atmosphere, increasing the CO_2 concentration of the atmosphere. This increase of the stable carbon isotopes, which results in a decrease of the ^{14}C specific activity, is called the Suess effect and has been detected by analysis of tree rings back to 1850 AD [19]. Between 1950 and 1950 AD, the Suess effect increased in magnitude and the decrease of atmospheric ^{14}C specific activity amounted to about 3%. In Fig. 1 this trend is visible.

Local environmental decrease in ^{14}C specific activity can also result from several other phenomena. Considerably lowered ^{14}C concentrations (up to several percent) compared to clean air sites has been measured in vegetation in heavily industrialised regions, see *e.g.* Refs. [20,21]. Also plants grown close to active volcanoes can display a decrease in ^{14}C : Ref [22] reports depletion of ^{14}C of up to 40%. The human diet may also contain ingredients of petrochemical origin (botanical extracts and essential oils can be replaced by materials that can be inexpensively synthesized from fossil fuels, and green houses growing vegetables may use fossil CO_2).

5.2 The reservoir effect

A most significant factor, which determines the ^{14}C specific activity of the diet, is what reservoir the diet originates from. Diet from terrestrial sources has different ^{14}C content than aquatic sources due to the non-equilibrium in ^{14}C specific activity between atmosphere (where the bomb- ^{14}C was produced) and aquatic reservoirs during the bomb pulse. This is powerfully demonstrated *e.g.* by Harkness and Walton [6], where fish caught in the late 1960ies showed levels on the order of 240 Bq/kg C, compared to about 360 Bq/kg C for beef. Thus, the percentage of sea foods in the diet is essential for bomb-pulse dating applications, and can probably lead to inter-individual variations of ^{14}C in man. This factor is probably one of the most important when it comes to the precision of bomb-pulse dating.

5.3 Route through the food chain

Also the length of route of ^{14}C through the food chain – from atmospheric CO_2 and eventually to man – can affect the ^{14}C specific activity of the diet. The carbon reaching man and animals may come directly from plants. However, it can also come from a more prolonged route through the food chain: the route is extended when the diet includes grass-eating mammals, and even longer in case of meat-eating mammals. Thus, due to the declining bomb-pulse curve, a varied diet of meat and vegetables may have a somewhat different ^{14}C

specific activity than a pure vegetarian diet. For meat-eaters, the turnover time of carbon in the consumed animal's cells also affects the ^{14}C -specific activity in the diet. This effect is however not believed to be as significant as the reservoir effect.

5.4 Anthropogenic sources of ^{14}C

During normal operation of nuclear power reactors, ^{14}C is produced by neutron activation of mainly nitrogen, oxygen and carbon in the fuel, the moderator, the coolant, and in construction materials of the reactors. The amounts of ^{14}C produced vary considerably between different reactors, depending on factors such as reactor type as well as operational parameters and concentrations of nitrogen impurities in the various parts and systems of the reactors [24].

The major part of the ^{14}C produced in nuclear reactors is retained in solid or liquid waste, *e.g.* spent ion exchange resins, which may end up in geological waste disposals. Part of the ^{14}C produced in some of the world's reactors is released from fuel reprocessing plants into the atmosphere, and also to the hydrosphere. However, a fraction of the ^{14}C created is also continuously released at the reactor site during normal operation, mainly as airborne and, to a lesser extent, as waterborne effluents in various chemical forms.

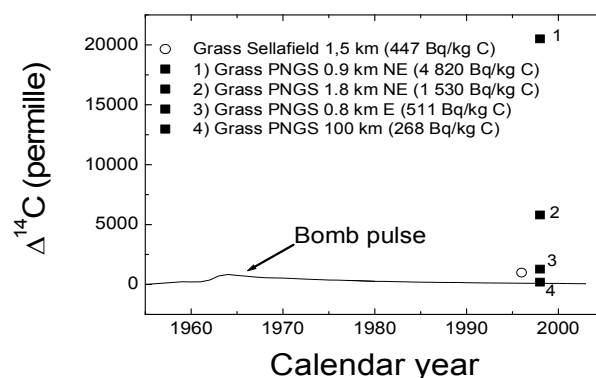


Fig. 2. Example of measured ^{14}C levels in the vicinity of Sellafield, a reprocessing plant for spent nuclear fuel (UK), and Pickering Nuclear Generating Station (PNGD (Canada) [23].

^{14}C in man may be affected for individuals living close to nuclear installations, see *e.g.* Ref. [3]. Maximum excess in vegetation is often found within a few km of nuclear power plants (depending *e.g.* on reactor type and operation, stack height and weather conditions), thus limiting the number of persons that live in exposed areas. Typical values for light-water reactors are maximum excesses of 10% within a few km of the power plant [23].

Heavy-water reactors (HWRs) may serve as a more extreme case, since these reactors are known to produce relatively more ^{14}C than most other types of reactors [24]. Milton *et al* [25] report an excess of up to about 5 000 % (12 950 Bq/kg C, year 1992) in fruit grown at about 1 km from Pickering Nuclear Generating Station

(PNGS, Canada), one of the largest nuclear facilities in the world using HWRs. In Ref. [23] values for longer distances from PNGS are presented; 1530 ± 50 Bq/kg C at 2 km from the facility in year 1998, and even at a distance of 100 km an excess of 7 % was found (268 ± 5 Bq/kg), see Fig. 2.

Leprieur *et al* [26] have reported a rather extreme case of ^{14}C contamination in the surroundings of a company specialized in organic radioactive molecule synthesis. Within a 50 m radius around the facility, 66 000 Bq/kg C was found in soils, and 25 000 Bq/kg C in plants, which is more than a hundred times the clean air ^{14}C levels.

The ^{14}C released from nuclear facilities has the potential of reaching man mainly through ingestion. It is however not well-known what magnitudes that might be found, due to lack of measurements in man. However, the most extreme human levels of ^{14}C are expected to be found in personnel working in a ^{14}C -enriched environment. Possible ^{14}C contamination in personnel working with ^{14}C -containing material is probably not routinely monitored at any workplace, and very few data exist on the levels that may occur. In Brodsky [27] a US university medical centre was found highly contaminated throughout by tritium and ^{14}C compounds. Incidents or accidents with ^{14}C are somewhat more frequently described, such as a high-level contamination of personnel in a laboratory producing ^{14}C -labelled barium carbonate [28]. Stenström *et al* [29] has presented ^{14}C levels in hair and urine from ^{14}C -using workers, showing a maximum ^{14}C excess of 63% in hair and 400% in urine.

6. Conclusions

Variations of ^{14}C in the environment exist, which significantly affects the shape of bomb-pulse locally compared to clean air data, and which may affect the ^{14}C levels in all types of living organisms. There are also cases, such as with workers handling ^{14}C -labelled material, where greatly enhanced ^{14}C levels can be seen in man. However, persons exposed to ^{14}C occupationally are only a small minority, and – for larger population groups and for evaluating the precision of bomb-pulse dating – variations in ^{14}C concentration in the diet are perhaps of more interest.

I argue that the major issue with bomb-pulse dating is that it is not well known how these local variations of ^{14}C in ambient carbon and in dietary carbon affect the individual human ^{14}C concentration, and how applicable clean air data of ^{14}C from atmospheric CO_2 is to humans.

More work need to be done in this area, for instance modelling ^{14}C levels in different diets. Perhaps more measurements are also needed. One approach to evaluate differences in man would be to analyse the ^{14}C concentration in hair in now living subjects. Even better would be if we could find older human hair samples,

from when the yearly decline of the bomb-pulse was sharper than today.

Workers handling ^{14}C -containing material, and perhaps their family members, can serve as a worst-case scenario for the bomb-pulse dating method.

Despite all these question marks, I am convinced that bomb-pulse dating is a very valuable tool that still has a lot to offer science.

7. References

1. Levin I., Kromer B., Schoch-Fischer H., Bruns M., Münnich M., Berdau D., Vogel J.C and Münnich K.O. 25 years of tropospheric ^{14}C observations in central Europe. *Radiocarbon* 27:1 (1985) 1-19.
2. Levin, I. and Kromer, B. Twenty years of high precision atmospheric $^{14}\text{CO}_2$ observations at Schauinsland station, Germany. *Radiocarbon* 39:2 (1997) 205-218.
3. Stenström K., Leide Svegborn S., Magnusson Å., Skog G., Zakaria M., Mattsson S. Lund University, Internal report LUNFD6(NFFR-3101)/1-47/(2006). SSI project report SSI P 1378. 2006.
4. Stenström K. and Mattsson S. Accelerator mass spectrometry (AMS) for pharmaceutical microdosing studies. Proceedings of the 5th International Conference on Medical Physics in the Baltic States. Kaunas, Lithuania, 5-6 October, 2007. ISSN 1822-5721.
5. Harkness D.D. and Walton A. Carbon-14 in the biosphere and humans. *Nature* 223 (1969) 1216-1218.
6. Harkness D.D. and Walton A. Further investigations of the transfer of bomb ^{14}C to man. *Nature* 302 (1972) 302-303.
7. Druffel E.M. and Mok H.I.Y. The history of human gallstones: applications of the post-bomb radiocarbon signal. *Radiocarbon* 25:2 (1983) 629-636.
8. Wild E., Arlamovsky K.A., Gosler R., Kutschera, A. Priller W., Puchegger S., Rom W., Steier P. and Vycudilik W. ^{14}C dating with the bomb peak: an application to forensic medicine. *Nucl. Instr. and Meth. B* 172 (2000) 944-950.
9. Spalding K., Buchholz B., Bergman L.-E., Druid H. and Frisén J. Age written in teeth by nuclear tests. *Nature* 437 (2005) 333-334.
10. Burchuladze A.A., Chudý M., Eristavi I.V., Pagava S.V., Peovinec P., Šivo A. and Togonidze G.I. Anthropogenic ^{14}C variations in atmospheric CO_2 and wines. *Radiocarbon* 31:3 (1989) 771-776.
11. Zoppi U., Skopec Z., Skopec J., Jones G., Fink D., Hua Q., Jacobsen G., Tuniz C. and Williams A. Forensic applications of ^{14}C bomb-pulse dating. *Nucl. Instr. and Meth. B* 223-224 (2004) 770-775.
12. Geyh M.A. Bomb radiocarbon dating of animal tissues and hair. *Radiocarbon* 43:2B (2001) 723-730.
13. Lovell M.A., Robertson J.D., Buchholz B.A., Xie C. and Markesbery W.R. Use of bomb-pulse carbon-14 to age seile plaques and neurofibrillary tangles in

- Amlzheimer's disease. *Neurobiology of Aging* 23 (2002) 179-186.
14. Spalding K.L., Bhardwaj R.D., Buchholz B.A., Druid H. and Frisén J. Retrospective birth dating of cells in humans. *Cell* 122 (2005) 133-143.
 15. Spalding K.L. et al. Dynamics of fat cell turnover in humans. *Nature* 453 (2008) 783-787.
 16. Lynnerup N., Kjeldsen H., Heegaard S., Jacobsen C. and Heinemeier J. Radiocarbon Dating of the Human Eye Lens Crystallines Reveal Proteins without Carbon Turnover throughout Life. (2008) *PloS ONE* 3(1): e1529. Doi: 10.1371/journal.pone.0001529.
 17. Hua Q. and Barbetti M. Review of tropospheric bomb ^{14}C data for carbon cycle modelling and age calibration purposes. *Radiocarbon* 46:3 (2004) 1273-1298.
 18. Levin I. and Kromer B. The tropospheric $^{14}\text{CO}_2$ level in mid-latitudes of the northern hemisphere (1959-2003). *Radiocarbon* 46:3 (2004) 1261-1272.
 19. Suess H.E. Radiocarbon concentration in modern wood. *Science* 122 (1955) 415-417.
 20. Pawelczyk S. and Pazdur A. Carbon isotopic compositions of tree rings as a tool for biomonitoring CO_2 level. *Radiocarbon* 46:2 (2004) 701-719.
 21. Rakowski A., Kuc T., Nakamura T., Pazdur A. Radiocarbon concentration in the atmosphere and modern tree rings in the Krakow area, southern Poland. *Radiocarbon* 46:2 (2004) 911-916.
 22. Pasquiere-Cardin A., Allard P., Ferreira T., Hatté C., Coutinho R., Fontunge M. and Jaudon M.J. Magma-derived CO_2 emissions recorded in ^{14}C and ^{13}C content of plants growing in Furnas calda, Azores. *J. Volc. Geoth. Res.* 92 (1999) 195-207.
 23. Stenström K., Erlandsson B., Mattsson S., Thornberg C., Hellborg R., Kiisk M., Persson P. and Skog G. Lund University, Internal report LUNFD6/(NFFR-3079)/1-44/(2000), SSI project report SSI P 928.95. 2000.
 24. Magnusson Å. ^{14}C generated by nuclear power reactors – generation and characterization of gaseous, liquid and solid waste. Doctoral dissertation, ISBN 978-91-628-7248-9. Lund University, 2007.
 25. Milton G.M., Kramer S.J., Brown R.M., Repta C.J.W., King K.J. and Rao R.R. radiocarbon dispersion around Canadian nuclear facilities. *Radiocarbon* 37:2 (1995) 485-496.
 26. Leprieur F., Linden G. and Pasquier J.L. Radioecology and health impact of the carbon-14 contamination on the Ganagobie site (Provence, France). *Radioprotection* 38:1 (2003) 13-28.
 27. Brodsky A., Management lessons from radiation accidents. *RSO Magazine* 10:6 (1995) 4-10.
 28. Kramer G.H., Badreddine A., Tran T. and Meyerhof D. Dosimetry of an incident involving ^{14}C . *Health Physics* 70:3 (1996) 418-424.
 29. Stenström K., Leide-Svegborn S. and Mattsson S. Low-level occupational exposure of ^{14}C – results from a pilot study. *Rad. Prot. Dos.* 2008; doi: 10.1093/rpd/ncn054.

PLUTONIUM SPECIATION AND ITS ENVIRONMENTAL FATE

Rūta DRUTEIKIENĖ*, Benedikta LUKŠIENĖ*

* Institute of Physics, Savanorių pr. 231, LT-02300 Vilnius, Lithuania

Abstract. The paper deals with the sequential extraction analysis of soddy-grassland and forest soil, artificially contaminated with ^{239}Pu in oxide, nitrate and chloride forms and exposed under environmental conditions for about a year. Partitioning of ^{239}Pu was defined for seven reagent fractions: water soluble, ion exchangeable, carbonates, Fe-Mn oxides, acid soluble, organic matter and residue. Transformation of initial forms of ^{239}Pu via sequential extraction was evaluated. Referring to the calculated mobility coefficients, the determined order mobility of ^{239}Pu compounds was as follows: $^{239}\text{PuCl}_3$ (soddy soil) > $^{239}\text{Pu}(\text{NO}_3)_4$ (soddy soil) > $^{239}\text{Pu}(\text{NO}_3)_4$ (forest soil) > $^{239}\text{PuO}_2$ (soddy soil).

Keywords: sequential extraction, ^{239}Pu partitioning, transformation of chemical forms.

1. Introduction

In the transuranium series plutonium as environmental contaminant is the major subject of environmental science. The atmospheric weapons tests, nuclear accidents and working of nuclear installations nowadays have made plutonium isotopes predominant in radioecological research than the other transuranic elements [1]. Over one third of the energy produced in most nuclear power plants comes from plutonium. Plutonium is a by-product of the fission process in nuclear reactors, due to neutron capture by uranium-238 in particular. When operating, a typical nuclear reactor contains within its uranium fuel load about 325 kilograms of plutonium, with plutonium-239 being the most common isotope [2]. In commercial power-plants and research applications plutonium generally exists as plutonium oxide (PuO_2), a stable ceramic material with an extremely low solubility in water or body fluids.

Historically, scientific interest of plutonium has focused on two areas: (1) its application as a tracer of environmental processes, and (2) its impact on human health through radiation exposure.

Plutonium is radiologically hazardous, particularly if inhaled. There are three principal routes by which plutonium can reach human beings: ingestion, contamination of open wounds, inhalation.

Ingestion is not a significant hazard, because plutonium passing through the gastro-intestinal tract is poorly absorbed and is expelled from the body before it can do harm. Contamination of wounds has been prevented by the use of the remote handling, protective clothing and extensive health monitoring procedure.

The main threat to humans comes from inhalation. While it is very difficult to create airborne dispersion of

a heavy metal like plutonium, certain forms, including the insoluble plutonium oxide, at a particle size less than 10 microns, are a hazard. If inhaled, much of the material is immediately exhaled or is expelled by mucous flow from the bronchial system into the gastro-intestinal tract, as with any particulate matter. Some however will be trapped and readily transferred, first to the blood or lymph system and later to other parts of the body, notably the liver and bones. It is here that the deposited plutonium's alpha radiation may eventually cause cancer [3].

For the present, the main amount of environmental plutonium is cumulated by soil and sediment except a small part of it occurring in a ground-level air because of the phenomenon of resuspension [4].

The mobility, accumulation and bioavailability of radionuclides is directly depended on physico-chemical forms or speciation of a given element. Different approaches are used for contaminated environmental samples analysis. To obtain information on radionuclide species, size and charge fractionation techniques are commonly applicable. The size fractionation methods as well as filtration, continuous low centrifugation, ultra centrifugation, gel chromatography is to be used for separation of particles or colloids in water. Exchange chromatography, liquid-liquid extraction, sequential extractions, crown ether chromatography, electrochemical methods and ion selective electrodes usually are recommended for charge fractionation purposes [5]. To obtain knowledge of the biological availability, accumulation and migration processes of trace metals within a specific soil or sediment the chemical methods as the sequential extractions or "fractionation" has been applied. The process of operationally defined selective dissolution of macro-

scale geochemical components of solid-phase matrix materials allows assessing the geochemical host phases of contaminants [6]. The existence of a particulate trace metal in soil or sediments in exchangeable, carbonate-bound, oxide-bound, organic matter-bound, or incorporated in crystal lattice forms has been investigated since 1973 [7-9]. After the sequential extraction procedure was developed [6, 9], the application of the method to radionuclides in various ecosystems was started [10-17].

This study focuses on the investigation of the behaviour of the known ^{239}Pu soluble and insoluble forms in soil after about a year of exposure under natural field conditions, by means of the sequential extraction method.

2. Experimental

2.1 Soil samples

In order to better understand the mobility of plutonium in soil the field experiment was performed [18]. Two columns (diameter 10 cm, length 20 cm) of nondestroyed soddy soil and 1 column of forest soil contaminated with ^{239}Pu in oxide, chloride and nitrate forms were stuck at all length in soil and left for about one year period. One column of soddy soil contaminated with ^{239}Pu in nitrate form was exposed for about a month longer. After exposition each column was divided into 4 layers, 5 cm each. The soil was dried at room temperature, ground and sieved to remove the plants and roots. Then the samples were homogenized and stored for subsequent analysis.

2.2 Sequential extraction procedure

For analysis the 1st layer of column was used. Selective extractants were chosen basically according to Tessier et al [9]. The principal scheme and geochemical phases leached by extractants are presented in Table 1.

Table 1. Scheme of sequential extraction

| Sequential extraction fractions | Geochemical phase |
|--|---|
| Double distilled water | Solubility of solids, trace elements in ionic phase and soluble complex compounds |
| 1 mol/L ammonium acetate (pH7) | Exchangeable ions |
| 1 mol/L acetic acid | Carbonates, some Fe and Mn oxides |
| 0,04 mol/L hydroxylamine chloride in 25% acetic acid (1:1) | Iron and manganese oxides (moderately reducible phase) |
| 2 mol/L hydrochloric acid | Acid-soluble compounds |
| 30% hydrogen peroxide, pH2 with HNO_3 | Organics, sulfides |
| HNO_3 and HF | Lithogenous fraction |

All the extraction procedures were conducted at room temperature shaking 20 g of soil with selective reagent

for an hour. The solids to extractant ratio were kept at 1:10. The extractant was separated by filtration and the residue from the previous step was washed twice with distilled water. After the filtration and washing steps, filters with residual solids were reintroduced in to the reaction vessel for the next extraction.

2.3 Determination of plutonium

Each fraction of sequential extraction was spiked with the ^{242}Pu yield-tracer and evaporated. Plutonium isotopes from this medium were leached with 8 mol/L HNO_3 solution under heating. Plutonium anion exchange separation was performed using Dowex 1x8 anion resin in NO_3^- form and bearing into consideration the relevance of the stabilization of Pu valence forms. For alpha spectrometric measurements plutonium sources were completely prepared by electrodeposition on polished stainless steel planchets.

The alpha spectrometric measurements were carried out applying the Cambera PD detector (area 450 mm², resolution 25-27 keV, alpha counting efficiency 25%). The detection limit for a counting time of 86,400 seconds was about 10^{-3} Bq of $^{239,240}\text{Pu}$.

3. Results and discussion

After exposition the largest quantity of ^{239}Pu released on the column surface in different chemical forms ($^{239}\text{PuCl}_3$, $^{239}\text{Pu}(\text{NO}_3)_4$, $^{239}\text{PuO}_2$) was obtained in the upper (0-5 cm) soil layer [18]. The top layer of soddy soil accumulated 92% of $^{239}\text{PuO}_2$, 81% of $^{239}\text{Pu}(\text{NO}_3)_4$ and 44% of $^{239}\text{PuCl}_3$. The forest soil top layer contain 88% of $^{239}\text{PuO}_2$, 82% of $^{239}\text{Pu}(\text{NO}_3)_4$ and 61% of $^{239}\text{PuCl}_3$.

The results of ^{239}Pu disposition amongst sequential extraction phases from the soil samples, contaminated with ^{239}Pu in chloride, nitrate and oxide forms and exposed for about a year under natural environmental conditions are summarized in Table 2.

Sometimes the water-soluble fraction is not used in sequential extraction studies, but is necessary for the hydration and swelling of clay minerals in accordance with Shultz et al [6] at the beginning of the extraction sequential sample soak period. As can be seen from Table 2 0,2% of ^{239}Pu from $^{239}\text{Pu}(\text{NO}_3)_4$, 1,2% from $^{239}\text{PuO}_2$ in soddy soil and 1,0% of ^{239}Pu from $^{239}\text{Pu}(\text{NO}_3)_4$ in forest soil occurred in the distilled water fraction. This result is comparable to the ^{239}Pu content in water-soluble fraction obtained in alluvial gley soil samples [19] in soddy podzolic soil and 0,6% in grey forest soil [5,12]. A significantly higher amount of ^{239}Pu was found in the distilled water fraction from soddy soil as contaminated with $^{239}\text{PuCl}_3$, it came up to 6,0%. This result is comparable to the ^{239}Pu content in water-soluble fraction obtained in alluvial gley soil samples [13] in soddy podzolic soil and 0,6% in grey forest soil [10,17].

1 mol/L ammonium acetate (pH 7) was used to extract exchangeable cations (it can also partially dissolve some carbonates). ^{239}Pu share from all studied samples in this fraction varied from 0,5 to 15,8%. These results are similar to those of researchers [10, 11, 13], where

Table 2. Percentage distribution of ^{239}Pu activity found in sequential extraction fractions

| Fraction | Soddy soil | | Forest soil | |
|---|----------------------|-----------------------|----------------------------------|----------------------------------|
| | $^{239}\text{PuO}_2$ | $^{239}\text{PuCl}_3$ | $^{239}\text{Pu}(\text{NO}_3)_4$ | $^{239}\text{Pu}(\text{NO}_3)_4$ |
| Water soluble | 1,2±0,1 | 6,0±0,4 | 0,20±0,03 | 1,0±0,2 |
| Exchangeable | 0,5±0,06 | 11,0±0,4 | 16,0±0,8 | 1,0±0,1 |
| Bound to carbonates (specifically adsorbed) | 0,50±0,08 | 5,0±0,3 | 1,0±0,1 | 2,0±0,2 |
| Fe-Mn oxides | 1,0±0,1 | 2,0±0,1 | 0,20±0,04 | 1,0±0,1 |
| Acid soluble | 4,0±0,3 | 11,0±0,5 | 14,0±0,3 | 17,0±1,5 |
| Fixed, among them: | 93,0±6,0 | 67,0±6,0 | 69,0±7,0 | 78,0±7,0 |
| - bound to organic matter | 12,0±3,0 | 3,0±3,3 | 14,0±3,0 | 8,0±2,0 |
| - residue | 81,0±3,0 | 54,0±2,7 | 55,0±4,0 | 70,0±5,0 |

percentage distribution of ^{239}Pu in carbonate fraction was of the order of 0,5-5,0%, while other authors obtained a higher plutonium amount in this fraction 30-35% [6] and 11% [19]. In our study a comparatively low amount of ^{239}Pu in acetic acid fraction can be explained by low pH values (pH 4,4 and pH 4,6) of the studied soils. Bunzl et al [13] did not include the extractant for leaching carbonate fraction due to the pH values of 3,2; 3,6; 3,9 of soil. Researchers have obtained different percentage distribution of plutonium bounded to Fe-Mn oxides.

It varied in a wide range: 6,4% [19], 6-7% [20], 30-35% [6]. The results of our investigation into ^{239}Pu partitioning showed lower percentage amount of ^{239}Pu in Fe-Mn oxides fraction (0,2-2,0%). Acid soluble fraction contained from 4,0 to 17,0% of ^{239}Pu , when 2mol/L HCl for leaching of studied soils was used. The lowest percentage amounts of ^{239}Pu by this extractant were extracted from samples contaminated with $^{239}\text{PuO}_2$ (Table 2). 2 mol/L HCl leached ^{239}Pu from soddy soil and forest soil contaminated with ^{239}Pu in nitrate form 14,0 and 17,0%, respectively. 4,5% of plutonium from soddy podzolic soil and 1,9% of this radionuclide from grey forest soil [17] and 3,1% of plutonium from grassland soil [10] were found to be soluble in 1 mol/L HCl. About 25% of $^{239,240}\text{Pu}$ from Venice canal sediment were dissolved in 8 mol/L HNO_3 [20]. Bunzl et al [13] obtained 12% to 57% of persistently bounded $^{239,240}\text{Pu}$ in different forest soil layers when 7 mol/L HNO_3 extractant was used. Thus, the solubilization of plutonium compounds in acid fraction depends on the acid concentration used. It was also stressed [13] that persistently bound form could be taken as a residual.

Low percentage amount of ^{239}Pu associated with organic matter (Table 2) is supposedly caused by the use of acidic hydrogen peroxide fraction at room temperature. Obviously a different ratio between ^{239}Pu bound to organic matter and the ^{239}Pu content in residual fraction would be obtained in our research if the acidic hydrogen peroxide at 85°C was used. For comparison, $^{239,240}\text{Pu}$ bound to organic matter in the sediment was determined to be 10-12% [6], in different soil layers from 87 to 60 and 30% [13], in alluvial gley soil – 42,5% [19] and in Cumbrian soils[21]: (64±1)% in gley soil, (68±3)% in sand, (53±2)% in woodland, (59±2) % in pasture soil.

The presence of radionuclide in connection with organic substance (humic and fulvic acids) defines the accumulation and migration processes of the

radionuclides [17]. Nevertheless, the investigation of heterogenic interaction of ionic forms of plutonium (IV) with insoluble in acidic media humic substances showed irreversible process of plutonium adsorption by humic acids [22]. It was indicated that humic substances could be considered as multifunctional ionexchangers. Therefore plutonium demonstrates steady attachment in the structure of humic substances due to the processes of complexes and chelates formation.

On the basis of the data obtained by means of the sequential analysis [10], the mobility coefficient of ^{239}Pu was calculated as the ratio of the sum of water soluble and exchangeable forms to the sum of acid soluble and fixed forms (1):

$$K_{mob} = \frac{\text{watersoluble} + \text{exchangeable forms}}{\text{acidsoluble} + \text{fixed forms}} \quad (1)$$

Coefficients of plutonium mobility in our study varied in the range of $3,6 \cdot 10^{-1}$ and $3,3 \cdot 10^{-2}$. According to the coefficients of ^{239}Pu mobility (Fig.1), the following order of mobility of ^{239}Pu compounds which were brought upon the soil a year ago can be determined: $^{239}\text{PuCl}_3$ (soddy soil) > $^{239}\text{Pu}(\text{NO}_3)_4$ (soddy soil) > $^{239}\text{Pu}(\text{NO}_3)_4$ (forest soil) > $^{239}\text{PuO}_2$ (soddy soil).

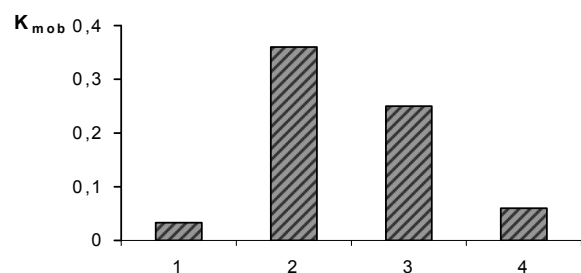


Fig. 1. Coefficients of ^{239}Pu in different forms in soil: 1- $^{239}\text{PuO}_2$ (soddy soil); 2- $^{239}\text{PuCl}_3$ (soddy soil); 3- $^{239}\text{Pu}(\text{NO}_3)_4$ (soddy soil); 4- $^{239}\text{Pu}(\text{NO}_3)_4$ (forest soil)

4. Conclusions

Besides the gained evidence that radionuclides transformation into mobile forms starts taking place when soil particles are destroyed under the influence of weathering, ageing, selfdispersion, leading and other processes [23] the achieved results are the sufficient basis to observe the versus process, i.e. transformation of mobile forms of plutonium to less mobile forms. Although some of the used extractants in our study were not highly specific for separate geochemical phases but generalizing the obtained results the following conclusions can be made.

The sequential analysis method allowed us to follow the transformation of chemical forms of plutonium. After staying in soil for a year under natural meteorological conditions insoluble $^{239}\text{PuO}_2$ and soluble $^{239}\text{PuCl}_3$ and $^{239}\text{Pu}(\text{NO}_3)_4$ have thus changed their mobility: 2,0% of plutonium oxide was transferred to the mobile forms; 22,0% of plutonium chloride, 17,0% of plutonium nitrate in soddy soil and only 4,0% of plutonium nitrate in forest soil remained in the mobile phase;

as it could be expected the largest percentage amount of ^{239}Pu in a fixed form was determined from $^{239}\text{PuO}_2$ (93,0%) but for the other plutonium compounds ($^{239}\text{PuCl}_3$, $^{239}\text{Pu}(\text{NO}_3)_4$) which had been used for the soil contamination this value was also sufficiently high and varied from 67,0 to 78,0%.

5. References

1. Yu Yu-Fu B Salbu H.E. Bjornstad J., Radioanal. Nucl. Chem., 148 (1991)163
2. Management of separated plutonium.// OECD/NEA Paris (1997)
3. The Toxicity of Plutonium. //Medical Research Council, London (1975)
4. A.Komosa // J., Radioanal. Nucl. Chem., 252 (2002) 121
5. B.Salbu // J.of Environmental Radioactivity, 96 (2007) 47-53
6. 4.Schultz M.K., BurnettW.C. and Inn K.G.W.// J. Environ. Radioactivity, 40 (1988), 2, 155-174
7. McLaren R.G. and Crawford D.V.// J. Soil. Sci. 24 (1973) 172-181.
8. Gibbs R.J.// Geol. Soc. Am. Bull. 88 (1977) 829-843.
9. Tessier A.P., Campbell G.C. and Bisson // Anal. Chem., 51 (1979) 844-851.
10. Martiušov V.V., Spirin D.A., Bazylev V.V., Fedorova T.A., Martiušov V.Z.,Panova L.A. // Ecology, 2 (1995) 110-113 (in Russian).
11. Pavlotskaja F.I., Goryachenkova T.A., Myasoedov B.F.// J. Radioanal. And Nucl. Chemistry, Articles, 147 (1991) 1, 133-140.
12. Konopliov A.V., Borzilov V.A., Bobovnikova C.I., Virčenko E.P, Popov V.E., Kutniakov I.V., Čumirev V.B. // Meteorology and hydrology, 12 (1988) 63-74, (in Russian).
13. Bunzl K., Kracke W., Schimmack W. and Zelles L. // J. Environ, Radioactivity, 39 (1998) 1, 55-68.
14. Riise G., Bjornstad H.E., Lien H.N., Oughton D.H., Salbu B. // J. Radioanal and Nucl. Chem., 142 (1990) 2, 531-538.
15. Lukšienė B.J., Shvedov V.P.// J.Radiochem. and Nucl. Chem., Articles, 91 (1985) 1, 215-219.
16. Tomašek M., Rybaček K., Wilhelmova L. // J.Radioanal Nucl. Chem., Letters, 201 (1995) 5, 409-416.
17. Goryachenkova T.A., Pavlotskaja F.I., Myasoedov B.F.// J.Radioanal. and Nucl. Chemistry, 147 (1991) 1, 153-157.
18. Druteikienė R, Lukšienė B., Holm E.// J.Radioanal. and Nucl. Chemistry, 242 (1999) 3, 731-737
19. Willkins B.T., Dodd N.J., Green N., Major R.O. and Stewart S.P.// In.Proc. CEC Symp. on the Behaviour of radionuclides in Estauries, Renesse, Netherlands. CEC, Luxemburg, . (1984) p.55-70.
20. Testa C., Desideri D., Guerra F., Meli M.A., Roselli C. // Czechoslovak Journal of Physics, 49 (1999) Suppl. S1, P2, 649-656.
21. Livens F.R. and Baxter M.S. // J.Environ. Radioactivity 7 (1988) 75-86.
22. Schrebetkovskij N., Bočkov A.A // Radiochimija, 6 (1975) 952-956 (in Russian).
23. Kochan I.G., Shuktomova N.A. // J.Radioanal. Nucl. Chem., Letters, 201 (1995) 5, 371-379.

RADIOTOXICITY OF NUCLEAR FUEL

Gediminas ADLYS*

* Department of Physics, Kaunas University of Technology, Kaunas, Lithuania

Abstract: Spent nuclear fuel is the biggest contributor to the radioactivity of the nuclear waste in nuclear energy sector. The main elements found in spent nuclear fuel are fission products, long-lived actinides (uranium U, plutonium Pu) and minor actinides (neptunium Np, americium Am, curium Cm). These highly active radionuclides emit alpha, beta, gamma and neutron radiation and pose the biggest risk for the environment. A measure of the hazard of nuclear material is provided by its radiotoxicity. Analysis of a radiotoxicity of the spent fuel from RBMK-1500 type reactor is provided in this article.

Keywords: nuclear fuel, fission products, actinides, minor actinides, code PEPIN1, radiotoxicity, code APOLLO1.

1. Introduction

About one third (32 %) of all the electricity produced in the European Union is nuclear-generated. Nuclear energy contributes substantially to the electricity generation in the Baltic Sea region. In 2005 nuclear power generated 70 % of the country's electricity in Lithuania, 26 % in Germany, 46 % in Sweden, 33 % in Finland. Nuclear energy is less vulnerable to fuel price changes than coal or gas-fired generation, as uranium represents a limited part of the total cost of generating nuclear electricity. The most part of enriched uranium for EU is produced in European Union countries. Perceptions about safety of nuclear power plants, management of radioactive waste, security, proliferation and terrorism have all had an influence on public opinion. However, radioactive waste management remains people's main concern regarding the use of nuclear power. A majority of EU citizens would be in favour of nuclear power if the waste issue is solved [1]. Nuclear energy is based on nuclear fission of uranium and plutonium. Binary fission, which is most probable, creates two nuclei with different masses. There are hundreds of fission products in the irradiated nuclear fuel with mass numbers ranging from 60 to 170. Mass distribution of fission products is characterized by an asymmetric curve, which represents two maxima and valley between separate groups. Most of these fission products are initially unstable and short-lived and decay within a few hours by beta, gamma or neutron radiation into radioactive daughter nuclides or to stable elements. Some nuclides in the decay chain are characterized by a radioactive decay period that can cover several thousand, or even several hundred thousand years.

As a result of neutron captures on actinide nuclei transuranic elements are produced in a nuclear reactor fuel.

The harmful potential of a certain quantity of radioactive material is assessed by considering it in terms of the dose that would be received by all the members of a group of people following the intake of a given amount of an element. The concept of radiotoxic inventory and the term of potential radiotoxicity is used with this meaning. The radiotoxicity of a nuclide is determined by its effective dose coefficient $e(T)$ or DPUI (dose per unit intake), expressed in (Sv/Bq). Effective dose coefficient corresponds to the dose resulting from the intake of 1Bq of a specific radionuclide. It takes into account the metabolism of radionuclides in the organism once ingested or inhaled the energy and type of the emitted radiation as well as the effect of radiation upon the specific tissue or organ. The quantity T is the integration time in years following intake. For adults, the integration time is 50 years. For the same level of radioactivity, actinides have a greater impact than fission products.

The radiotoxicity (Sv) resulting from intake of a particular nuclide is the product of the effective dose coefficient (units Sv/Bq) and the activity (in Bq) of that nuclide:

$$\text{Radiotoxicity} = \text{Activity} \cdot e(50) \quad (1)$$

Effective dose coefficients are evaluated using models describing the movement of radionuclides through the different parts of the body. A dose factor table is regularly updated by the International Commission on

Radiological Protection (ICRP). Generally, the values assigned are several orders of magnitude greater for actinides than for fission products

Table 1. DPUI values representing ingestion by an adult (source: ICRP 72)

| | Nuclide | DPUI, (Sv/Bq) |
|------------------|---------------|-----------------------|
| Actinides | Uranium 238 | 4.5×10^{-8} |
| | Plutonium 239 | 2.5×10^{-7} |
| | Americium 241 | 2.0×10^{-7} |
| | Neptunium 237 | 1.1×10^{-7} |
| Fission products | Zirconium 93 | 1.1×10^{-9} |
| | Technecium 99 | 6.4×10^{-10} |
| | Samarium 151 | 9.8×10^{-11} |
| | Strontium 90 | 2.8×10^{-8} |
| | Iodine 131 | 2.2×10^{-8} |
| | Caesium 137 | 1.3×10^{-8} |

2. Fission products

At the zero moment of burst fission the total activity of fission products is ultimate because of decay of a number of short-lived products. Modelling results achieved with depletion code PEPIN1 shows that total activity decreases in time because short-lived nuclides decay to more long lived nuclides. The number of nuclides versus their contribution to the total activity expressed in percents is presented in Figure 1. Maximum number of radionuclides is at zero moment, but almost all radionuclides have very small contribution from 0.001 % to 0,1 % and only contribution of 15 radionuclides is higher than 1 %. Number of contributing radionuclides is decreasing with a time. So the activity of particular nuclide increases (Fig. 2.).

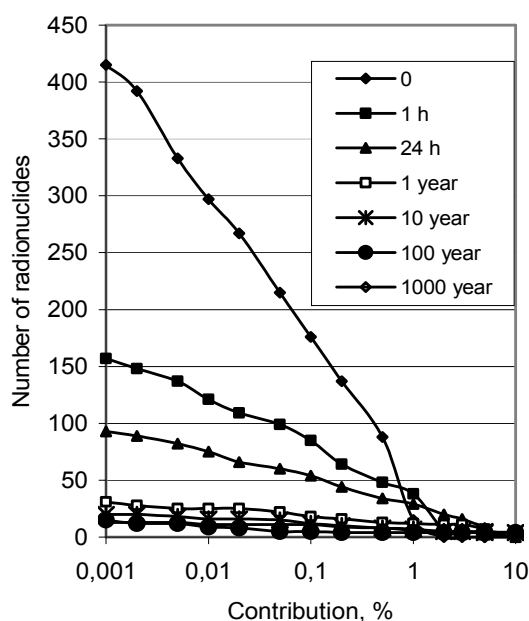


Fig 1. Number of nuclides versus their contribution to total activity

If cooling time of the spent nuclear fuel increases from 1 year to 100 years the number of radionuclides contributing to the total activity by more than 1 %

decreases from 12 to 4. At this time only 4 radionuclides contribute to the total activity by more than 10 %. After 1000 years of cooling, 6 nuclides contribute by more, than 1 %, 3 nuclides by 5 % and 1 nuclide by more than 50 % to the total activity.

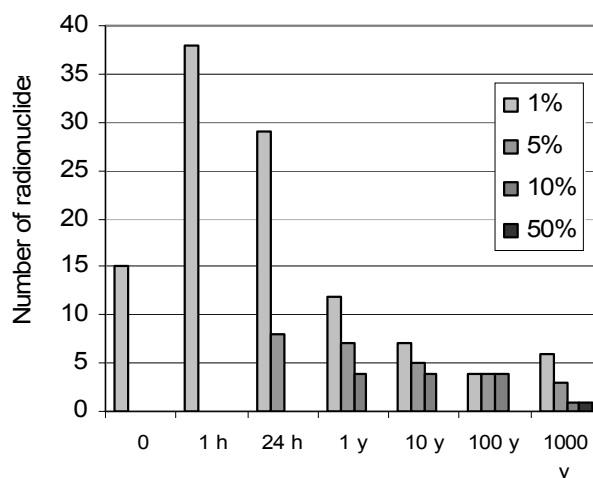


Fig 2. The number of main contributors to the total activity during the years.

In the Table 2 there are radionuclides contributing with activity of more than 0,01 % to total activity are presented in Table 2.. The results were calculated using code PEPIN1. Cursive indicates radionuclides contribution to the total activity of which is higher than 1 %, and boldfaced indicates radionuclides, contributing with more than 10 % to a total activity. After 1 year cooling the main contributors from RBMK-1500 reactor spent nuclear fuel are: ⁹⁵Nb, ¹⁰⁶Ru, ¹⁰⁶Rh, ¹⁴⁴Ce, ¹⁴⁴Pr. After 10 to 100 years of cooling ⁹⁰Sr, ⁹⁰Y, ¹³⁷Cs, ^{137m}Ba are the most important radionuclides. (Calculation was performed for the burnup of the spent nuclear fuel of 18 MWd/kg)

Table 2. Importance of radionuclides according total activity in spent nuclear fuel

| Cooling time | Nuclides |
|--------------|--|
| 1 y | Kr85, <i>Sr89, Sr90</i> Y90, Y91, Zr95, Nb95 , Ru103, Rh103m, Ru106 , Rh106 , Sn123, Te125m, Te127m, Te127, Te129m, Te129, Cs134, <i>Cs137</i> , Ba137m, Ce141, Ce144 , Pr144 , <i>Pm147</i> , Eu155. |
| 10 y | Kr85, Sr90 , Y90 , Ru106, Rh106, Sn121m, Sn121, Sb125, Te125m, Cs134, Cs137 , Ba137m , Ce144, Pr144, <i>Pm147</i> , Sm151, Eu155. |
| 50 y | Kr85, Sr90 , Y90 , Tc99, Sn121m, Sn121, Cs137 , Ba137m , <i>Sm151</i> , Eu155. |
| 100 y | Kr85, Sr90 , Y90 , Tc99, Sn121m, Sn121, Cs137 , Ba137m , <i>Sm151</i> . |

The most active nuclides are present only after some cooling time. The number of radioactive nuclides decreases with a time. The total activity and radiation power of fission products decreases with a time too

(Fig.3.). Long –lived fission products have higher impact.

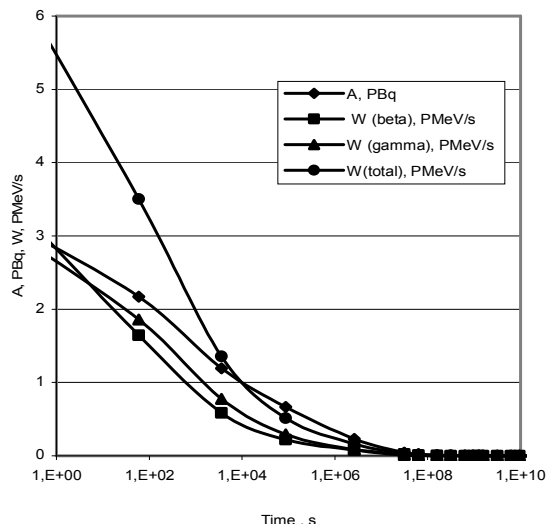


Fig 3. Activity and radiation power of fission products versus cooling time

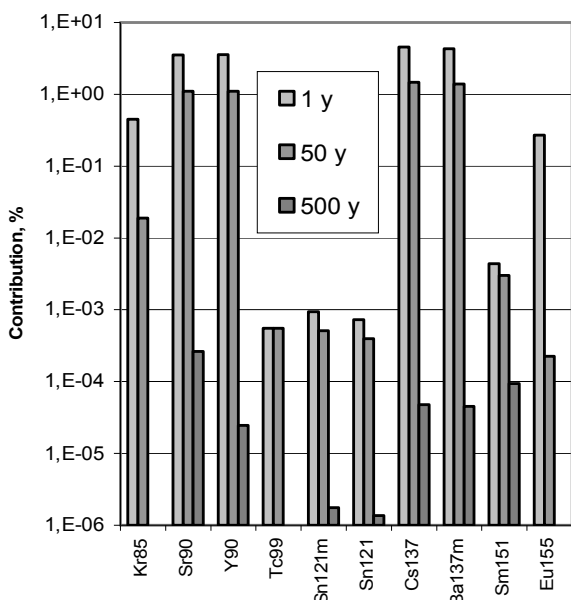


Fig. 4. Contribution of radionuclides to total activity in dependence on cooling time.

According to the Table2, after 50 years of cooling most important nuclides are ⁸⁵Kr, ⁹⁰Sr, ⁹⁰Y, ⁹⁹Tc, ^{121m}Sn, ¹²¹Sn, ¹³⁷Cs, ^{137m}Ba, ¹⁵¹Sm, ¹⁵⁵Eu, which contribution to the total activity during the time is shown in Figure 4.

After 1 min when nuclear reactor is stopped the strongest radiation power sources are ¹³⁴I (3,88 %), ¹³⁸Cs (3,58 %), ¹⁴²La (3,10 %), ¹⁴⁰La (2,84 %), ⁹⁴Y (2,37 %), ⁹³Sr (2,22 %), ⁹⁵Y (2,10 %), ¹³²I (2,07 %), ¹⁰⁴Tc (2,03 %).

After 1 hour cooling time, when most of short-lived radionuclides are decayed, contribution to radiation power of some nuclides increases: ¹⁴⁰La (7,31 %), ¹³⁴I (6,96 %), ¹⁴²La (5,76 %), ¹³²I (5,30 %), ¹³⁵I (4,40 %), ¹³⁸Cs (3,97), ⁹²Y (3,27 %).

After 24 hours the contribution of particular radionuclides to total radiation power became more

important: ¹⁴⁰La (18,63 %), ¹³²I (11,34 %), ¹⁴⁴Pr (5,97 %), ⁹⁵Zr (5,29 %), ⁹⁵Nb (5,08 %), ¹³⁵I (3,43 %).

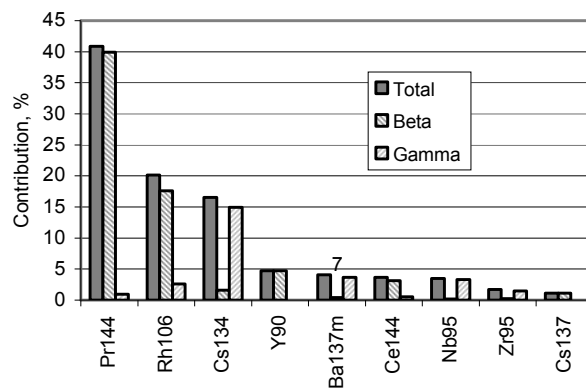


Fig. 5. Energy release from particular nuclides after 1 year

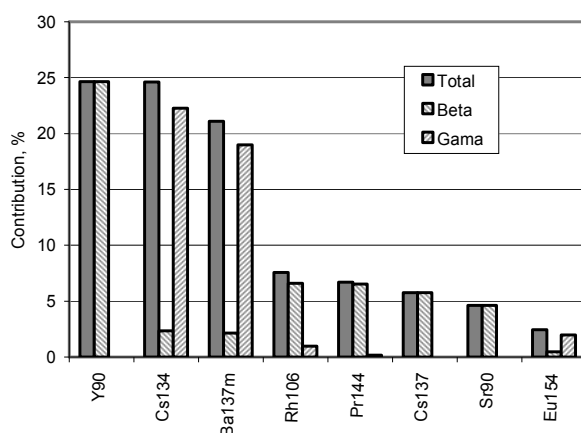


Fig. 6. Energy release from particular nuclides after 5 years

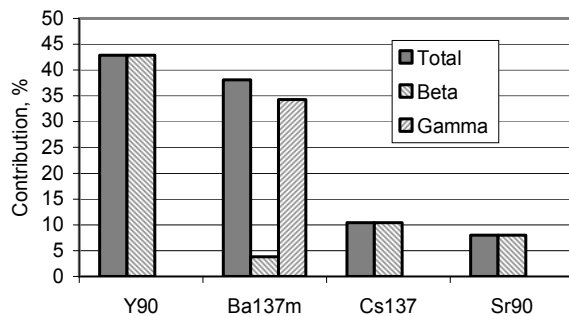


Fig. 7. Energy release from particular nuclides after 50 years

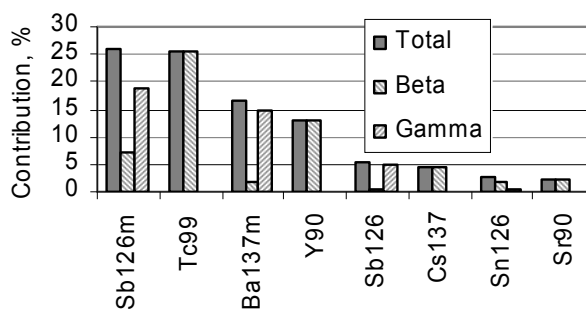


Fig. 8. Energy release from particular nuclides after 500 years

Influence of particular nuclides to energy release after 1 year, 5 years, 50 years and 500 years is shown in Fig 5- Fig.8. Total radiation power consists of beta radiation and gamma radiation

Radionuclides ^{144}Pr , ^{106}Rh , ^{90}Y thoroughly are beta radiation sources because of small gamma radiation components. At the same time ^{134}Cs , $^{137\text{m}}\text{Ba}$, ^{95}Nb , ^{95}Zr are gamma radiation sources.

Quantity of fission products depends on fuel burn-up, consequently this dependence has an influence on the contribution of particular nuclides contribution to the total energy release.

In Figure 9 comparison of radiation power is provided for the fuel burn-up of 10 MWd/kg and of 20 MWd/kg after 5 years cooling. (Nuclear fuel for RBMK-1500 reactor with 2,4 % ^{235}U + 0,41 % Er (erbium) was used for the calculations. Water density in fuel assembly was 50 %).

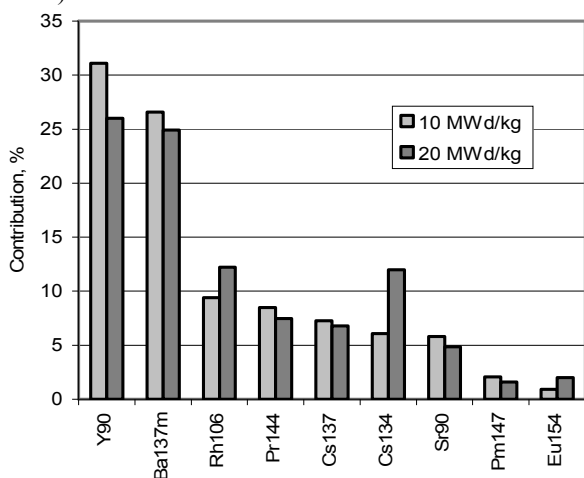


Fig. 9. Contribution to total radiation power in the case of two different fuel burn-up after 5 years cooling

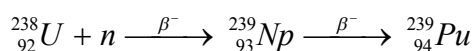
If fuel burn-up increases from 10 MWd/kg to 20 MWd/kg, contribution of ^{90}Y and $^{137\text{m}}\text{Ba}$ to the total radiation power decreases, but contribution of ^{106}Rh and ^{134}Cs increases. Comparison of these results to those calculated for 50 years cooling shows that ^{106}Rh , ^{144}Pr , ^{134}Cs , ^{147}Pm losses influence and ^{85}Kr and ^{151}Sm begin to play the main role.

Almost all fission products belong to decay chains and genetic pairs of short-lived nuclides and long-lived nuclides are formed: ^{90}Sr (28,78 y) and ^{90}Y (58,51 d); ^{106}Ru (373,59d) and ^{106}Rh (29,80 s); ^{137}Cs (30,07 y) or $^{137\text{m}}\text{Ba}$ (2,552 min).

3. Actinides

The radioactivity of spent fuel is several orders of magnitude higher than that of the uranium ore used to manufacture the fuel.

Neutron capture in ^{238}U during reactor operation is followed by two successive β^- decays from ^{239}U to ^{239}Np and to ^{239}Pu .



It is the main formation path of ^{239}Pu .

Through consecutive neutron capture on ^{239}Pu plutonium isotopes ^{240}Pu , ^{241}Pu , ^{242}Pu are produced.

Americium appears in the system through beta decay of ^{241}Pu and through neutron capture on ^{242}Pu . By neutron capture of americium curium is produced. Accumulation graphs of plutonium isotopes and minor actinides (americium and curium) are presented in Fig.10 and Fig.11. Results were calculated by means of code APOLLO1 for RBMK-1500 reactor.

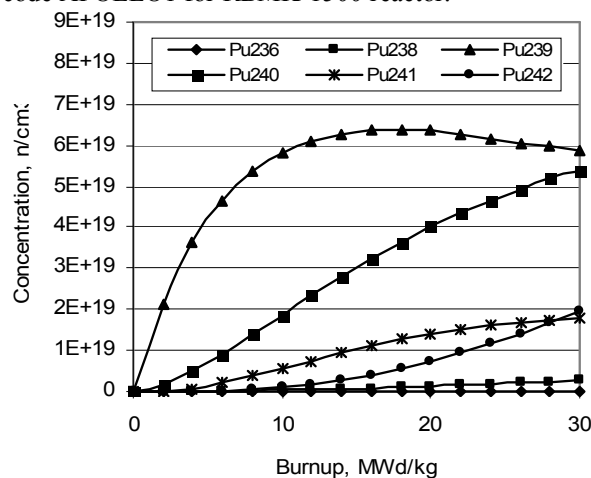


Fig. 10. Accumulation of plutonium isotopes versus fuel burnup.

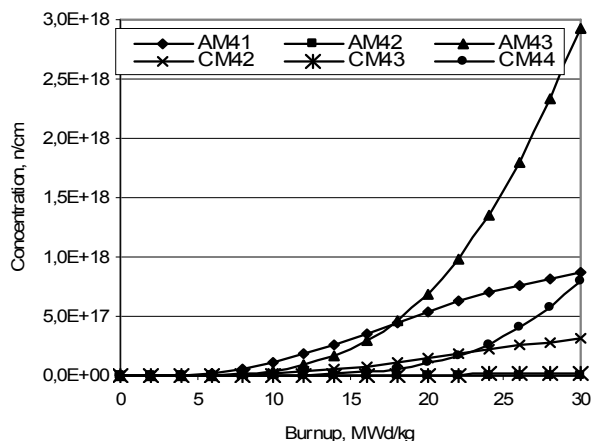


Fig. 11. Accumulation of minor actinides versus fuel burnup.

4. Summary

The values of effective dose coefficients are several orders of magnitude greater for actinides than for fission products. Plutonium and americium nuclides are dominant for the long term radiotoxicity. They remain dominant until their activities reach the level of the mined uranium in the air.

5. References

1. G.A. Adlys, D. Adlienė, S. Tulonen, Tendencies of nuclear energy development in Europe. ECT2008, Kaunas.
2. J. Magill, V. Berthou, D. Haas, J. Galy et all. Impact limits of partition and transmutation scenarios on the radiotoxicity of actinides in radioactive waste. Nuclear energy, 2003, 42, No 5, Oct., 263-277.

OPTIMISING PET/CT AND SPECT/CT INVESTIGATIONS. THE MADEIRA PROJECT.

Helena UUSIJÄRVI*, Marie SYDOFF*, Marcus SÖDERBERG*, Sigrid LEIDE-SVEGBORN*, Sören MATTSSON*
*Medical Radiation Physics, Lund University, Malmö University Hospital, SE-205 02 Malmö, Sweden

Abstract: The aim of the MADEIRA project is to improve the 3D nuclear medicine images: PET/CT and SPECT/CT. In Malmö the focus will be to study the biokinetics of radiopharmaceuticals not being published before, optimise the time between the injection of activity and the data acquisition, investigate the activity quantification in PET images, find the optimal number of subsets and iterations in iterative reconstruction of SPECT images and study the improvement of image quality of respiratory gated PET images.

Keywords: PET/CT, SPECT/CT, biokinetics, activity quantification, time optimisation, iterative reconstruction, respiratory gating

1. Introduction

Nuclear medicine images have been used to illustrate the function of organs since the 1960's. The technique has been developed from scanning over the body with a scintillation detector, via the pinhole camera to the today used gamma cameras and PET (positron emission tomography) cameras. Also the ordinary gamma cameras can be used for tomographic imaging (single photon emission tomography, SPECT) if rotating the camera heads around the patient. In recent years the SPECT and PET cameras have been integrated with a computer tomograph (CT) which is essential for the correct anatomical localisation of the activity uptake. It can also be used for attenuation maps for the attenuation correction.

The MADEIRA project (Minimizing Activity and Dose with Enhanced Image quality by Radiopharmaceutical Administrations) is sponsored by the European Union during a three year period, 2008-2010. The aim of the project is to improve the 3D nuclear medicine imaging technologies. Achievements will be made in terms of increase of spatial and temporal resolution and reduction of the radiation exposure of the patient. In consequence, the applied techniques will offer better and more detailed images for diagnosis obtained with less exposure to radiation. Better image quality may lead to earlier diagnosis that reduces mortality and improves the quality of life for the patients.

The MADEIRA project consist of four work packages: 1) assessment of clinical data, coordinated by Lund University in Sweden; 2) PET magnifier probe development, coordinated by Jozef Stefan Institute in

Ljubljana, Slovenia, together with CSIC-IFIC in Valencia, Spain and University of Michigan in Ann Arbor, USA; 3) physics-based image processing, coordinated by Helmholtz Zentrum München in Germany together with SCIVIC in Göttingen, Germany and; 4) biokinetic and dosimetric modelling, coordinated by the University of Milan, Italy. All groups are to larger or smaller extent active in most work packages.

In Malmö the main focus of this project is to 1) study the biokinetics of ^{18}F -methylcholine and ^{123}I -ioflupane, 2) find the optimal time scheme for imaging with ^{18}F -methylcholine and ^{123}I -ioflupane, 3) make phantom measurements to study whether the amount of activity in a region of interest (ROI) given by the PET/CT camera is consistent with the known activity in the phantom, 4) Optimise the reconstruction process and compare the performance of different reconstruction algorithms of SPECT images and 5) study the use of respiratory gating for imaging of tumours in the lung region with ^{18}F -FDG.

2. Ongoing studies

2.1. Biokinetic studies

To find the optimal time window for imaging and for patient dose estimations it is important to know the biokinetic of a given radiopharmaceutical in the structure of interest (often a tumour) and its surrounding normal tissue. ^{18}F -methylcholine is a new radiopharmaceutical for detection of prostate cancer and its metastasis. The detailed biokinetics for this substance has not been published and is to our knowledge not

known. Neither the biodistribution for the commercial radiopharmaceutical ^{123}I -ioflupane (also known as DaTSCANTM) has been published.

^{18}F -methylcholine is given to patients with suspected prostate cancer metastasis. Routinely, PET/CT acquisitions over the abdomen are performed directly after the injection of 0.4 MBq/kg. One hour after this a larger image, from the ear to the middle of the thigh, is taken. For the biokinetic study we will make a whole body PET/CT immediately after the injection. Additionally, three whole body PET acquisitions will be made 1 h post injection (p.i.), 4 h p.i. and 8 h p.i.. At these additional time points only a PET image will be taken and the CT data from the first time point will be used for attenuation correction. The patients will be put in the same position at all data collections with help of external positioning lasers.

^{123}I -ioflupane is used to evaluate Parkinson's disease. Routinely, the patient is given potassium iodide 1 h before the injection of 185 MBq ^{123}I -ioflupane. A SPECT/CT acquisition of the head is made 3 h p.i. In the biokinetic study we will make a whole body acquisition directly after the injection and additional SPECT whole body acquisitions 1 h p.i., 3 h p.i. and 24 h p.i.. The CT data from the first acquisition will be used for attenuation correction in the following SPECT images.

During both biokinetic studies the patients will be asked to collect all urine between the measurements. For the ^{18}F -methylcholine patients, the urine will be collected in samples for 0-1 h, 1-4 h and 4-8 h and for the ^{123}I -ioflupane in samples for 0-1 h, 1-3 h and 3-24 h. Blood samples will be taken in close connection to all acquisitions. The activity in the blood and urine will be measured with a gamma counter (WIZARDTM 3'', Wallac Oy, Finland) and ROIs will be drawn in the PET and SPECT images around the organs with uptake of activity. The biokinetic data will be used in a compartment model and the residence time will be calculated.

2.2. Activity quantification

PET images using ^{18}F -fluoro-deoxy-glucose (^{18}F -FDG) are, at Malmö University Hospital, used before and after treatment in cancer patients to see the effect of the therapy. Not only can the size of the tumour be evaluated, but also the activity uptake which gives a measure of the metabolic activity in the tumour. The PET camera at Malmö University Hospital (Philips Gemini TF) gives the amount of activity in a ROI, however the accuracy of the calculated activity needs to be investigated for various positions in the body and for various body sizes.

To do that, PET/CT acquisitions of phantoms with known activity will be performed. ROIs will be drawn around the volumes containing activity and the activity calculated by the camera will be compared to the known activity in the phantom.

2.3. Time optimisation

The optimal time between the injection and the acquisition will be investigated by measuring the patients at different times after administration of the activity. Patients injected with ^{18}F -methylcholine will be measured immediately after injection and 1 h p.i. as routinely done in the clinic. Additionally the patients will be measured 2 h p.i.. Patients injected with ^{123}I -ioflupane will be measured immediately after injection, 1 h p.i., 3 h p.i. and 24 h p.i.. For the time optimisation, whole body images are not necessary and therefore only images over the region of interest will be taken. A CT will be made at the first acquisition and this will be used for attenuation correction for the following images as well.

2.4. Optimise the reconstruction process

Originally the SPECT and PET data was reconstructed to images using filtered back projection (FBP) reconstruction algorithms. FBP is fast, but the reconstruction process induces streak (star) artefacts and the correction, by use of low-pass filters, degrades the spatial resolution. Another way of reconstructing images is to use iterative reconstruction (IR) algorithms. The primary advantage of the iterative methods over conventional FBP is the possibility to accurately model image-degrading effects, for example, attenuation and scatter, into the reconstruction model. Since the 1990's IR algorithms have been developed by the use of subgroups, e.g. the Ordered Subset Expectation Maximization (OSEM) and Flash 3D. We will reconstruct SPECT images using different numbers of subsets and iterations for the OSEM and Flash 3D algorithms as well as for a new algorithm developed by the MADEIRA project member SCIVIC and compare them with the images reconstructed using FBP.

It is known that IR gives better image quality than FBP, but it is not known how many subgroups and iterations that is optimal to use. Larger number of iterations will improve the image quality to a certain extent, before the noise takes over hand.

2.5. Respiratory gating

To get enough statistics in the images the PET acquisition takes several minutes and therefore the patient can not be asked to hold their breath during the acquisition. Tumours in the lung region may therefore appear blurred in images due to the movement of the tumour during the acquisition. This artefact can be corrected for by using respiratory gating which means that the collection of counts is restricted to a small part of the respiratory cycle.

Patients being examined for tumours in the lung region with ^{18}F -FDG will first have a clinical routine examination and thereafter have a respiratory gated examination over the lung region. An elastic band (bellows) will be put around the abdomen of the patient and the respiratory cycle will be recorded. Both the CT and the PET acquisitions will be controlled and will only be measuring at a pre-chosen part of the respiratory cycle, preferably during exhalation.

The gated and non-gated images will be compared with respect to image quality. Images from gated PET and

CT images will then be used for dose planning of radiotherapy in which the accelerator will be gated in the same way as the PET and CT equipment.

PET/CT and SPECT/CT investigations without increasing the activity given to the patient, will be performed at Malmö University Hospital. By next year we hope to present the results of the studies.

3. Summary

Several projects, all with the aim to improve the image quality and increase the information obtained by

**PLANNING AND DESIGNING A PET-CENTRE FOR CLINICAL USE.
PRELIMINARY EXPERIENCES FROM UMEÅ, SWEDEN**

Lennart JOHANSSON*

* Radiation Physics Department, Umeå University Hospital, SE-905 81 Umeå, Sweden

Umeå University Hospital in Sweden is a hospital serving the northern half of Sweden with highly specialized medical service. At present we are running a project with the purpose of establishing a clinical PET-centre including cyclotron and equipment for local production of PET-radiopharmaceuticals. We have chosen to invest in our own cyclotron and radionuclide production, of two reasons: - we are a university hospital and as such interested in keeping up with the development, and being able to use also more short-lived positron emitters as tracers. - we are located far away from other cyclotrons, which mean that we will be confined to expensive air transports, if we want to buy the tracers. In Umeå the cyclotron, bunker and chemistry department, and the PET-camera will be placed in a new building, together with the departments for radiation treatment and conventional nuclear medicine.

Ten years ago PET was an expensive and exclusive method for radiodiagnosis, mainly in neurology, and for pharmacological research. The reason for this was the need for large and expensive cyclotrons, and a staff of well qualified radiochemists for the production of the labelled substance, usually with ^{11}C ($T_{1/2} = 20$ min). During the last years, however, PET investigation for diagnosis, treatment planning and follow up in oncology has received an increased importance, and it is approaching a "golden standard" for some type of tumours. The number of small or intermediate PET centres has thus increased dramatically. This increase is due to the recent technical development, including increased availability of the glucose analogue ^{18}F - FDG. Fluorine-18 has a half-life of 109 minutes, and on the contrary to e.g. ^{11}C -labelled substances with this radionuclide, can be transported for some hours before use. A second reason is the introduction of the hybrid PET/CT camera, with fused CT- and PET- images, that increases the diagnostic value.

Today ^{18}F FDG and also ^{18}F as fluoride is commercially available. One delivery of about 10 GBq ^{18}F FDG is enough for 10 patients, administered and investigated

two patients per hour, with one hour waiting for the substance to be taken up. In the future possibly a further number of ^{18}F - labelled substances will be found on the market. On the other hand, the possibility that some of the substances that today only can be labelled with ^{11}C , in the near future will be commercially available labelled with ^{18}F , should not be ruled out. However, in order to use ^{11}C labelled substances, such as methionine, or acetate, a cyclotron will be needed. It may be necessary to invest in a cyclotron also if the distance to the nearest production facility is too far, leading to either too high costs if transported by air, or too long delivery times, if transported by car.

When planning a PET facility it is recommendable to place the PET-scanner as close to the cyclotron and hot-lab as possible, in order to minimise transport routes. Furthermore, in order to enable a future possibility to use ^{15}O ($T_{1/2} = 2$ min), e.g. for cardiac studies, requires a radionuclide transportation tube between the cyclotron and the scanner room. If the PET/CT is to be used for planning radiation treatment it is an obvious advantage to place the scanner not too far away from the treatment department.

Cyclotron

The development and introduction on the market of small cyclotrons is a major reason for the increase in number of clinical PET-investigations. One important feature, of these cyclotrons is that they accelerate negative hydrogen ions instead of protons. Stripping off the electrons from the ion reverses the electrical charge, and hence the direction of the rotation. The strong and bulky magnets that were necessary in order to bend the proton beam to the target for older cyclotrons could thus be replaced.

Small cyclotrons for radionuclide production that deliver proton energies up to about 18 MeV are now commercially available. Some of them can also accelerate deuterons. This will be enough energy for production of most radionuclides that is used for PET

Table 1. Production of positron emitters

| Radionuclide | Half-life | Nuclear reaction | Threshold (MeV) | Energy for cross section maximum (MeV) | Chemical form |
|------------------|-----------|--------------------------------------|-----------------|--|------------------------------|
| ^{18}F | 110 min | $^{18}\text{O}(\text{p},\text{n})$ | 2.6 | 5.2 | F^- |
| ^{18}F | | $^{20}\text{Ne}(\text{d},\alpha)$ | 0 | 12.3 | |
| ^{11}C | 20.4 min | $^{14}\text{N}(\text{p},\alpha)$ | 3.1 | 7.6 | CO_2 |
| ^{11}C | | $^{10}\text{B}(\text{d},\text{n})$ | 0 | 9.0 | |
| ^{15}O | 2.07 min | $^{14}\text{N}(\text{d},\text{n})$ | 0 | 4.0 | O_2 |
| ^{15}O | | $^{15}\text{N}(\text{p},\text{n})$ | 3.7 | 6.6 | O_2 |
| ^{13}N | 9.96 min | $^{16}\text{O}(\text{p},\alpha)$ | 5.5 | 8.0 | NH_4^+ |
| ^{124}I | 4. 18 d | $^{124}\text{Te}(\text{p},\text{n})$ | | 12 | |
| ^{64}Ni | 12.7 h | $^{64}\text{Ni}(\text{p},\text{n})$ | | 11 | |
| ^{86}Y | 14.7 h | $^{86}\text{Sr}(\text{p},\text{n})$ | | 13 | |
| ^{68}Ge | 271 d | $^{69}\text{Ga}(\text{p},2\text{n})$ | | 20 | $\rightarrow ^{68}\text{Ga}$ |

(Table 1). The energy of the cyclotron should at least exceed the energy for the cross section maximum.

When choosing a proper cyclotron one should consider what radionuclides you will need to produce, and what activity will be needed. With one PET-scanner the a cyclotron producing a proton beam of around 10 MeV will normally be enough to supply the department with enough amount of ^{18}F or ^{11}C .

If the radionuclide produced will be limited, to ^{18}F , ^{11}C and ^{15}O , possibly also ^{14}N , there is no need for solid targets, and also no need to leave space for a beam-line. Possible positron emitting radionuclides that may be of interest in the future, such as ^{64}Cu or ^{124}I . The production of those, and other infrequently used radionuclide requires different types of solid targets, and is therefore rather expensive.

Chemistry synthesis modules

A production site for PET-radiopharmaceuticals also requires equipment for the labelling of carrier molecule with the radionuclide. Also in this field the recent development has resulted in simple devices for automatic synthesizing some of the most common ^{18}F and ^{11}C labelled substances. This is another invention that have contributed to the recent dramatic increase in number of PET centres, since this facilitated the laboratory work considerably.

A configuration which may be considered as suitable for a centre mainly producing PET-radiopharmaceuticals for in-house use is to have one synthesise module fixed for e.g. ^{18}F FDG production and perhaps one more common ^{18}F labelled substance, and a complementary module that can be programmed, for production of different ^{11}C labelled substances. In this context it is important to point out that the synthesise equipment, and also all chemicals used has to follow the GMP-rules.

PET/CT scanner

Almost all PET-scanners sold today are equipped also with a CT. The CT is used for attenuation correction of the PET-images, and for diagnostics. Also a combined PET and MR camera has recently been announced, but

this combination still has to prove its abilities. Parameters, which, some of them may affect the image quality, that are of interest to consider when choosing a PET/CT camera are:

- *Detectors.* Today various scintillators are used, bismuth germanate (BGO) and lutetium oxyorthosilicate (LSO) are two common types, but also LSO doped with yttrium (LYSO) and gadolinium oxyorthosilicate (GSO), are found on the market. Since all of these detectors have favourable properties, such as high atomic number and light yield, the performance of the scanner depends to a high degree on the scanner design as a whole such as configuration of the detectors, and detector rings, electronics, and the encoding of the position of the scintillation in a scintillator block.
- *Field length.* The field length, or the axial field of view, varies between different scanners, a larger field length decreases the scan time, since the, number of positions per scan is decreased. A larger field length, however, also means a larger number of detector rings, and hence a more expensive camera. Typically one need acquire pulses for about 5 minutes per field of view, and
- *Diameter of tunnel.* The diameter of the tunnel, or the transaxial field of view, does not only set a limit on the size of the investigated patient, a larger diameter is also desirable also for scanning patients with the purpose of dose planning for external radiotherapy. In those cases the patient should be scanned fixed in the same position, and on the same type of table that will be used during the irradiation.
- *3D and/or 2D acquisition.* Most modern PET scanners today have uses regularly 3D scanning. 3D scanning means that coincidences are considered not only between detectors in the same ring, but also between different rings. In 2D model lead shields are introduced between the different rings preventing photons from the same annihilation to be detected by detectors belonging to different rings. The sensitivity of the system is thus limited, but the number of random coincidences that has to be handled by the electronics is also decreased.
- *Time of flight.* When fast enough scintillation material and electronics are used it is possible to use a time window for the coincidence that is less than 1 ns. This enables a possibility to better locate the scintillation; since it may be indicated from which radial

distance within the ring it has its origin. This will improve the image slightly, especially the contrast and signal to noise ratio.

- *Motion correction, breath gating.* Since the PET-scanning will take about 5 minutes per axial field of views, the patient will not be able to hold the breath during this time. Compared to the CT of the same area, which is almost instantaneously, this may lead to mismatches, especially over the thorax-region. This mismatch might affect the SUV-value and lead to artefacts from the attenuation correction, a gated collection, in list model, or live, may prevent this. The image improvement achieved with this technique, is significant, and this may be considered as more important than e.g. time of flight.
- *Type of CT.* Which CT to choose will affect the price as well as the total scan time for the patient and hence the throughput capacity.
- *Laser positioning.* If the PET/CT images are going to be used for radiation treatment planning a laser beam system for the position of the patient on the table is needed.

Radiation protection

The penetrating ability of the 511 keV annihilation photons is considerably larger than that of all other radionuclides used in nuclear medicine. Also the number of photons is twice as high as compared with most other radiopharmaceuticals. It is therefore important that the premises and the working flow should therefore be carefully planned with regard to radiation protection of the staff, which will be exposed from syringes and patients to a larger extent than in conventional nuclear medicine. It is important to have shielded injection rooms and, where the patient also can wait after injection. Preferably these are planned as separate room. Three such rooms will be needed for full day scanning with FDG patients with one camera. Depending on the radiation levels accepted outside the room, 10 – 30 mm lead is needed.

The use of accelerators is subjected to radiation protection rules and restriction. The cyclotron has to be placed in a bunker, with 2 m thick walls of ordinary concrete. The cyclotron vault may be entered either via a slide door of the same thickness, or a maze, the latter will take up more space. Mini-cyclotrons are available as self-shielded. Even if such a shield minimizes the space required for the installation, it will not completely eliminate the need of a bunker, about 50 cm concrete walls, should however be enough. When beam is on a complex radiation field of, neutrons, bremsstrahlung, and prompt or delayed gamma and β^\pm rays is created in the vault. The beam itself, as well as the neutrons, and high energy photons, will produce a large number of different radionuclides by activation. The highest activity is composed of rather short-lived radionuclides, of which some of them are gases or aerosols that should be ventilated out. Fortunately the most active radionuclides are comparatively short-lived, it is therefore recommendable to wait for some specific time, before entering the vault after irradiation. The best way

is to monitor the radiation inside, and set up a dose-rate limit that not should be exceeded when entering. Also neutron monitoring in the vault is advisable.

Airborne radioactivity produced within the cyclotron, and the target area, should not be directly ventilated out in the vault, it may be stored to decay in a long tube, either buried under the concrete floor, or in a special container. It should also be noted that it in some European countries is necessary the measure the activity that is let out in the open air, through the chimney, and report this to the authorities. This requires monitoring of activity air concentrations as well as the air-flow.

The neutrons may be a special problem, since they may cause activation products to be produced in the wall of the bunker. As time passes this may result in small activities of comparatively long-lived radionuclides. One way to gain control over this is to mix some barium, e.g. in the form of barite, in the concrete, or use barium rich painting on the walls, which catches the neutrons. Since iron isotopes may be activated it is important not to use iron or iron ore in the walls of the cyclotron vault, normal reinforcement bars in the concrete, should, however, not cause any problem.

The synthesis equipment has to be placed in shielded and well ventilated cells or hot-boxes designed for this purpose. All further manipulation of the radioactive solution should also be carried out behind at least 5 cm lead. For FDG the finally prepared substance may be delivered in a vial with 10 – 50 GBq ^{18}F . From a radiation protection point of view an automatic dispenser is preferable delivering injection ready and labelled syringes placed in a syringe shield, preferably of tungsten.

Quality assurance

Production of radiopharmaceuticals for use in humans should always follow the GMP-regulations (Good Manufacturing Practice, volume 4, European Union). Those rules are important when designing the facilities for the laboratory. The configuration of the laboratories for the radionuclide production should be designed with sluices, separate for persons and material, and also separated for material in and out. The quality control of the prepared substance can not be performed in the same room as where the hot-boxes are located.

Before administering the substance prepared the quality of the produced batch has to be controlled. The quality control laboratory should be a separate room near the hot-lab. The most important equipment for quality control is an HPLC.

Gallium-68 generator

The ^{68}Ga generator is increasingly popular, and ^{68}Ga is probably the third most common positron emitter after ^{18}F and ^{11}C . Gallium-68 is produced as a daughter when ^{68}Ge decays. Gallium may be used for tumour diagnostics, and it is a cheap alternative to a cyclotron.

Referances

- Bailey DL., Townsend DW., Valk PE, Maisey MN. Positron Emission Tomography – Basic sciences. Springer 2005
- Calandrino R., del Vecchio A., Todde S. and Fazio F.: Measurement and control of the air contamination generated in a medical cyclotron facility for PET radiopharmaceuticals. Health Phys. 92(2007)S70-S77
- Guillet B., Quentin P., Waultier S. *et al.*: Technologist radiation exposure in routine clinical practice with 18F-FDG PET. J Nucl Med Technol. 33(2005)175-179
- Haddad F., Ferrer L., Guertin A. *et al.*: ARRONAX, a high-energy and high-intensity cyclotron for nuclear medicine. Eur J Nucl Med Mol Imag 35 (2008) 1377-1387
- Hertell N.E., Shannon M.P., Wang Z.-L. *et al.*: Neutron measurements in the vicinity of a self-shielded pet cyclotron. Radiat Prot Dosim 108(2004)255-261
- Kemp BJ., Kim C., William JJ *et al.*: NEMA NU 2-2001 performance measurements of LYSO-Based PET/CT system in 2D and 3D acquisition mode. J Nucl Med 47(2006)1960-1967
- Madsen MT, Anderson JA, Halama JR, *et al.*: AAPM Task Group 108: PET and PET/CT shielding requirements. Med Phys. 33(2006)4-15.
- Mah D. and Chen CC. Image Guidance in Radiation Oncology Treatment Planning: The Role of Imaging Technologies on the Planning Process. Semin Nucl Med 38(2008)114-118
- Phelps ME. PET: Molecular Imaging and Its Biological Application. Springer 2004.
- Sharma S., Krause G., and EbadiRad, M.: Radiation safety and quality control in the cyclotron laboratory. Radiat. Prot. Dosim. 118(2006)431-439
- Townsend DW. Positron Emission Tomography / Computed Tomography. Semin Nucl Med 38(2008)152-166

SKANDIONKLINIKEN - THE SWEDISH CENTRE FOR PROTON THERAPY

Håkan NYSTRÖM*

* chief physicist, the Skandion clinic, Uppsala, Sweden, hakan.nystrom@skandion.se

Abstract: Proton therapy, although not an entirely new innovation, has gained a lot of new interest in recent years. The main reason for this is the new developments in proton therapy technology, including Spot Scanning and IMPT. Uppsala, Sweden was among the pioneers in proton therapy and a new centre for proton therapy is now planned there. The new facility is a joint undertaking of seven counties and their eight university hospitals in Sweden under a concept of distributed competence.

Keywords: Proton therapy, Spot scanning, distributed competence.

1. Introduction

The use of protons as a modality to treat deeply located tumors is not a new idea, but was proposed already in 1946 by Wilson [1]. The specific interaction properties of protons with a well pronounced Bragg Peak at the end of their trajectories, makes it possible to create dose distributions far more tailored to the shape of the tumor than with any other existing conventional treatment modality. The first treatments with protons were performed in Berkeley, Ca, USA in 1954 and the second facility to open was at the The Swedberg Laboratory, Uppsala, Sweden in 1957. Since then, more than 55 000 patients have been treated world wide, and around 1 000 in Uppsala. The real boom for proton therapy has, however, come in the last decade when new technology for steering the beam has made Spot Scanning and Intensity Modulated Proton Therapy (IMPT) possible. The number of proton facilities is now increasing rapidly, and a new Scandinavian facility is planned in Uppsala, Sweden.

2. New developments in Proton therapy.

The traditional way of achieving a flat field suitable for patient treatments with a proton beam, is known as Passive Scattering. With this method, several beam modifiers, such as scattering foils, energy degraders, bolus and collimators are introduced into the beam. Although effective to create homogeneous dose distributions, Passive Scattering also has some severe limitations and drawbacks. Entering material into the beam creates a background of neutrons to the beam. This neutron "dose-bath" is highly unwanted, in particular for young patients, since it increases the risk of developing radiation induced secondary malignancies

later on in life. Some neutron contribution will always be present due to interaction processes within the patient, but around 80% of the neutron contribution comes from the beam modifying devices [2]; a contribution that can be avoided.

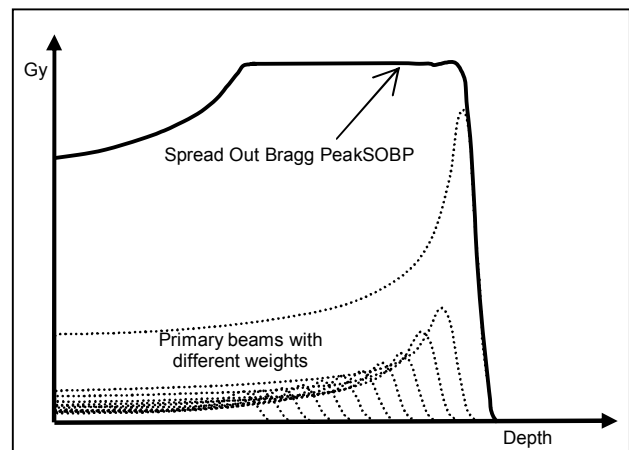


Fig. 1. A homogeneous dose distribution in the depth direction, is achieved by adding beams with different energies. The resulting dose distribution is designed to give a flat dose distribution all through the depth of the target.

The beam modifying devices used with Passive Scattering are to a large extent custom made for each patient. This requires work shop facilities, man power for device production and manual change of collimators etc. between fields. Passive scattering has also significant limitations in the possibilities of tailoring the high dose region to the shape of the target, since the depth of the spread out Bragg Peak will be the same in all parts of the field, irrespective of the depth of the

target. Last but not least, Passive Scattering is designed to obtain homogeneous dose distributions and cannot provide IMPT.

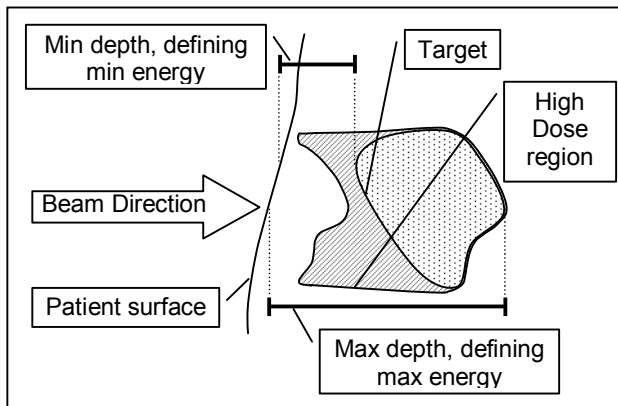


Fig. 2. With Passive Scattering, the depth of the Spread Out Bragg Peak (SOBP) will be the same in all parts of the field, making the high dose region too large.

Passive Scattering is still the most common method used for patient treatments, but new technology is emerging, without the limitations that are inherent in Passive Scattering.

With Spot Scanning, sometimes referred to as Active Volume Scanning, the pristine pencil beam from the accelerator is deflected electromagnetically to hit a predefined point within the patient. If the pencil beam can be made sharp enough, there will be no need for mechanical collimation. By scanning the beam over the patient in both x- and y-direction, there will be no need for scattering foils to achieve broad fields.

Energy modulation, in order to create a Spread Out Bragg Peak (SOBP), does not need to be as fast as in Passive Scattering, but can be done step wise, energy layer by energy layer. In this way the energy modulation can take place before the gantry, outside the treatment room. These things together practically eradicate the unwanted neutron dose reaching the patient from the equipment. Left is the unavoidable contribution of neutrons created by the proton beam inside the patient, but this contribution is minor compared to what Passive Scattering would have brought [2].

The SOBP can be tailored individually for any ray line of the beam. In different parts of the field, the maximum and minimum depth of the target, and hence the desired length of the SOBP, varies significantly, and this can be accurately taken into account in the planning process with no unnecessary energy deposition in volumes upstream the target.

In the planning process, any sub-volume of the target can be assigned an individual spot weight, which opens up for dose optimization in a similar way as IMRT in conventional radiotherapy. Two or more fields can be summed together, where each field can be optimized to avoid critical structures. The cost is an inhomogeneous dose distribution in the target, but when summed together with the other fields, the result is a homogeneous dose distribution in the target, as well as a minimized dose to surrounding tissue [3].

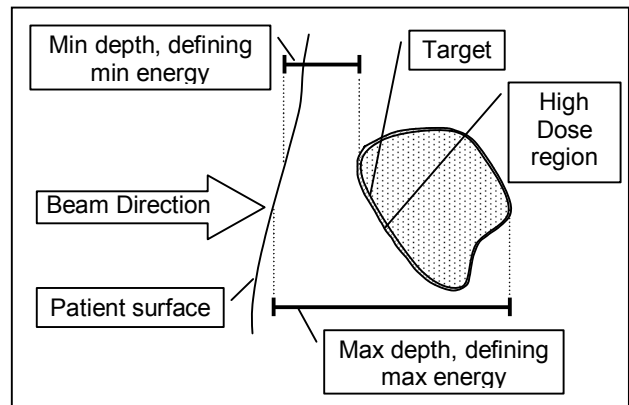


Fig. 3. With Spot Scanning, the high dose region can be properly tailored to the target volume.

Spot Scanning, and IMPT in particular, demand fast and accurate magnet systems in the beam transport, as well as powerful and safe software for dose calculation and optimization. To bring Spot Scanning from theory to clinical practice has therefore not been an entirely easy task.

The first to introduce the technique in a clinical setting was Paul Scherrer Institute (PSI) in Switzerland, who started more than 10 years ago with patient treatments in a scanning beam [4] and most of the development in this field has been performed there. The main vendors in the proton business are developing systems for spot scanning, and in the near future several clinics will take this new technology into clinical use.

3. The Swedish Concept of Distributed Competence

Proton therapy is sometimes accused to be an extremely expensive form of cancer care. Before making such a statement, however, we must not forget that radiotherapy is a very cost-effective way of treating cancer. Radiotherapy is, next to surgery, the most important modality in the fight against cancer. Chemotherapy, however increasingly important, is far less effective and far more costly. True is, however, that proton therapy is more expensive than conventional radiotherapy, and in particular the investment costs are significant. In order to justify such a large investment, there must be patients enough that would significantly benefit from proton therapy, rather than conventional therapy. Several investigations around Europe estimate the fraction of such patients to around 10 – 15% of all radiotherapy patients. This means that a typical mid-size to large clinic with the order of 1 – 3 000 new patients per year would not have enough own patients to justify the kind of investments necessary for a proton facility. To overcome this problem, all the eight university hospitals in Sweden¹, located in seven different counties, came together with a cooperation plan to

¹ Norrlands universitetssjukhus, Umeå, Sahlgrenska universitetssjukhuset, Göteborg, Karolinska universitetssjukhuset, Stockholm, Universitetssjukhuset MAS, Malmö, Universitetssjukhuset i Lund, Hälsouniversitetet, Linköping, Universitetssjukhuset Örebro, Akademiska universitetssjukhuset, Uppsala

establish a proton facility, common for all university hospitals.

The first hurdle to overcome was the structure of the health care system in Sweden. The country is divided in 20 counties, each having the health care responsibility of its own area. To be able to finance and run a common project of this order, the seven counties with university hospitals formed a joint authority of county councils; a legal body at the same level as the counties, but with the sole mission to create and run the proton facility. This was the first time in Sweden where a national joint effort has been established to provide highly specialized health care.

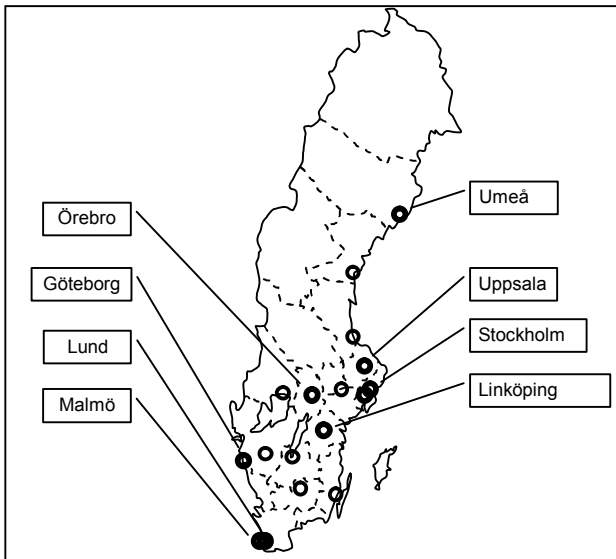


Fig. 4. Co-operating radiotherapy centres indicated with bold circles and name

The location of the facility was decided to be Uppsala, due to its central location in the country, with good access to the largest airport of Sweden, but also due to its know-how and expertise of proton therapy at the The Svedberg Laboratory. Further, it was possible to find a location close to the university hospital of Uppsala, enabling a close co-operation in areas like pediatric and anaesthetic care.

Close co-operation will be a key issue, not only to make sure that all patients who would benefit from proton therapy will also get it, but also to ensure a high level of quality and expertise all over the country. To facilitate this, the operation of the Skandion clinic will be organized according to the concept of distributed competence [5]. Basically this means that the proton facility is only there to perform the actual treatment of the patient. All the planning steps taken prior to the treatment, including immobilization, CT-scanning and treatment planning, will be performed at the home clinic, as well as any follow-up after the treatment. At the Skandion clinic, highly professional staff, including radiation oncologists, nurses and medical physicists will take care of the patient and the treatment. The medical responsibility of the patient will, however, remain with the doctor at the home clinic, who will be in frequent contact with the staff at the proton facility.

One of the consequences of this is that patients cannot be referred for treatment at the Skandion clinic. Patients

coming from any of the non-university clinics, or from abroad, must be referred to one of the eight participating university clinics, constituting the Skandion clinic.

It could be argued that distributed competence might lead to diluted competence, since the expertise will be distributed over many persons. However, since patients from many different diagnose groups will be treated, the national experts for each and every group will be involved and bring their invaluable competence to the proton centre. In addition, a network for teleconferencing will be established with regular conferences, and every single patient's records and treatment plans will be discussed and presented to all participants within the network.



Fig. 5. The architect's view of the Skandion clinic.

Since proton treatments are expected to be about twice as expensive per fraction compared to conventional radiotherapy, a reimbursement system will be developed to ensure that the decisions to treat will always be taken on purely medical grounds with no financial aspects involved. To do so, a subscription system will be introduced. This means that every county will be paying half of the expected costs to run the proton facility, scaled to the relative population of each county, on a yearly basis, irrespectively of how many patients will be treated from that county. The remaining costs will be covered by a per fraction fee that is expected to be of approximately the same magnitude as for a conventional fraction.

4. Status of the Swedish Project

The project to establish a Scandinavian centre for proton therapy started a decade ago and was driven by the professions of radiation oncology and medical physics. A report was presented in 2003 where all the rationales for the project were described and an analysis of the need was performed. The report paved the way for a political consensus of forming the joint authority of county councils for advanced radiotherapy. After a pre-qualification tendering process in 2007, the real tendering process is in action in 2008, and a contract with a major supplier of proton therapy equipment, including all the necessary sub-systems, such as treatment planning systems, imaging devices and oncology information systems, is expected first half of 2009. The building construction work will start the

same year, and the first patient is expected to be treated in 2012.

The Skandion clinic is established primarily to meet the need of Swedish patients, but will, depending on free capacity, be open also for patients from abroad. Important in this respect, as mentioned above, is that patients referred to proton treatment must first be referred to one of the co-operating university hospitals.

5. References

1. Wilson R. R., Radiological use of fast protons. *Radiology* 1946. (47) p. 487-491
2. Jarlskog CZ, Paganetti H., Sensitivity of different dose scoring methods on organ-specific neutron dose calculations in proton therapy. 2008. *Phys. Med. Biol.* 53(17) p. 4523-32
3. Lomax A. J., Pedroni E., Rutz H. and Goitein G. The clinical potential of intensity modulated proton therapy. *Med. Phys.* 2004. 14(3) p. 147-52
4. Pedroni E. *et. al.* Initial experience of using an active beam delivery technique at PSI. 1999. *Strahlentherapie Oncol.* 175 suppl. 2. p. 18-20
5. Karlsson M., Björk-Eriksson T., Mattsson O. *et. al.* "Distributed proton radiation therapy" – A new concept for advanced competence support. *Acta Oncologica* 2006. 45 p. 1094-101

USE OF THE LASER BEAM FOR MARKERLESS TRACKING OF THE PATIENT BREATHING MOTION FOR RESPIRATORY GATED RADIOTHERAPY

Aleksejs KATASEVS^{**}, Sergey POPOV^{*}, Arturs MEIJERS^{*}
^{*} Latvian Oncology Centre of Riga Eastern Clinical University Hospital, Riga, Latvia
^{**} Riga Technical University, Riga, Latvia

Abstract: Respiratory gating is broadly used method in modern radiotherapy to lessen uncertainties related to patient respiratory motion. Most of the currently available commercial respiratory gating systems involve use of mechanical markers attached to the patient chest for caption of motion during CT scanning as well as radiotherapy treatment. The present paper explores the possibility to use infrared laser light reflected from the moving surface as optical markers instead of mechanical marker box for commercially available gating systems. Performed tests demonstrated, that reflected laser spot movement can be used to obtain breathing patterns, and acquired signals are suitable for respiratory gating.

Keywords: Breathing adapted radiotherapy; respiratory gating systems; infrared laser beams.

1. Introduction

Respiratory motion is a major source of treatment uncertainty for radiation therapy of tumors in the thorax and abdomen. During normal respiration, diaphragm excursions of more than 2 cm are observed under fluoroscopy and motion of 1 to 3 cm has been reported for kidneys, liver and tumors in lung. [1] To provide full dose to the CTV, the PTV must be large enough to take into account respiratory motions. However, large margins may include excessive healthy tissue in the radiation fields. With respiratory gating system, the patient's normal breathing is monitored by a device which turns on the treatment, CT or simulator beam only when respiratory motion is within a particular, previously chosen phase.

One of the respiratory gating methods, currently used at the Latvian Oncology Center of Riga Eastern Clinical Hospital, is motion capture technique developed by Varian Medical Systems [2]. The system uses infrared – reflective marker box, attached to the patient chest. Movement of the box is acquired by infrared CCD camera, thus allowing no obtain breathing movement pattern. This approach has several drawbacks: mechanical object (marker block) on the patient chest during the treatment delivery, necessity to include this object in the treatment plan, time consuming positioning of the object.

At the same time, there are number of methods, that allow obtain the form of object by scanning with the laser beam and measuring the position of the reflected

spot (see, for instance, [3]). At the Riga Technical University (RTU) this technique were modified recently to be used for motion capture of the breath movement and evaluation of the breathing pattern. The method is based on the use of laser spots instead of markers, directly attached to the surface [4]. The aim of the present work is to demonstrate, that the laser beam can be used instead of marker block (Varian) to capture breath motion in real time by means of commercially available respiratory gating system (Varian). [2]

2. Materials and methods

2.1. Respiratory Gating System

Major components of the Varian commercially available gating system includes:

- Charge-coupled device (CCD) tracking camera
- *In situ* monitor - view finder, showing the image from the camera
- PC workstation running the system software
- Gating switchbox
- Speakers for providing the patient with audible prompts
- Marker block

System tracks the vertical component of upper marker motion to reproduce the breathing pattern (during the tests - reflected laser beam). The distance between both markers is used to calibrate the system and calculate the absolute amplitude of the movement.

During the tests, two infrared (IR) laser beams, directed at breathing phantom, were used instead of marker block.

2.2. Measurements

To acquire breathing patterns, breathing phantom, developed by Varian Medical Systems, was used (Fig 1.) [2].

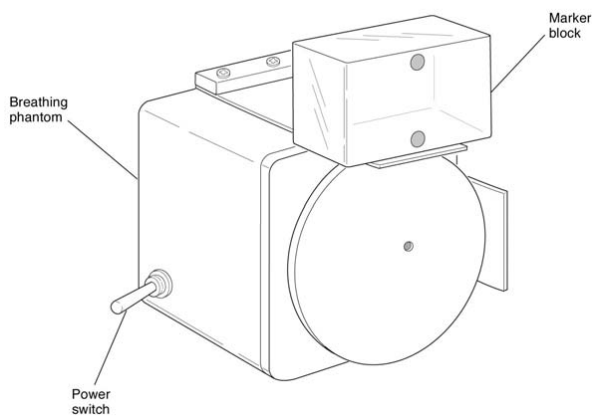


Fig. 1. Breathing phantom

To verify the actual mechanical position of the breathing phantom, corresponding to specific moment phase of the breathing pattern, gated treatment simulation at the linear accelerator Clinac 2100C/D (Varian Medical Systems, USA) was carried out. The portal image was obtained by use of Kodak X-Omat films. Films were exposed with 6MV photon beam and dose rate 300 MU/min. Irradiated films were digitized using Vidar 16 VXR (Vidar Systems Corporation, USA) film scanner with resolution 75 dpi. Films were further processed using DoseLab 4.0 software [5].

2.3. Test sessions

Several test sessions were carried out:

1. Breathing pattern was recorded by using lasers as well as marker block to compare properties of both signals.
2. Breathing patterns were recorded at different geometrical positioning of the lasers (changing beam incidence angle and distance between lasers) to verify the impact of geometrical configuration on the acquired signal amplitude.
3. Breathing patterns were acquired both at CT and linear accelerator to verify that the same phantom movement amplitude would result in the same signal amplitude at both locations, therefore allowing gating.
4. To verify that the maximal amplitude of the acquired breathing signal corresponds to the maximal mechanical position of the phantom two films were irradiated at the linear accelerator, first - with gating enabled, beam triggering thresholds set to the maximal inhale, second - with gating disabled.

3. Results and discussion

Breathing patterns acquired by using lasers and marker block are shown in figure 2.

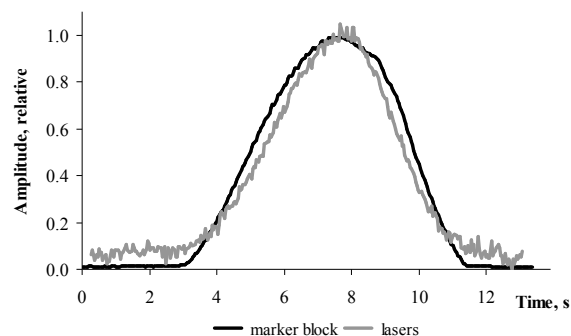


Fig. 2. Signals acquired by using lasers and marker block

Both signals are normalized to compare their properties: for lasers, measured breathing cycle was 12.0 s ($\sigma = 0.34$ s), however for the marker block it was 12.5 s ($\sigma = 0.10$ s). The discrepancy is due to discharge of the phantom battery, providing steady increase of phantom movement period.

The amplitude of the signal strongly depends on the geometrical position of the lasers and camera (Fig. 3).

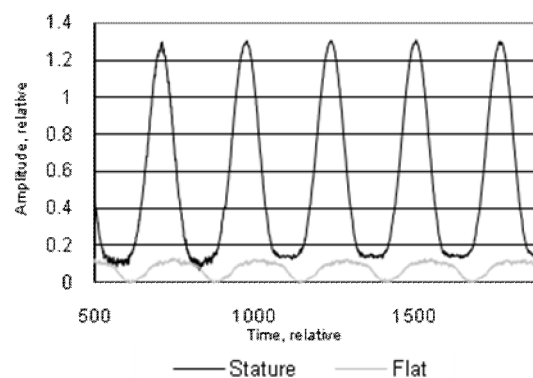


Fig. 3. Impact of the laser beam incidence angle

To obtain greater signal amplitude it is necessary to ensure greater angular difference between laser beams and optical axis of the camera. However if the lasers are positioned in a way that the beam incidence angle regarding the patient is less than one of the camera optical axis, this will result in inverted signal (Fig 4.). If the incidence angle of laser beams is the same as one the angle of camera optical axis, it is not possible to track any motion.

Varian gating system uses distance between markers to determine absolute amplitude of the motion; due to this the distance between laser beams is another factor influencing signal amplitude (Fig. 5). Breathing signals were obtained at two different laser beam angles: 44° and 28°. Distance between lasers was set to 7, 8 and 9 cm. It was not possible to track reflected dots if the distance between lasers was less than 7 cm.

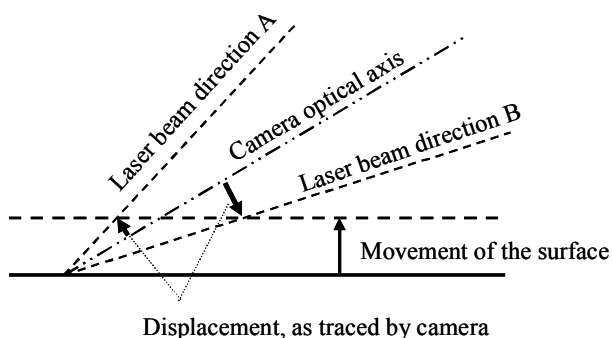


Fig. 4. Impact of geometrical configuration on the signal amplitude

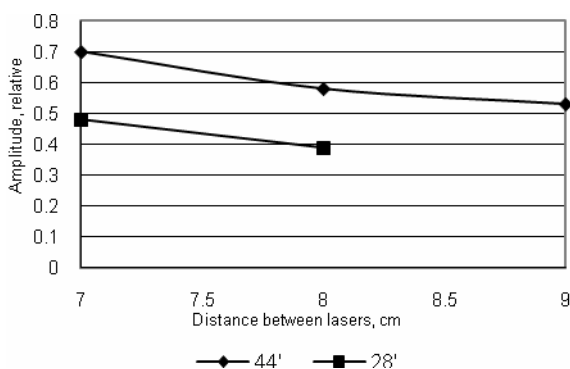


Fig. 5. Impact of the distance between lasers on the signal amplitude

If the distance between lasers is decreased, system assumes that the surface is positioned further away; therefore amplitude of the acquired signal is increased. Also it was determined that the amplitude of the signal will change by more than $\pm 5\%$, if the angle of laser beam will change by more than $\pm 10\%$ or the angle of camera – by more than $\pm 14\%$.

Since it is necessary to ensure that the same motion amplitude will result in the same signal amplitude regardless of geometrical configuration, the correction coefficient was introduced to calculate the true amplitude of the motion regardless geometrical positioning.

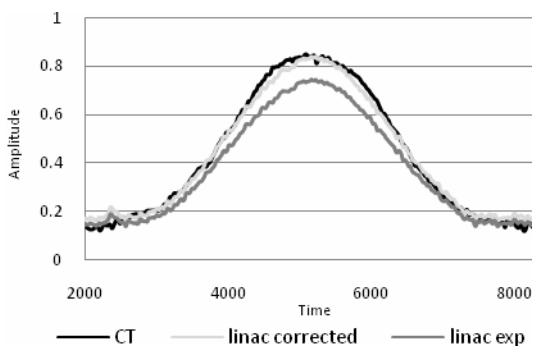


Fig. 6. Application of theoretically calculated correction coefficient

Fig. 6 illustrates breathing patterns, acquired at CT (Fig. 6, CT) and linac (Fig. 6, linac exp) under different

geometrical conditions: CT – angle of lasers 53° , angle of camera 16° ; linac – angle of laser 39° , angle of camera 13° . After application of correction coefficient, dependent on the geometrical configuration, to the values of amplitudes, obtained at linac:

$$Amp_{linac} = 0.8 \cdot Amp_{CT}, \quad (1)$$

patterns, obtained at CT room and linac room coincided (Fig. 6, linac corrected), therefore allowing gating.

The same result can be achieved, if, after one got reference signal at CT, test signal would be obtained at linac and used to calculate correction coefficient from measured data (Fig. 7).

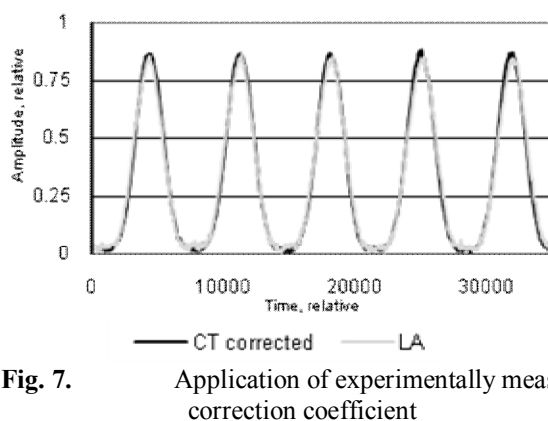


Fig. 7. Application of experimentally measured correction coefficient

Treatment simulation demonstrated, that film, irradiated while gating disabled, shows the movement pattern of the breathing phantom (Fig. 8). Two position of the iron screw nut, mounted at the top of the phantom, are clearly noticeable. Lower position corresponds to maximal “exhale”, but upper – to maximal “inhale”. Since “exhalation” phase lasts longer due to phantom construction, image at the lower position is brighter (film is less exposed).

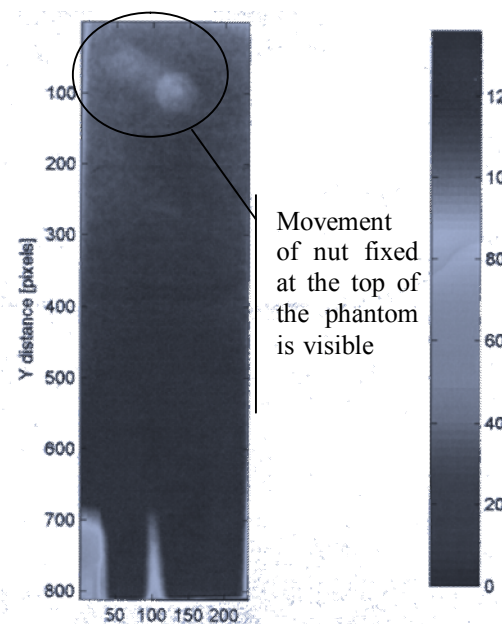


Fig. 8. Film irradiated while gating disabled

Second film was irradiated with gating enabled; gating threshold set to maximal inhalation phase. It is clearly visible that the phantom is fixed at the same position at any given breathing cycle (Fig. 9).

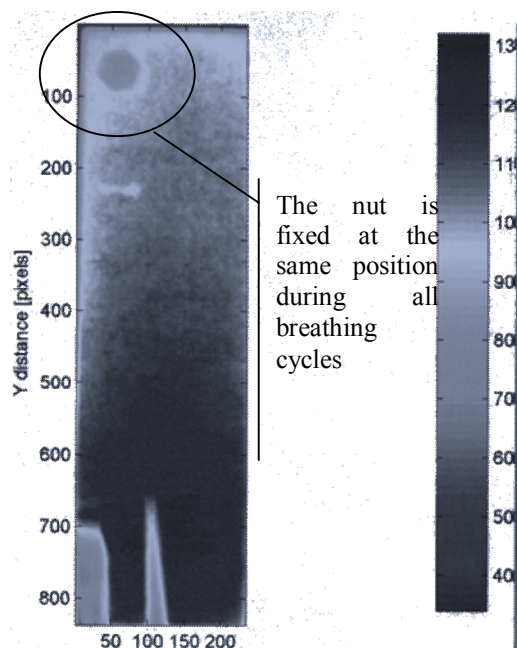


Fig. 9. Film irradiated while gating enabled

Both films were aligned using DoseLab 4.0 software [5] and plot representing absolute dose difference between both films was acquired (Fig. 10).

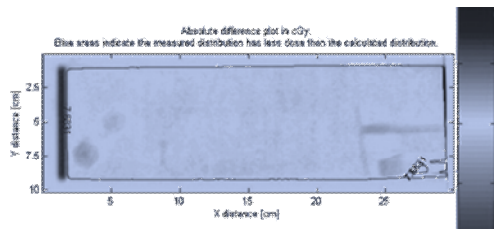


Fig. 10. Absolute dose difference plot

The plot shows, that enabling of the gating allowed synchronize switching of linac radiation beam with breathing phantom position.

4. Conclusions

The tests prove that laser beams can be used instead of marker block to acquire breathing patterns. Commercial system is able to recognize breathing phases correctly. It is possible to achieve reasonable recurrence of the signal amplitude, which is dependent mostly on the geometrical configuration, therefore allowing respiratory gating.

Method is rather sensitive to geometrical configuration that is why it is not suited for creating a system that would not require positioning. There are several options to ensure coincidence of the amplitude of reference signal and signal acquired during treatment, for instance, normalization of the signals or use of correction coefficients. Laser spot stereometry would become an another option.

5. References

1. Hellman S., Memorial Sloan-Kettering Cancer Center. A Practical Guide to Intensity-Modulated Radiation Therapy. Madison, 2003. 423 p.
2. Respiratory Gating Reference Guide 1.6, Varian Medical Systems, 2004
3. Aliverti A., Ferrigno G. and Pedotti A. Surface analysis by laser beam scanning and stereophotogrammetry. Proc. Spie 2067, 1993. p. 209-219.
4. Blums J., Katasevs A., Kudrjasovs O. No-contact methodology of human thorax form registration during breathing. Patent LVP-07-15.
5. DoseLab software homepage, Internet, <http://www.doselab.com>

THE IMPACT OF THE DETECTOR SIZE EFFECTS IN REGIONS OF HIGH DOSE GRADIENTS ON POINT DOSE MEASUREMENT

Sandija PLAUDE*, Arturs MEIJERS*, Sergey POPOV*, Albert MILLER** and Yuri DEKHTYAR***

* Latvian Oncology Centre of Riga Eastern Clinical University Hospital, Riga, Latvia

** Vilnius University Oncology Institute, Vilnius, Lithuania

*** Riga Technical University, Riga, Latvia

Abstract: Intensity Modulated Radiotherapy (IMRT) is an increasingly used treatment technique. Patient-related Quality Control (QC) is essential part of IMRT clinical implementation, therefore Intensity Modulated (IM) fields has to be verified prior to deliver of the IMRT plan to the patient. The aim of this study was to evaluate volume-averaging effect of different ionization chambers used for ionometric dosimetry of the IM fields.

Keywords: Intensity Modulated Radiotherapy, ionometric dosimetry, quality control.

1. Introduction

Intensity Modulated Radiotherapy (IMRT) belongs to the Conformal Radiotherapy (RT) technique that supplies a better dose conformity to the tumor volume and is more sparing for normal tissues.

Because of IMRT high complicity, it demands a reliable quality control both in operation of the equipment and in the delivery of treatment to individual patient [1].

Ionization chambers (IC) are the preferred radiation detectors for measuring absorbed dose by IMRT fields. Absolute dose measurements using IC is still the gold standard [2]. However dose measured with IC is just the average dose value over the IC volume [3]. Usually the beam central axis (CAX) is used for reference dose measurements, and absorbed dose variations within field covered by IC are not available for detection. As the result, accuracy of measured the dose provided by IMRT is reduced. Particularly, this is dramatic when the high gradient of doses should be supplied.

The detector having a finite size affects measurement results, detector size effect playing a role.

Recently many authors [1, 3, 7, 9] have studied influence of different detectors in regions with high-dose gradients, but most of these studies are devoted for measurements of small fields, treating with IMRT dynamic fields is a sum of such the small segments.

The main aims of this work was to evaluate influence of two IC and photon diode widely used for relative and absolute dosimetry of the IMRT fields on measured dose to both in static and dynamic modes.

2. Materials and methods

2.1. Detectors

The following detectors were chosen for the experiment (Fig. 1):

- 1) PTW 30006 "Farmer" type chamber with its active volume 0.6 cm^3 ;
- 2) PTW 31002 "Semiflex" type IC 0.125 cm^3 ;
- 3) Scanditronix Wellöfer semiconductor p-type diode model PFD^{3G}. This is an energy compensated photon diode with tungsten powder mixed with epoxy added behind the chip, to differentially absorb low energy scatter.

All of the detectors have cylindrical geometry with diameter of active area 6.1 mm, 5.5 mm and 2.0 mm respectively [4].

2.2. Test fields and their measurement approach

A static test field had sizes ($10 \times 10 \text{ cm}^2$). The point type dose measurements were made at the CAX of the field and at its penumbra region ten points.

The same points were chosen for the dynamic field that had the same sizes as the static one.

Radiation was supplied from linear accelerator Clinac 2100C/D (Varian Medical Systems).

This accelerator is equipped with a dual photon mode and a multileaf collimator (MLC). The MLC has 40 opposed leaf pairs. Each MLC leaf is 6 cm thick made from tungsten with leaf transmission 1.5% - 2% for 6MV photon energy. A width of each MLC leaf is 1 cm at the level of the isocenter.



Fig. 1. Radiation detectors used for phantom measurements. a) "Farmer" type chamber; b) "Semiflex" ionization chamber and c) Scanditronix Wellhöfer semiconductor p-type diode

Fields were radiated with 6MV photon beam with dose rate 300 MU/min.

Radiation beam incidence was perpendicular to the surface of a water phantom "Blue Phantom" from Scanditronix Wellhöfer. The dose measurements were performed at a depth 5 cm, and source-axis distance (SAD) was equal 100 cm. The latter corresponded to the isocenter plane.

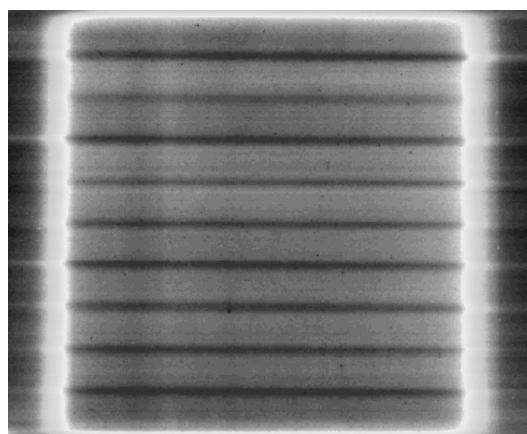


Fig. 2. Fluency of dynamic IMRT test field

The fluency of the dynamic test field was homogeneous at the middle (Fig. 2).

To get a dose profile for the dynamic IMRT field "sliding window" technique was employed. The results are presented in Fig 3. Dose profiles of static and dynamic test fields were acquired using radiographic film.

The penumbra regions of both of the static and dynamic test fields were scanned with 1 mm step. All measurements were normalized to the results achieved for CAX.

2.3. In-phantom measurements

ICs were positioned as their longitudinal axis was perpendicular to the beam axis, while diode was positioned in parallel against the beam axis.

Each detector was cross-calibrated in a CAX of the static field, the field size at CAX is sufficient to cover the detector homogeneously with radiation (the size of

the field was much larger than the size of the detector sensitive element).

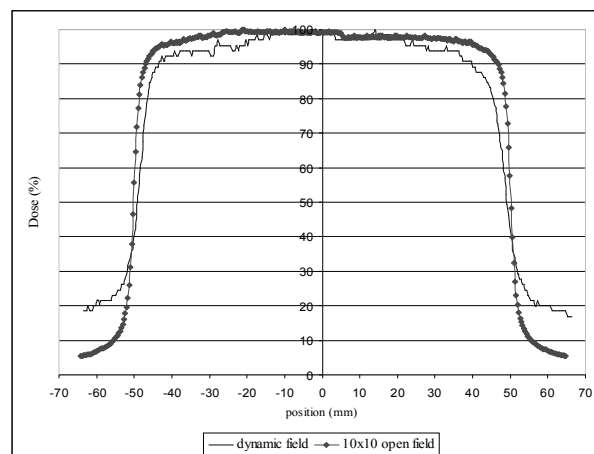


Fig. 3. Dose profiles of static and dynamic test fields acquired using film dosimetry

2.4. Film dosimetry

Fluencies of all test fields were verified using film dosimetry.

The films were radiated in water equivalent phantom at the same depth as the detectors. The Kodak[®] X-Omat films were in use for the measurements.

The films were calibrated using the method by [5]. Each film was exposed with 9 dose levels in a range 1.23 – 95.63 cGy (provided by the calibrated accelerator).

Irradiated films were digitized using the film scanner Vidar (Vidar Systems Corporation, USA) with resolution 75 dpi in 12 bit mode (point size 0.339 mm). Scanned films were stored in 12-bit TIFF format, for further processing using DoseLab 4.0 software [6]. Optical density of the film was converted to the dose using calibration curve, acquired by means of calibration film.

3. Results and discussion

Dose profiles, acquired in the 1 cm wide penumbra region of the static and dynamic fields presented in Figure 4.

The graph on the left (Fig. 4a), dose profiles for the static field demonstrates that IC with a large volume gives a smeared signal at dose gradient. The semiconductor detector gives more reliable dose distribution.

In a case of the dynamic mode (Fig. 4b), the influence of the size of detectors is small only close to the uniform dose region. In the high dose gradient region and low dose region the influence of the detectors is high.

To estimate results deviated by each detector, its measured data were extrapolated to the zero size detector. It is possible to extrapolate acquired data to a response of the detector with zero dimensions. In this way we can estimate deviation of each detector due to spatial resolution. In order to do this, the measurements results of all detectors at a single measured point were extrapolated with polynomial regression to detector size

with zero dimensions. Reconstructed penumbra represents results of polynomial regression analysis.

After that it is possible to calculate individual deviation for each detector under investigation (Figure 5).

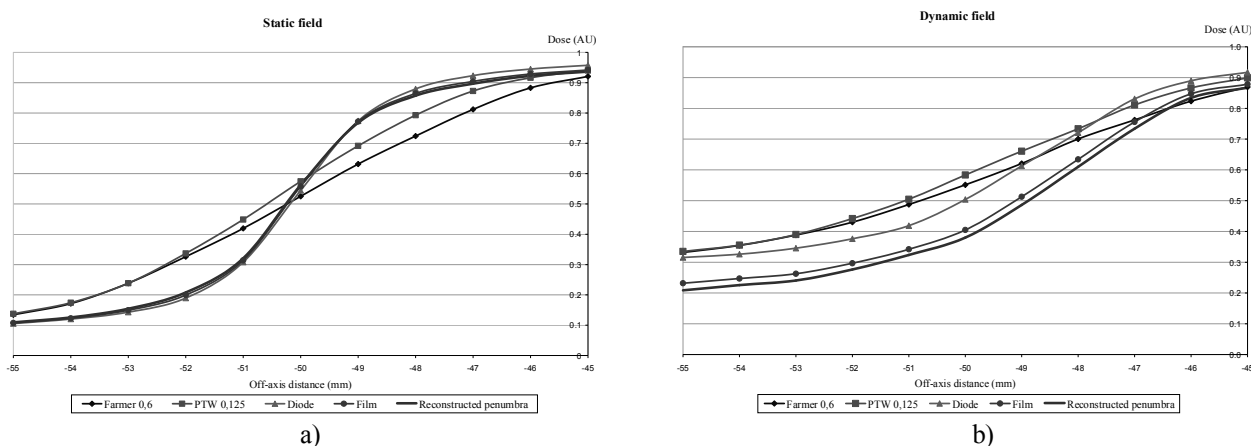


Fig. 4. Dose profiles in the penumbra region of a) static field and b) dynamic field acquired with different detectors

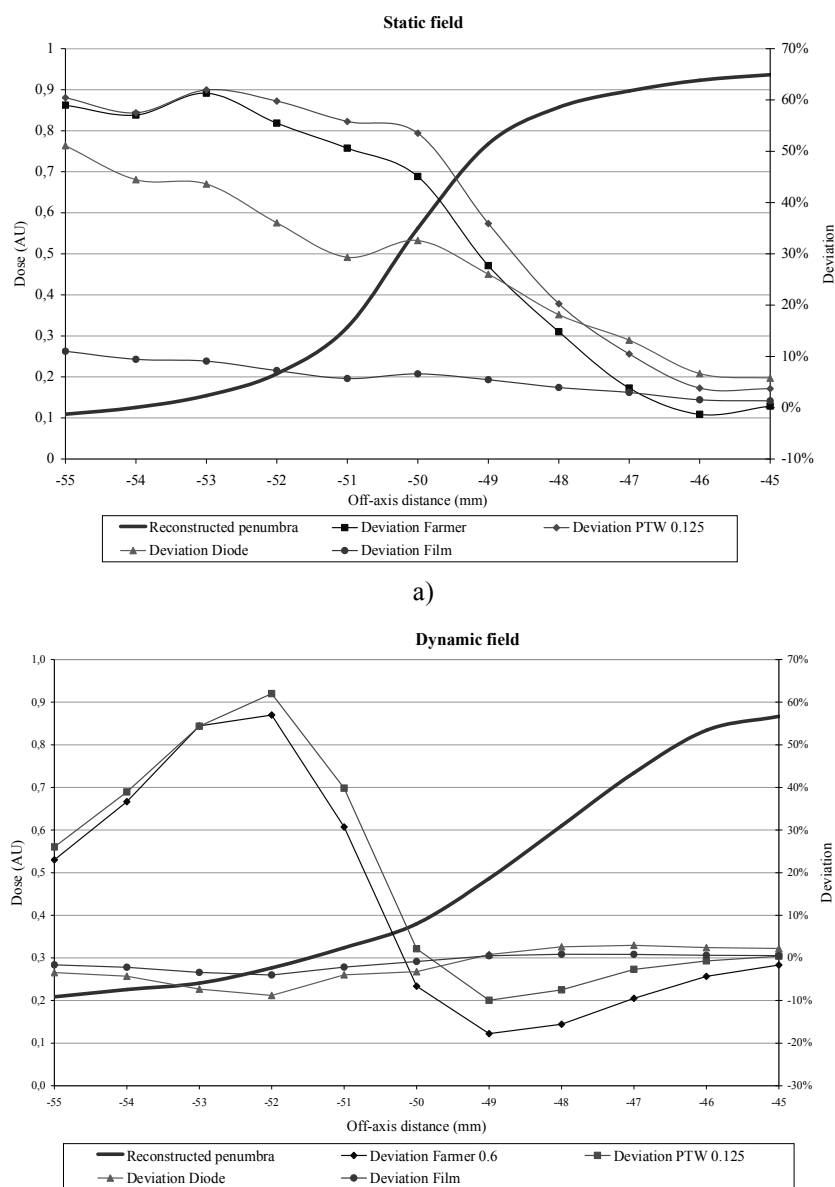


Fig. 5. Dose deviations from reconstructed penumbra for examined detectors for a) static field and b) dynamic field

Figure 5 shows dose deviations by each detector in contrast with a zero size detector. The Farmer type chamber shows greatest deviations that can be partially explained by its large sensitive volume, which is in accordance to literature data [7, 8]. Nevertheless one can see deviations of opposite sign in dynamic field as compared to static field for both ionization chambers.

4. Conclusions

IC that has a large sensitive volume (like a Farmer type detector) is not of preference to be in use for IMRT field dose measurements.

Both ICs have shown great differences of dose measurements in the region of high dose gradient. This can be partially explained by its large sensitive volume, but nevertheless there exist deviations of opposite sign in dynamic field as compared to static field for both ionization chambers. This fact could not be fully explained at present moment and requires additional investigation.

Measurements with other types of detectors should be performed further in order select the best detector to be in use for IMRT.

5. References

1. Sanchez-Doblado F, Capote R, Rosello J V et al. (2005) Micro ionization chamber dosimetry in IMRT verification: Clinical implications of dosimetric errors in the PTV. *Radiat Oncol* 75:342–348
2. Metcalfe P, Kron T, Hoban P, (2007) The physics of radiotherapy X-rays and electrons. Medical Physics Publishing, 2007. p.705
3. Stasi M, Biaiotto B, Barboni G et al (2004) The behavior of several micro ionization chambers in small intensity modulated radiotherapy fields. *Med Phys* 31:2792-2795
4. Technical Data, PTW-Ionization Chambers, PTW-Freiburg
5. Childress N.L, Dong L, Rosen I.I, (2002) Rapid radiographic film calibration for IMRT verification using automated MLC fields. *Med Phys* 29:2384-2390
6. DoseLab software homepage, Internet, <http://www.doselab.com>
7. Low DA, Parikh P, Dempsey JF et al (2003) Ionization chamber volume averaging effects in dynamic intensity modulated radiotherapy beams. *Med Phys* 30:1706–1711
8. Khan F.M, (2003) The physics of radiation therapy. Lippincott Williams&Wilkins, 2003. 560 pp.
9. Escude L, Linero D, Molla M et al (2006) Quality assurance for radiotherapy in prostate cancer: point dose measurements in intensity modulated fields with large dose gradients. *Int J Radiat Oncol BiolPhys*6:136-140

POSSIBLE APPLICATION OF VERIFICATION METHODS IN GAMMA THERAPY

Vanda ANDRIJAITIENĖ*, Diana ADLIENĖ**

* Klaipėda University Hospital, Liepojos g. 41, LT-92288 Klaipėda, Lithuania;

** Physics Department, Kaunas University of Technology, Studentų g. 50, LT-51368 Kaunas, Lithuania

Abstract: Verification systems which are integrated into modern radiotherapy equipment are used for checking and controlling of patient treatment. However old gamma therapy equipment with Co-60 source and without any verification system is still in use parallel to the modern linear accelerators in Lithuania. Due to this reason deviations in the prescribed, calculated and delivered radiation doses to the patient are possible.

TLD and EDR2 film dosimetry has shown that the difference between calculated and measured surface entrance doses varied between 2% and 10 %.

Uncertainties in the positioning of a patient and by deviations in radiation field geometry were estimated using XOMAT-V verification films. It was found that 50% of randomly selected patients were not positioned correctly. Corresponding doses were calculated using planning system COSPO.

Investigated quality control verification methods are compared to those used in the case of linear accelerator and possible applications of verification methods in gamma therapy are discussed in this article.

Keywords: gamma therapy, linear accelerator, patient treatment, quality control, dosimetry, verification

1. Introduction

Radiotherapy is one of the most important methods for cancer treatment. Development of the new radiation technologies makes it possible to determine more precise tumour size and location, surrounding healthy organs and tissues and to optimize the absorbed dose distribution. However it is not possible to overcome some uncertainties in the delivered dose to the patient which can occur during tumour size evaluation, dose planning and treatment of patient. Verification systems which are integrated into modern linear accelerators allows to quantify the above mentioned uncertainties, to control treatment of patients, to analyze the results and to make corrections if it is necessary [1, 3].

Performance of the quality control of patient's treatment is a special task for the personnel, which works with gamma therapy (Co-60 source) units. Special verification films could be used for a control of the geometry of irradiation fields and for a control of patient's position during the treatment using Co-60 unit [13] Patient's dose verification could be performed using *in vivo* thermoluminescence or film dosimetry methods [11, 12, 14].

The aim of present paper is to investigate possible quality control methods of patient's treatment using Co-60 units, to compare the results of investigation with the

results obtained from measurements using verification systems integrated into modern linear accelerators and to discuss the applicability of the different verification methods in gamma therapy (Co-60 units) in a daily practice of radiotherapy departments in Lithuania.

2. Materials and methods

Gamma therapy unit ROKUS-M with Co-60 source was used for the treatment of patients (Fig. 1).



Fig. 1. Gamma therapy unit ROKUS-M

Dose planning system COSPO was used for the patient's dose calculations.

X OMAT-V verification films with a size of 25,4cmx30,5cm were placed behind a patient and used for the control of patient's position during the treatment (one film for each irradiation field). This investigation was performed during the first treatment procedure of a cancer patient.

After the securing of the appropriate position of the patient LiF: Mg, Ti pellet (TLD) was placed in the central position of the irradiation field on the patient's surface and was used for the surface entrance dose measurements during the treatment. Dose D_{max} was calculated:

$$D_{max} = \frac{D_{TLD} \cdot F_{konv}}{PDD_{pav} \cdot F_{kal}} \quad (1)$$

D_{max} – dose at the depth of d_{max} ;

D_{TLD} – TLD, measured dose;

F_{konv} – calibration coefficient, which compares calibration dose and TLD dose at the depth of 0,5cm;

PDD_{pav} – depth dose on the surface (%);

F_{kal} – calibration coefficient which gives a ratio of D_{TLD} on the skin surface and D_{TLD} at the depth of 0,5 cm.

Dose measurement was repeated during the next treatment using Kodak EDR2 (extended dose range) films with a size of 35cmx43cm instead of TLDs.

Dose D_{max} was derived from the calibration curve (OT versus dose), calculated for EDR2 film (Fig. 2)

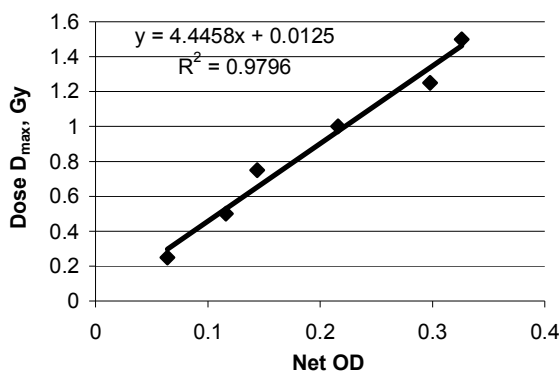


Fig.2. Calibration curve

Optical density of the irradiated films was evaluated using densitometer PTW Densi X 52001.

Investigation of disagreements in a prescribed and delivered to the patient dose caused by different factors was performed in the case of 16 randomly selected patients.

3. Results and discussions

Positioning

To show the influence of the irradiation field shift only by 1 cm from dose isocentre on the doses delivered to the patient during treatment (Pelvis region), 2D dose planning system COSPO was used. It was assumed that

this shift was caused by the incorrect positioning of the patient.

Possible uncertainties in the dose plan of the patient (one single case) are presented in Fig. 3.

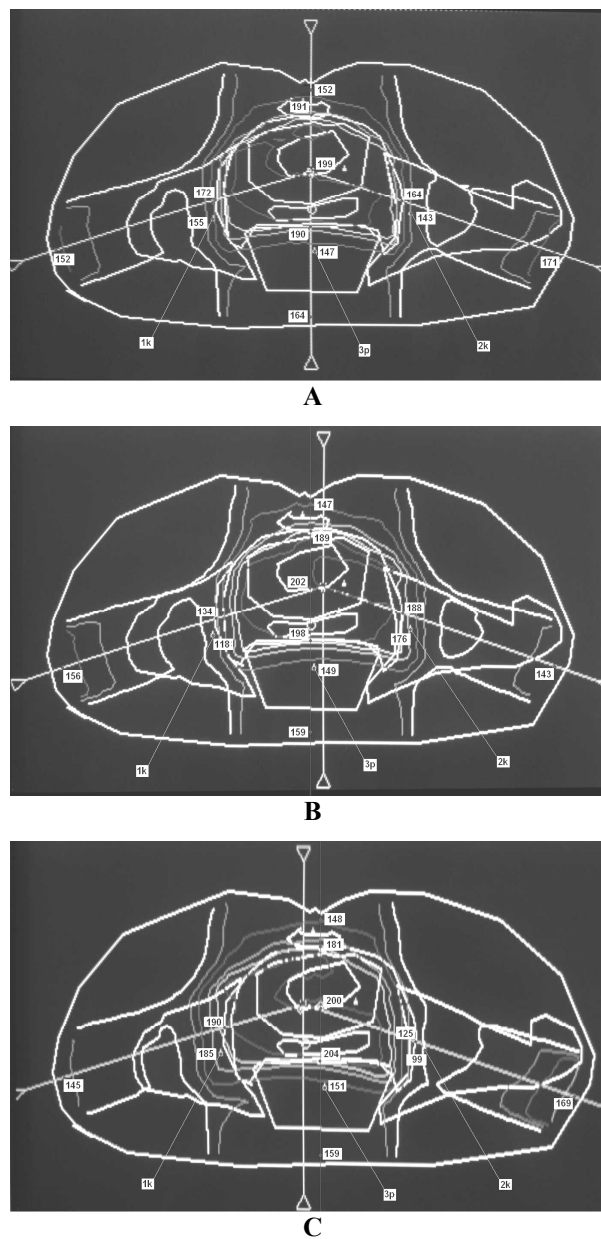


Fig.3. Distribution of isodoses: A – correct position; B – shift of the irradiation field to the left (1 cm); C – shift of the irradiation field to the right (1 cm).

According to the plan, the prescribed dose to the target was 50Gy, delivered in 2Gy fractions. For the simplicity, only PTV is indicated on the image.

Indicated critical organs are: 1k – left femoral head (tolerance dose – 60-65Gy), 2k – right femoral head (tolerance dose 60-65Gy); 3p – urine bladder (tolerance dose 52-65Gy).

Dose modelling results are presented in Fig. 4. The highest dose changes, caused by 1cm shift of the isocentre, were estimated for the critical organs: shift to the left was responsible for the increase of the point dose of 30cGy for one 2Gy fraction in the case of (1k) organs and decrease of the dose of 44cGy for one

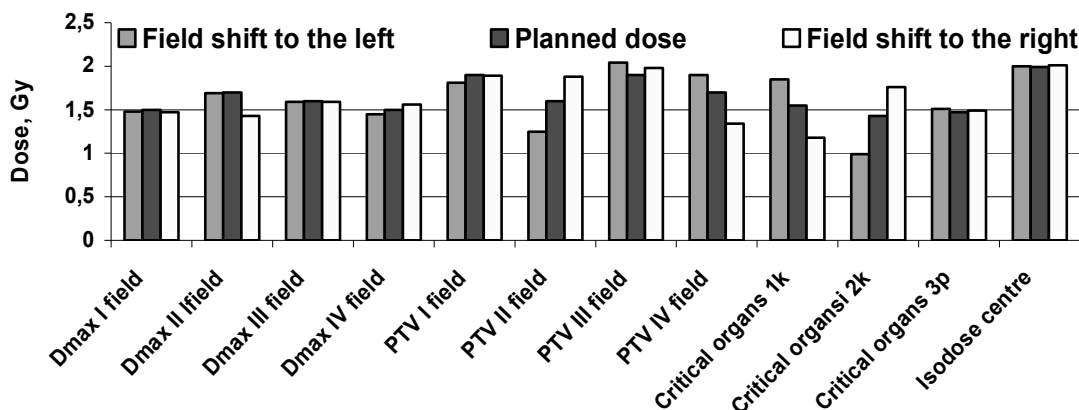


Fig. 4. Comparison of the doses

fraction in the case of (2k) organs. Shift to the right caused decrease of 37 cGy for (1k) organs and increase of 33 cGy for (2k) organs. Changes in the point dose for (3p) organs were not significant and varied in the range of 3%. Some changes in the dose were observed PTV II and PTV IV fields due to the shift.

Possible deviations from the planned doses caused by incorrect positioning of the patient were evaluated in 30 cases (Pelvis region) comparing CT image and the X-ray image obtained using verification film X OMAT-V. Results of the investigation are presented in Fig. 5

It was found that the biggest shift of the irradiation field caused by incorrect positioning of the patient was 4cm. Corrections in the patients positioning were necessary in more than 50% of all investigated cases.

Performed investigation showed that the quality of treatment procedure can be enhanced and tumour control achieved, if a controlling of the patient's position is undertaken. Application of special verification films in a daily practice before the first treatment of patient allows to check the positioning and to overcome possible mistakes of personnel.

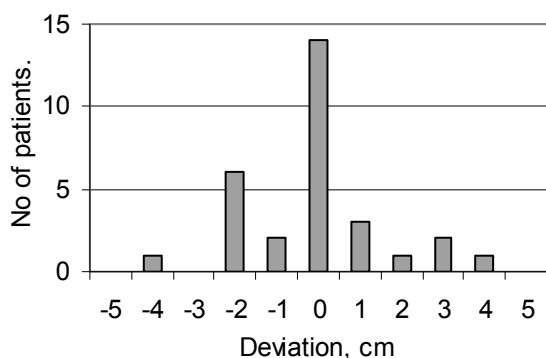


Fig. 5. Shift of the patient's irradiation field as compared to the dose plan

Dose plan verification

Surface entrance doses D_{max} at the point in the case of one irradiation field were evaluated by two methods: TLD and film dosimetry using verification films EDR2. Comparison of the calculated doses (dose planning system COSPO) and experimentally *in vivo* evaluated doses for 16 patients is presented in Fig.6

It is evident that the calculated and experimentally evaluated doses D_{max} differed not significantly. It was found, that the relative uncertainties for both experimental methods varied in the range within 11%: in the case of TLD measurements – from 0,4% to 10,5% (average value 5,9%) and in the case of EDR2 film dosimetry – from 0,9% to 9,2% (average value 4,7%).

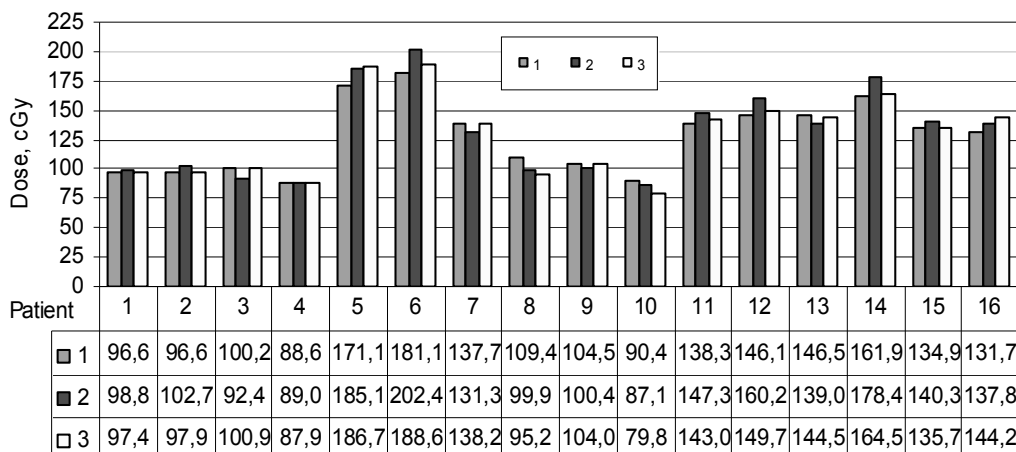


Fig.6. Comparison of surface entrance doses D_{max} : 1-TLD measurement; 2-planned dose; 3- EDR2 film dosimetry measurement

System error was not observed. Average values of the relative uncertainty in both cases were slightly higher as it is recommended [12].

4. Conclusions

1. Possible applications of different dose verification methods were investigated in the case when old gamma therapy unit with Co-60 source was used for the treatment of cancer patients.
2. It was shown that the positioning of patient for the treatment could cause some shift of radiation field which influences significantly the dose delivered to patient. Solution of this problem could be application of verification films in a daily practice before the first treatment and corrections of the patient's position according the verification results.
3. Two methods were applied for the evaluation of the experimental doses delivered to the patient during one treatment: TLD and EDR2 film dosimetry and special methods for the evaluation of the dose D_{max} were used. It was shown that calculated doses (planning system COSPO) and experimentally *in vivo* measured doses were slightly different. Relative uncertainties of the estimated doses varied within 11% in both cases. However average value of the relative error was only slightly higher as recommended 5%. According to the results of investigation it could be assumed, that EDR2 film dosimetry method under circumstances could be applied for the control of the delivered dose to patient. However in daily practice it is too complicated and uncertain.

5. Acknowledgements

This study was supported by Lithuanian State Science and Studies Foundation

6. References

1. Verellen Dirk, De Ridder Mark et al. Innovations in image – guided radiotherapy. Nature Reviews, Volume 7, December 2007.
2. Driver D. and Jane H. Dobbs Improvements in radiotherapy practice: the impact of new imaging technologies. Cancer Imaging (2004) 4, 142–150
3. Schlegel W., Bortfeld A. and Grosu L. New Technologies in Radiation Oncology, ISBN 978-3-540-00321-2 Springer Berlin Heidelberg New York, 2006, 324-327 p.
4. Holmberg O. Ensuring the Intended Volume is Given the Intended Absorbed Dose in Radiotherapy: Doctoral dissertation. Lund University/ Malmo, 2004.
5. Podgorsak E. B. Review of Radiation Oncology Physics: A Handbook for Teachers and Students; IAEA. – Vienna, 2003
6. Khan M. The Physics of radiation therapy. – Baltimore, 2003. – 456 p. ISBN 0-7817-3065-1
7. Michael A., G. Herman. Clinical use of Electronic Portal Imaging. Division of Radiation Oncology, Mayo Clinic, Rochester, 2004.
8. Soete G, Verellen D, Tournel K, et al. Setup accuracy of stereoscopic X-ray positioning with automated correction for rotational errors in patients treated with conformal arc radiotherapy for prostate cancer. Radiotherapy Oncology, 80:371–3, 2006
9. Langen K, M, Pouliot J, Anezinos C. et al. Evaluation of ultrasound-based prostate localization for image-guided radiotherapy. Int. J. Rad. Oncol. Biol. Phys., 57:635–44, 2003.
10. Litzenberg D. W, Willoughby T. R, Balter J. M, et al. Positional stability of electromagnetic transponders used for prostate localization and continuous, real-time tracking. Int. J. Radiat. Oncol. Biol. Phys; 68:1199–206, 2007.
11. Rizzotti A., Compri C. and Garusi G. F. Dose evaluation to patients irradiated by Co-60 beams, by means of direct measurement on the incident and on the exit surfaces. Radiother. Oncol. 3, 279-283, 1985.
12. VanDam J., Marinello G, Methods for in-vivo Dosimetry in external Radiotherapy, ESTRO, 1994.
13. Chengyu Shi, Nikos Papanikolaou, Yulong Yan, Xuejun Weng, and Hongyu Jiang. Analysis of the sources of uncertainty for EDR2 film-based IMRT quality assurance. Journal of Applied Clinical Medical Physics, Vol 7, No 2, 2006.
14. Leunens G., Van Dam J., Dutreix A. and van der Schueren E. Quality assurance in radiotherapy by in vivo dosimetry. Determination of target absorbed dose. Radiother. Oncol. 19, 73-87, 1990.
15. Whittington R, Bloh P, Hutchinson D et al. verification of prostate treatment setup using computed radiography for portal imaging. J Appl. Clin. Med Phys, 3(2):88-96, 2002.
16. Suriyapee S. et al. Optimal sensitometric curves of Kodak EDR2 film for dynamic intensity modulated radiation therapy verification, biomedical imaging and interventional journal, 4(1): e 4, 2008.

PRIEMONĖS IR PRIETAISAI RADIACINEI SAUGAI IR MONITORINGUI

UAB „Lokmis“, įkurta 1995 m., yra vienas pirmaujančių šiuolaikinės matavimo įrangos ir matavimo sprendimų tiekėjų Lietuvos rinkai. Kompanija siūlo kompleksines metrologinių, elektros, fizikinių matavimų, cheminės analizės ir telekomunikacijų sistemas, jų projektavimo, kalibravimo, įdiegimo ir aptarnavimo paslaugas. Pritraukdama įmonės mokslinį potencialą, UAB „Lokmis“ suteikia metodinę pagalbą konstruojant matavimo sistemas mokslinams ir techniniams tikslams spręsti. Būdamas stambiausių pasaulio matavimo įrangos gamintojų partneriu ir atstovu, UAB „Lokmis“ siūlo tik apčiuotus ir išbandytus produktus. Kompanija, sertifikuota pagal ISO 9001:2000 standartą, nuolat rūpinasi siūlomų sistemų kokybe ir patikimumu.

2005 m. UAB „Lokmis“ pradėjo naują veiklos kryptį, siūlydama branduolinės spektroskopijos, radiometrijos ir dozimetrijos sistemas. Šios sistemos naudojamos radiologinės saugos, radioaktyviųjų atliekų apibūdinimo, aplinkos monitoringo, fizinės saugos tikslams.

Siūlome Jums kompleksines sistemas ir sprendimus (matavimo įrangą su suderinta programine įranga, priedais, garantiniu ir pogaugantiniu aptarnavimu ir techniniu palaikymu):

Dozimetrines sistemas (asmens dozimetrija, TLD /EPD, aplinkos dozimetrija)

Radiometrus, radionuklidų kalibratorius

Radonometrus, jodo ir kitų medicininių izotopų identifikatorius

Portatyvius puslaidininkinius spektrometrus medicinos tikslams

Portatyvias patalpų oro ėmimo sistemas

Stacionarias ventiliacinių sistemų išlėkų monitoringo sistemas

Fantomus

Elektrometrus

Paviršinės taršos matuoklius

Radioaktyvius kalibracinius šaltinius, radionuklidų tirpalus

Radioaktyvių medicininių atliekų surinkimo konteinerius, manipulatorius

Kokybės užtikrinimo įrangą Rentgeno diagnostikoje

Apsaugos nuo alfa, beta, gama ir Rengeno spindulių priemonės, drabužius, deaktyvavimo priemonės

Kitus įvairius kompleksinius sprendimus pagal kliento užsakymą (pvz., mobiliųjų laboratorijų komplektavimas)



Rankų, rankų-kojų paviršinės taršos matuokliai,
Thermo Fisher Scientific

Mūsų partneriai:

Thermo
SCIENTIFIC

Thermo Fisher Scientific

plataus spektro radiometrinė ir dozimetrinė įranga
www.thermo.com/rmp

ORTEC®
ORTEC

branduolinės spektroskopijos sistemos www.ortec-online.com

BERTHOLD
TECHNOLOGIES

Berthold Technologies

radiometrinė ir spektrometrinė įranga radiologiniam monitoringui ir kontrolei www.bertholdtech.com

RTI

RTI Electronics AB

įranga kokybei užtikrinti Rentgeno diagnostikoje
www.rti.se

VSE PRO RTG
V.M.K.
ALL FOR X-RAY

V.M.K. spol. s.r.o.

apsauginės švinuotos priemonės fizinei saugai
www.vmk-rtg.cz



Apsauginiai drabužiai medicininiam personalui ir pacientams
V.M.K. spol. s.r.o

UAB „Lokmis“
Naugarduko 68B
LT-03203 Vilnius, Lietuva
Tel.: 8 5 215 18 95
Faks.: 8 5 215 17 46
El. paštas: office@lokmis.lt
www.lokmis.lt



IMAGE QUALITY ASSURANCE OF MEDICAL LCD DISPLAYS BASED ON AAPM TG 18 ACCEPTANCE PROTOCOL

Ivo PRUUL*, Anatoli VLADIMIROV**, Kalle KEPLER**

*Tartu University Hospital, Department of Medical Technology, Tartu, Estonia;

**University of Tartu, Training Centre of Medical Physics and Biomedical Engineering, Tartu, Estonia

Abstract: Image quality assurance should be of high priority in radiology departments. In recent years Estonian hospitals have gone over from hard copy (film) to soft copy (computer) display systems, but unfortunately image quality control is not yet done regularly on those systems. This pilot study was carried out in two major hospitals in Estonia. The protocol of the Task Group 18 of the American Association of Physicists in Medicine (AAPM) was used as a basis for assessment of medical displays. Minolta LS-100 photometer was used to measure luminance of the AAPM TG18LN digital test patterns. The luminance ratio (LR), maximum luminance (L_{max}) and deviation of contrast response with respect to that of DICOM GSDF were estimated for eight LCD displays. The maximum luminance non-uniformity (k_{δ}) was $26,5 \pm 4,4$ % for the 10% luminance of the TG-UNL10 test pattern. As in literature and in our measurements was proved DICOM calibration should be done regularly, once per year to maintain high performance of the displays and acceptable image quality.

Keywords: image quality assurance, medical displays assessment and calibration, DICOM Grayscale Standard Display Function, PACS

1. Introduction

In recent years Estonia has implemented a nationwide Picture Archiving and Communication System (PACS). The national Estonian PACS dates back to Baltic International Telemedicine Network (BITNET) project, launched in 1999. In 2001 a mini-PACS was created in Tartu University Hospital with two CT, one MRI and one CR system that were connected to a DICOM server. It received approximately 1 GB data per day. In 2005 Tartu University Hospital and North-Estonian Regional Hospital joined to create and maintain a nationwide PACS. Today this PACS has the total capacity of 100 TB. It receives images from over 80 modalities from 26 healthcare institutions and the daily archived data is in average 125 GB. Also it offers the opportunity to view images through secure Internet connection at healthcare institutions and by family practitioners all over the country and abroad [1].

After image acquisition, the image quality is optimized by image processing. Images are sent to electronic storage, display workstations (via PACS), or to a hard copy printer. The image display is the last link in the medical imaging chain and its performance affects the displayed image quality, as do the clinical setting and the ambient lighting conditions. Recently, much effort has been made to address the quality control aspects of

electronic display devices and to verify their physical characteristics [2]. When quality control standards for traditional film have been broadly developed, then soft copy display systems do not have many guidelines how to perform a quality control. Digital Imaging and Communications in Medicine (DICOM) standard specifies a function that relates pixel values (grey levels) to displayed luminance levels, Grayscale Standard Display Function (GSDF) [3]. Monitors that are calibrated to DICOM standard should always convert the same digital input values into the same luminance values. AAPM has provided the standard guidelines for the performance evaluation of electronic displays [4]. The AAPM document describes how to make quality assessments on medical display systems and also gives some acceptance criteria's for the display systems.

Measurements made in this study according to AAPM protocol proved that medical display quality control is necessary and DICOM calibrations should be done regularly. The maximum luminance non-uniformity (k_{δ}) was $26,5 \pm 4,4$ % for the 10% luminance of the TG-UNL10 test pattern. The maximum luminance values were greater than 170 cd/m^2 and the computed luminance ratio L'_{max}/L'_{min} was greater than 250 as recommended by AAPM TG18. Computed contrast values in dark and bright areas fall out of the standard

±10% tolerance limits. As the measured systems were calibrated 2 years ago, the degradation from DICOM standard luminance values was clearly seen. Also in those systems that were measured twice, before and after DICOM calibration, the amount of grayscale values that could be seen after the calibration increased, especially in dark and bright areas. This article discusses the importance of medical display quality control.

2. Materials and methods

In two major hospitals in Estonia, Tartu University Hospital and North-Estonian Regional Hospital, at eight workstations flat panel (LCD) medical displays were tested, in which six displays were of the model BARCO NIO E-2620, with matrix size of 1600x1200 (two megapixel) and two of the model BARCO NIO MDNG-5121 BB, with matrix size of 2048x2560 (five megapixel). Before starting the tests, displays were cleaned of dust, fingerprints and other stains and were correctly positioned to minimize any reflections. DICOM calibration was not made to BARCO NIO E-2620 monitors to assess their present situation. Only BARCO NIO MDNG-5121 BB monitors were measured twice, before and after DICOM calibration, to assess the improvement. Minolta LS-100 photometer was used to measure luminance. The LS-100 has a 1° acceptance angle, wide range of luminance levels from 0.001 to 999.900 cd/m² and a luminance precision of less than ±2% ±1 digit of the reading. All measurements were made in near darkness and for that a light-blocking baffled tube was used. The measurements were made using AAPM standard patterns. AAPM TG18-LN pattern was used to assess luminance response and TG18-UN pattern was used to assess the display luminance non-uniformity in five different locations on the display, in the centre and in the corners.

2.1. DICOM 3.14 Grayscale Standard Display Function

The American College of Radiology (ACR) and the National Electrical Manufacturers Association (NEMA) formed a joint committee to develop a standard for Digital Imaging and Communications in Medicine.

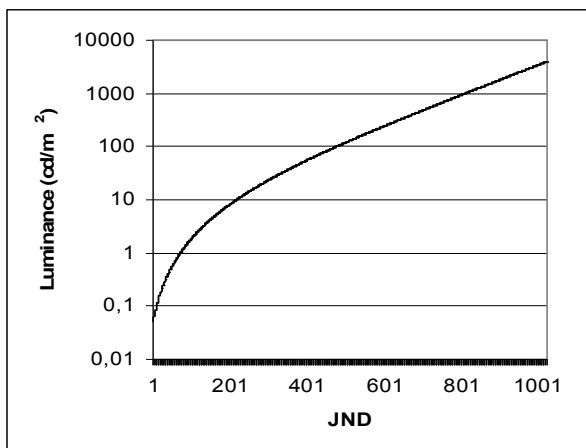


Fig. 1. Luminance as a function of Just Noticeable Difference (JND) index as defined by Barten [5].

While other parts of the DICOM Standard specify how digital image data can be moved from system to system, it does not specify how the pixel values should be interpreted or displayed. DICOM 3.14 specifies a function that relates pixel values to displayed luminance levels [3]. In medical imaging, it is important that there be a visual consistency in how a given digital image appears, DICOM 3.14 was developed to provide an objective, quantitative mechanism for mapping digital image values into a given range of luminance. An application, which knows this relationship between digital values and display luminance, can produce better visual consistency in how that image appears on diverse display devices. The relationship that DICOM 3.14 defines between digital image values and displayed luminance is based upon measurements and models of human perception over a wide range of luminance. There exists several models of human visual system, but the Barten model [5][6] is most frequently used. Human contrast sensitivity is distinctly non-linear within the luminance range of the Grayscale Standard Display Function. The human eye is relatively less sensitive in the dark areas of an image than it is in the bright areas of an image. This variation in sensitivity makes it much easier to see small relative changes in luminance in the bright areas of the image than in the dark areas of the image. Based on Barten’s model a unit called just noticeable difference (JND) was defined. JND is the luminance difference of a given target under given viewing conditions that the average human observer can just perceive. The Grayscale Standard Display Function is defined by a mathematical interpolation of the 1023 luminance levels derived from Barten’s model. The Grayscale Standard Display Function allows calculating luminance, *L*, in candelas per square meter, as a function of the JND index *j* [3]:

$$\log_{10} L(j) = \frac{a + c \cdot \ln(j) + e \cdot (\ln(j))^2 + g \cdot (\ln(j))^3 + m \cdot (\ln(j))^4}{1 + b \cdot \ln(j) + d \cdot (\ln(j))^2 + f \cdot (\ln(j))^3 + h \cdot (\ln(j))^4} \quad (1)$$

with *Ln* referring to the natural logarithm, *j* the index (1 to 1023) of the luminance levels *L_j* of the JNDs, and the constants *a, b, c, d, e, f, g, h, k* and *m* have been defined by DICOM 3.14 [3]. Fig. 1 indicates that the human eye is relatively less sensitive in the dark area compared to bright area. Indeed, over the luminance range 0.1 to 10 cd/m² (two orders of magnitude) there are around 200 JND while over the range 10 to 1000 cd/m² (also two orders of magnitude) there are around 600 JND available. When luminance exceeds 10 cd/m², the human eye follows almost purely logarithmic behaviour [7].

It is important to recognize certain limitations of the DICOM standard response. When viewing the varied brightness of a medical image, the human visual system adapts to the average quantity of light falling on the retina [4]. This is referred to as fixed adaptation. However, the DICOM 3.14 luminance response is based on contrast threshold data that is derived from

experiments where the background luminance is changed to equal the luminance of the target pattern, and the observer fully adapts to the new background. The contrast threshold associated with the GSDF thus reflects variable adaptation. When the eye is adapted to the mixed bright and dark regions of a medical image, the contrast threshold as a function of luminance differs significantly from that associated with variable adaptation [8]. Fig. 2 shows that the visual contrast response under fixed adaptation conditions is worse in the bright and dark areas of an image. This means that for the brighter and darker image parts, a JND corresponds to larger luminance differences than GSDF predicts and therefore subtle luminance differences will be more difficult to see. The number of gray shades that can be simultaneously perceived by a human observer as described by GSDF should be considered as an upper limit [4].

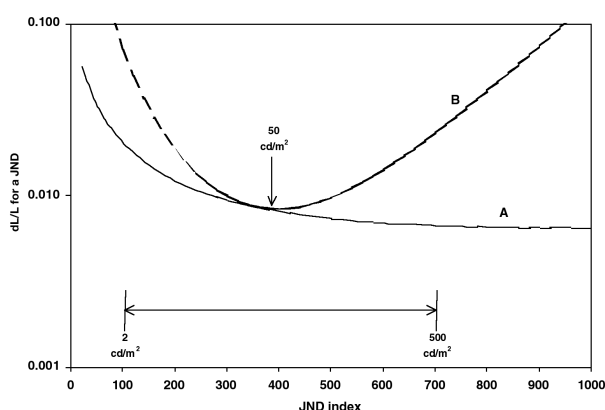


Fig. 2. Contrast threshold for variable (A) and fixed (B) visual adaptation [9].

2.2. AAPM TG 18

According to the American Association of Physicists in Medicine professional guidelines [10], the performance assessment of electronic display devices in healthcare institutions falls within the professional responsibilities of medical physicists. The intent of the report Assessment of Display Performance for Medical Imaging Systems was to provide standard guidelines to practicing medical physicists, engineers, researchers, and radiologists for the performance evaluation of electronic display devices intended for medical use.

Table 1. Some selected acceptance criteria of AAPM TG18 [4].

| Parameter | Acceptance criteria |
|-------------------------------------|---------------------------|
| Maximal luminance (L_{max}) | $\geq 170 \text{ cd/m}^2$ |
| Luminance ratio (LR) | > 250 |
| Luminance uniformity (k_δ) | $< 30\%$ |

The scope of AAPM TG 18 report is limited to display devices that are used to display monochromatic medical images. It describes how to assess geometric distortions, display reflection, luminance response, luminance spatial and angular dependencies, display resolution, display noise, veiling glare and display chromaticity. Also it gives suggested acceptance criteria for display systems (Table 1) [4].

2.3. Luminance response

Using the Minolta LS-100 and the TG18-LN test patterns, the luminance (L_i) in the test region was measured for the 18 p-values (grayscale values). Using a baffled tube eliminated the effect of ambient illumination. Ambient luminance value (L_{amb}) was measured by putting the display into power-save mode. The real luminance values (L'_i) were calculated by the addition of the luminance values and the ambient luminance value.

$$L'_i = L_i + L_{amb}. \quad (2)$$

In order to relate measured luminance values to the DICOM 3.14 standard luminance response, the gray levels used in the 18 measurements of luminance were transformed to JND indices. Using the DICOM's table of JND indices versus luminance, the JND indices for the measured minimum and maximum luminance (L'_{min} and L'_{max}), J_{min} and J_{max} , were identified. The JND indices for the intermediate values were then calculated

$$J_i = J_{min} + \frac{P(J_{max}-J_{min})}{\Delta P}, \quad (3)$$

where J_i indicates the JND indices and P is p-value or grayscale value.

The expected response of quantitative measurements was evaluated in terms of the contrast response. The observed contrast (δ_i) was computed as

$$\delta_i = \frac{2(L_i - L_{i-1})}{(L_i + L_{i-1})(J_i - J_{i-1})}, \quad (4)$$

The expected response according to GSDF was similarly computed as

$$\delta_i^d = \frac{2(L_i^d - L_{i-1}^d)}{(L_i^d + L_{i-1}^d)(J_i - J_{i-1})}. \quad (5)$$

As a quantitative criterion for medical displays, the measured contrast response at any given point should fall within 10% of the standard. This criterion applies specifically to contrast evaluated from the 18 measurements of luminance made at uniformly spaced p-value intervals [4].

2.4. Luminance non-uniformity

Luminance non-uniformity refers to the maximum variation across the display area. Using the TG18-UN test pattern the luminance was measured in five different spots on the screen. Luminance non-uniformity was calculated as

$$k_\delta = 200 * \frac{(L_{max} - L_{min})}{(L_{max} + L_{min})} \quad (6)$$

The maximum luminance deviation should not be bigger than 30% [4].

3. Results and discussion

The tests started with six Barco NIO E-2620 displays. The results are shown in Table 2 (result \pm uncertainty).

In Table 2 we can see that the maximum luminance value is greater than 170 cd/m² as recommended by AAPM TG18. The computed luminance ratio L_{max}/L_{min} for Barco NIO E-2620 displays were greater than 250. The luminance non-uniformity is less than the 30% luminance difference criterion. The contrast response of six Barco NIO E-2620 displays was calculated and shown in Fig. 3, which shows that the contrast values in dark and bright areas fall out of the standard $\pm 10\%$ tolerance limits. It indicates that without regular quality control the luminance values degrade from the DICOM standard luminance values.

Table 2. Maximum luminance (L_{max}), luminance ratio (LR) and luminance non-uniformity (k_{δ}) measured for BARCO NIO E-2620 displays.

| Monitor # | L_{max} (cd/m ²) | LR | k_{δ} (%) |
|-----------|--------------------------------|-------|------------------|
| 1 | 295±7 | 650±4 | 15±3 |
| 2 | 441±10 | 432±3 | 19±4 |
| 3 | 464±11 | 313±4 | 14±5 |
| 4 | 469±11 | 292±3 | 13±5 |
| 5 | 466±11 | 367±3 | 12±5 |
| 6 | 473±11 | 413±3 | 15±5 |

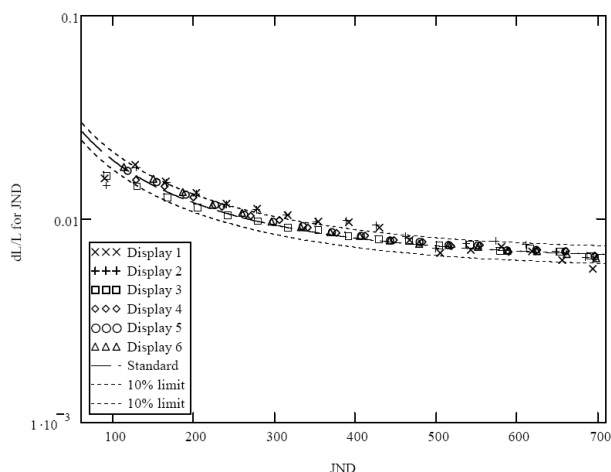


Fig. 3. Contrast response computed from 18 gray levels, related to the expected contrast response associated with the GSDF with 10% tolerance limits for BARCO NIO E-2620 displays.

The same tests were done with two BARCO NIO MDNG-5121 BB displays. The measured maximum luminance, calculated luminance response and luminance uniformity is shown in Table 3. The maximum luminance values were over the AAPM criteria of 170 cd/m² for all the displays. The computed luminance ratio L_{max}/L_{min} for all displays was greater than the minimum level recommended by AAPM TG18.

Table 3. Maximum luminance (L_{max}), luminance ratio (LR) and luminance non-uniformity (k_{δ}) measured for BARCO NIO MDNG-5121 BB displays before and after DICOM calibration.

| Monitor # | L_{max} (cd/m ²) | LR | k_{δ} (%) |
|------------|--------------------------------|-------|------------------|
| 7 (before) | 460±8 | 768±4 | 20±5 |
| 8 (before) | 449±8 | 787±4 | 26±4 |
| 7 (after) | 457±10 | 775±4 | |
| 8 (after) | 442±10 | 774±4 | |

The contrast response was calculated and shown in Fig. 4, which shows that before the DICOM calibration the luminance values did not match with the DICOM standard luminance values, especially in the dark and bright areas, where measured values are out of the 10% tolerance limits. After the calibration measured values followed the DICOM GSDF curve.

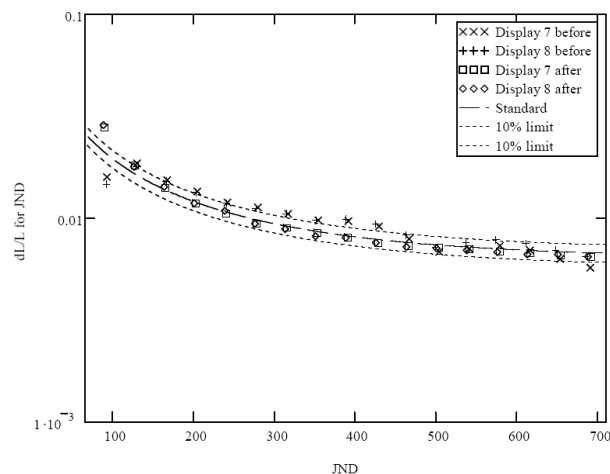


Fig. 4. Contrast response computed from 18 gray levels, related to the expected contrast response associated with the GSDF with 10% tolerance limits for BARCO NIO MDNG-5121 BB displays.

The maximum luminance non-uniformity for all displays was less than 30% luminance difference criterion recommended in the AAPM TG18 protocol.

4. Conclusion

In this study 8 medical display systems have been tested using the AAPM TG18 protocol. Tests before the calibration had some non-acceptable results in the dark and bright areas. After the calibration all test results met the criteria recommended by the AAPM TG18 protocol and were fully acceptable for diagnostic imaging. The test results confirmed that DICOM calibration is necessary to be done regularly. Without quality control the display system degradation from DICOM standard luminance values are clearly seen and those systems may cause false diagnosis.

5. References

1. Aavik A., Allik T., Nazarenko S., Paats A., Raudsepp R., Ross P., Simisker A., Tõnnov A., Ulst M. National PACS Programme in Estonia - Results and Successes. Imaging Management, 7, 12, (2007). p. 18-20, 41.
2. Jung H., Kim H-J., Kang W-S., Yoo S. K., Fujioka K., Haseqawa M., Samei E. Assessment of flat panel LCD primary class display performance based on AAPM TG 18 acceptance protocols. Medical Physics, 31, 7, (2004). p. 2155-2164.
3. National Electrical Manufacturers Association. Digital Imaging and Communications in Medicine

- (DICOM) Part 14: Grayscale Standard Display Function. <http://medical.nema.org/>, (2008).
4. Samei E., Badano A., Chakraborty D. Assessment of display performance for medical imaging systems. <http://deckard.mc.duke.edu/~samei/tg18>, (2005).
 5. Barten PGJ. Contrast Sensitivity of the Human Eye and Its Effects on Image Quality. Bellingham, WA: SPIE Press, (1999).
 6. Barten PGJ. Physical model for contrast sensitivity of the human eye. Proc SPIE Int Soc Opt Eng, 1666, (1992). p. 57-72.
 7. Kimpe T., Tuytschaever T. Increasing the Number of Gray Shades in Medical Display Systems – How Much is Enough? Journal of Digital Imaging, 20, 4, (2007) . p. 422-432.
 8. Samei E. Digital mammography displays. In: Karellas A., Giger A. Advances in Breast Imaging: Physics, Technology, and Clinical Applications. RSNA Categorical Course Syllabus. Oak Brook, IL: Radiological Society of North America (RSNA), (2004). p. 135-143
 9. Flynn MJ., Kanicki J., Badano A., Eyler WR. Highfidelity electronic displays of digital radiographs. Radiographics, 19, (1999), 1653-1669.
 10. Barnes GT., Bronskill MJ., Fox MF., Frey GD., Haus AG., Madsen MT., Pavlicek W., Reed SA., Wenstrup RS. AAPM Report No. 42. The Role of the Clinical Medical Physicist in Diagnostic Radiology, Report of the AAPM Task Group No. 2. Woodbury, NY: American Institute of Physics, (1994).

ADAPTATION OF COMPUTED TOMOGRAPHY QUALITY CONTROL METHODS FOR TESTING LABORATORY

Joosep KEPLER*, Kalle KEPLER**

*Tartu University, Faculty of Science and Technology, Tartu, Estonia;

**University of Tartu, Testing Centre, Tartu, Estonia

Abstract: During the past two years the number of computed tomography (CT) scanners has been doubled and during the past seven years the number of CT examinations has been quadrupled in Estonia. In CT patient dose could exceed doses that of conventional radiography more than 50 times. Dose and image quality management depends mainly on the CT scanner settings and performance. European guidelines have been given for the regular quality assessment to avoid malfunctioning and overdoses in CT. Quality assessment and dose measurements has been carried out in other European countries and in USA for decades, while in Estonia it has been done quite sporadically. Since 2007 the Testing Centre of the University of Tartu has carried out CT quality control tests on-site in hospitals. In this article is given an overview of specifying and amending methodology for testing centre, based on the comparison of usage of the European, UK, USA, Nordic and other national standards and criteria. Choosing of the methods was based on existing standard head and body phantoms, dose measuring equipment and software. It was attempted to select the basic quality control methods, which would be most appropriate for field measurements and in the same time not spending too much clinical time.

Keywords: computed tomography (CT), quality assessment, CT dose index (CTDI), CT number, dose length product (DLP), image uniformity, image noise, testing laboratory

1. Introduction

Computed tomography (CT) has become an important diagnostic method among today's diagnostic imaging technology due to 3D capabilities and option for viewing only organs or different tissues makes CT quite popular. But compared to conventional radiography organ doses from CT scanning are considerably larger than those from corresponding conventional radiography. For example, a conventional anterior-posterior abdominal x-ray examination results in a dose to the stomach of approximately 0,25 mGy, which is at least 50 times smaller than the corresponding stomach dose from an abdominal CT scan [1]. While good image quality needs higher doses, it is always needed to make a compromise between higher noise and higher dose. Using methods for assuring quality in CT and keeping doses at low level is also strongly recommended by European Commission [2].

For one measure to keep doses at lower levels, European medical physicists and radiologists have suggested reference values with which the mean doses should be compared [3].

The number CT scanners has been doubled in recent years in Estonia and in May 2008 there were 21 CT

scanners altogether in Estonian hospitals [4]. While in 2001 there were totally 35 000 CT scans performed in Estonia, the number of CT scans in 2006 was already 125 000, increasing from 4% to 12% of all diagnostic procedures which use x-rays [5].

Believing that medical doctors will use CT diagnostics only when it is justified, one can still doubt if the CT-scanner's automated systems work without malfunctioning. According to European directives, a regular quality assessment must be carried out to minimize the chance of working with malfunctioning equipment and overdoses. While there are standards for measuring CT dose and image quality, it is still complicated to compare the test results due to different manufactures protocols.

In most European countries and in USA the quality assessment of CT has been carried out for decades, yet in Estonia it has been done quite sporadically [6,7]. Since 2007 Testing Centre of the University of Tartu has carried out systematic CT scanner quality control measurements on-site at hospitals. This article gives an overview of developing and specifying methodology in this field for a testing laboratory. This work is based on recommended European [3], UK [8, 9], USA [10],

Nordic [11] and other [12] national standards and criteria and on the comparison of the relevant methods. Different standards and guidelines from different countries might name principally the same methods with different names. For this reason the names of the methods named here are based on W. A. Kalender classification [13], which is based on the relevant IEC standard [12].

2. Instruments and methods

2.1. Usage of CT quality control methods

The methods recommended by IPEM [8], AAPM [10], BIR [9], IEC [12], CEC [3], NRPC [11] and also including UT (Tartu University Testing Centre selected tests) are summed up in table 1, showing whether it is used (marked with X) or is not used (left blank). With "A" are marked tests that are done by radiology technicians (radiographers) and "B" means that these tests are done by medical physicists. Differences between the named standards have not been discussed here and details can be found from the references below.

Table 1. Comparison of usage of the methods recommended by different standards and guidelines.

| Test parameter | IPEM [8] | AAPM [10] | BIR [9] | IEC [12] | CEC [3] | NRPC [11] | UT |
|--|----------|-----------|---------|----------|---------|-----------|----|
| CT values | A, B | X | A | X | X | X | X |
| Uniformity | B | X | | X | X | X | X |
| Noise | A, B | X | A | X | X | X | X |
| Spatial resolution | B | X | | X | X | X | |
| Low-contrast resolution | | X | | X | | X | |
| Slice thickness | B | X | | X | X | | |
| Dose profile | B | X | | X | | X | |
| CTDI and DLP (in air, with head phantom and with body phantom) | B | X | | X | X | X | X |
| Accuracy of table position | A | | | X | X | | |
| Light localizers | A | X | | | | | |
| Gantry tilt | | | | X | | | |

2.2 Standard phantoms, stands and measuring devices

The head phantom was a cylindrical (16 cm diameter, 14 cm length) solid tissue equivalent epoxy phantom with five 13,1 mm diameter holes drilled parallel to its long axis, one at the axial centre and four around the perimeter, 90° apart and 1 cm from the edge. Each of the holes used to be plugged with a cylindrical solid epoxy rod. The body phantom is similar to the head phantom, with a 32 cm diameter, 14 cm length. The

comparison of the standard epoxy phantom and the standard PMMA phantom was carried out few years ago in Karolinska University Hospital (Sweden) and the results tend to be almost the same, with differences in the range of some percents [6].

For holding quality phantoms in gantry's centre manufacturers usually use head socket at the top of patient table. In some countries (e.g. in Finland) a special textile bag is used to hold phantoms at right place. In our methodology it was decided to use a wooden stand made of 10 cm x 10 cm beams. Scattering and absorbing effects of used beams are discussed in section 3.

DLP measurements were performed using a pencil shaped ionisation chamber Model DCT 10 RS Lemo (RTI Electronics AB, Sweden) connected to electrometer module Barracuda (RTI Electronics AB, Sweden) and placed along the axis of rotation of scanner. The electrometer in its turn is connected to a laptop using COM/USB cable. Information on measured doses and waveform images was displayed and recorded by oRTIgo QA and Dosimetry software that came in bundle with the Barracuda system. The system is calibrated according to International Electrotechnical Commission (IEC) standards and is traceable to SSI (Sweden Radiation Protection Authority). According to the device's original documentation, standard uncertainty of the ion-chamber is within $\pm 3\%$, and standard uncertainty of whole system including the electrometer and the ion-chamber is within $\pm 4\%$.

2.3. Selection of methods for testing laboratory

Selection of methods for testing laboratory was based on existing test phantoms and measuring equipment. It was tried to take into consideration that CT scanners are used in clinical practice, so tests should not take very long time (not exceeding about 3 hours), which means that meanwhile no patients could not be scanned. Positioning lights and table movement accuracy tests are left out because radiology technicians at hospitals can carry out these tests easily.

While for patient safety radiation measuring is most important, but for the diagnosis better image quality (uniformity and less artefacts) is most important.

Taking into consideration of all these factors tests listed in table 1 at column labelled UT were chosen. Optimising of the methods was carried out in four Estonian hospitals and the best order considering time and protocol efficiency was:

- 1) CT-number constancy, uniformity and noise tests
- 2) Dose measurement with body phantom,
- 3) Dose measurement in air,
- 4) Dose measurement with head phantom,

The frequency of these tests done by medical physicists is 2 years due to practical considerations. The same test frequency is also required for other x-ray equipment and must be followed for getting permission for radiation activity in Estonia.

3. Results and discussion

CT scanner test results and specifications are given as an example in case of BrightSpeed Elite (GE).

3.1. CT-number constancy, uniformity and noise tests

For this test a body phantom was placed at the centre of gantry and scanned using standard clinical abdomen protocol. For viewing and calculating mean and standard deviation (noise) values a freeware program ImageJ 1.38x [14] was used. Main scanning parameters (tube potential, current, etc) were recorded.

ROI (Region Of Interest) was positioned into the central region and also into four peripheral areas shown in figure 1. The size of each ROI was approximately 40x40 mm, depending on reconstruction matrix used. The mean values for peripheral CT-numbers were 115,7 HU, 115,4 HU, 116,2 HU and 115,8 HU at areas described in figure 1 with angles 45°, 135°, 225° and 315° respectively. Mean value of central mean CT-number was 116,0 HU.

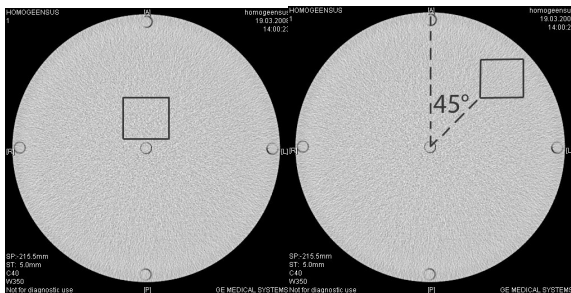


Fig. 1. In the left side is shown how the central ROI (few millimetres above central rod image) is positioned. In the right side is shown one of the peripheral ROI-s while other peripheral ROI-s are at angles 135°, 225° and 315° from vertical axis. All peripheral ROI-s are placed few millimetres below surface line.

For evaluating results and making sure that equipment is compliant these results were compared to different criteria. For uniformity estimation the IEC [12] criteria was used: ununiformity (difference between central and peripheral values) should be less than 4 HU. For CT-number constancy test the IPEM [8] criteria was used that difference from base level more than 10 HU is remedial level and 30 HU for suspension level is used. For noise test the IEC [12] criteria was used that measured noise values should not differ from values given in accompanying documents more than 15% and if no values are given, then 10% difference from base value would be remedial level and 25% difference would be suspension level.

3.2 CT dose index and dose length product tests.

Ionisation chamber was placed at the centre of gantry using a phantom as a stand (must not cover the x-ray beam) to hold it in place and dose length product (DLP) in air was measured. From measured DLP value, a normalized (for radiographic exposure 100 mAs) computed tomography dose index is calculated by the formula

$${}_nCTDI_{air} = \frac{DLP}{N \cdot T \cdot C}, \quad (1)$$

where DLP is measured dose length product (mGy-cm), N is the number of slices in a single scan, T is slice thickness (cm), C is radiographic exposure of 100 mAs. Test results are shown in table 2.

Table 2. Measured and calculated values for dose index and dose length product in air.

| Measured DLP, mGy-cm | Normalized dose index ${}_nCTDI_{air}$, mGy/100 mAs |
|----------------------|--|
| 85,3 | 43,1 |
| 85,1 | 43,0 |
| 85,0 | 42,9 |

For estimating test results in air a criteria from IPEM [8] quality program should be used: test results difference from the baseline more than 15% is remedial level, however difference more than 40% is a suspension level.

With ionisation chamber placed in the different positions of a body phantom, a DLP is measured while ionisation chamber is completely inside a drilled hole and all other holes have insertion of the same material as phantom. These 5 different positions are: A (central position), B (position at 12 o'clock), C (position at 3 o'clock), D (position at 6 o'clock) and E (position at 9 o'clock).

For body phantom weighted measured dose length product (DLP_w), computed tomography dose index (CTDI) and weighted computed tomography dose index ($CTDI_w$) were calculated from measured values.

Weighted CTDI was calculated by formula

$$CTDI_w = 1/3CTDI_c + 2/3CTDI_p, \quad (2)$$

where $CTDI_c$ is a CTDI measured value at a central position A, and $CTDI_p$ is a mean measured value of all peripheral positions.

Indicated CTDI and DLP values were registered from the CT display or CT dose protocols. Test results are summed up in table 3.

Table 3. Test results for body phantom.

| Position | Measured DLP, mGy-cm | Measured CTDI, mGy |
|----------|----------------------|--------------------|
| A | 408,3 | 11,84 |
| B | 786,3 | 22,79 |
| C | 729,0 | 21,13 |
| D | 721,1 | 20,90 |
| E | 710,4 | 20,59 |
| DLP_w | 627,2 | |
| $CTDI_w$ | | 18,18 |

For comparing measured results with indicated values different criteria are used. An IEC criteria [12] states that expected (indicated) value and measured value should not differ more than 20%. In this example the difference between indicated and measured results was -4,5%.

CEC [3] reference DLP_w value for routine abdomen examination is 780 mGy-cm and relevant $CTDI_w$ reference value is 35 mGy.

With head phantom the procedure is quite the same as with body phantom, the only difference is that some manufacturers like GE use a head scan protocol that changes dose rate during scan as can be seen in figure 2. Due to the two different scan series (DLP speeds), DLP and CTDI values had to be found for both series individually. The results for the scan are in table 4. Indicated values were also registered and gross DLP_w was constantly 503,34 mGy·cm, $CTDI_{vol}$ for first series was 52,45 mGy, $CTDI_{vol}$ for second series was 20,97 mGy.

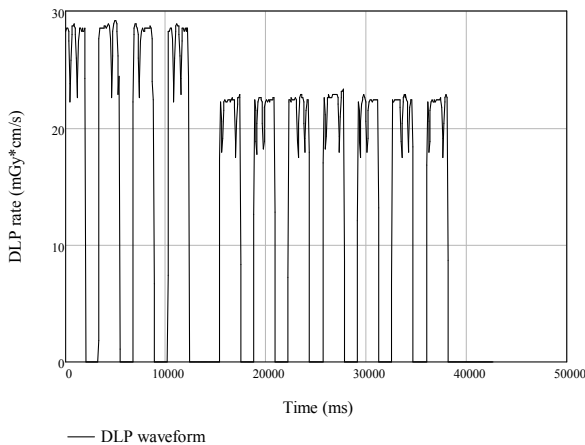


Fig. 2. Measured waveform of the dose length product, using head phantom and standard head protocol, ionisation chamber placed at centre.

Table 4. Test results for head phantom.

| Position | Measured total DLP, mGy·cm | Measured CTDI for 1st series, mGy | Measured CTDI for 2nd series, mGy |
|----------|----------------------------|-----------------------------------|-----------------------------------|
| A | 539,6 | 56,23 | 22,48 |
| B | 508,7 | 53,01 | 21,19 |
| C | 501,7 | 52,28 | 20,90 |
| D | 515,6 | 53,73 | 21,48 |
| E | 521,8 | 54,38 | 21,74 |
| DLP_w | 521,17 | | |
| $CTDI_w$ | | 54,31 | 21,71 |

Test results in table 4 are assessed according to different criteria. IEC [12] states that indicated value and measured values of CTDI should not differ more than 20%. For this example the maximum difference between indicated and measured value was -3,4%. CEC [3] reference DLP_w value for routine head examination is 1050 mGy·cm and $CTDI_w$ reference value is 60 mGy.

3.3 Estimating uncertainty in measurement.

All uncertainties were calculated at 95% confidence level and it was assumed that the phantoms were completely uniform. Standard uncertainty in measurement of uniformity was found by standard uncertainty for peripheral CT-number and standard uncertainty for central CT-number. For the example measurements mentioned above, standard uncertainty was 0,4 HU and expanded uncertainty was 1,0 HU.

For estimating dose measurement uncertainty, air dose measurement data were used. Expanded A-type uncertainty was found as Student coefficient times standard deviation of measured doses. The result was 0,4 mGy·cm. B-type uncertainty of dose measurement corresponds to methodical uncertainty and equipment uncertainty. In figure 3 the measured DLP waveform in air compared to ideal waveform is shown.

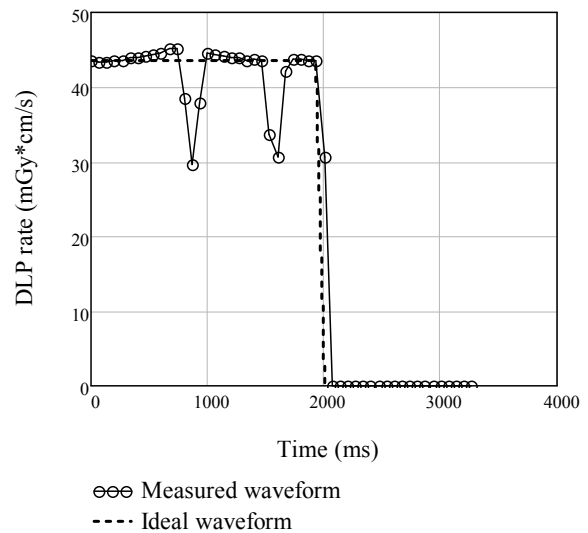


Fig. 3. Measured and ideal waveform of DLP in air.

Absorption notches in figure 3 are caused by wooden stand, which holds phantoms in place at gantry centre. Methodical uncertainty is the difference of the two waveforms in figure 3 and it is found by integrating both functions and finding the relation of two integrals. The difference between two areas is 1,2%, so expanded methodical uncertainty would be 0,97 mGy·cm. As the relative uncertainty of used measuring devices is 4%, the expanded uncertainty of measuring device would be 3,2 mGy·cm. Taking into account A- and B-type uncertainties the total uncertainty in example given above would be 3,4 mGy·cm and relative uncertainty of the test would be 4%.

4. Conclusion

Taking into account radiation safety of patient it is equally important to measure CT dose index (CTDI) and dose length product (DLP) and to assess their constancy, comparing them with base values measured from acceptance tests and with reference doses. Therefore, these tests have been selected as basic quality control tests to be carried out on-site in hospitals. Ununiformity and noise can cause misdiagnosis due to the artefacts. For this reason methods to assess constancy of CT-number, image noise and image uniformity have also been chosen into the selection of tests. The example given above is completely compliant to the relevant standards, but the tests should be repeated in two years.

5. References

1. Brenner J. and Hall E. J., Computed Tomography – An Increasing Source of Radiation Exposure, *The New England Journal of Medicine*, 357, 22, 2277-2284 (2007).
2. European Commission, Council Directive 97/43/Euratom of 30 June 1997 on health protection of individuals against the dangers of ionizing radiation in relation to medical exposure, and repealing Directive 84/466/Euratom, *Official Journal of the European Communities*, L 180 , 22 – 27 (1997).
3. Commission of European Communities (CEC), European guidelines on quality criteria for computed tomography, (European Communities, Luxembourg, 2000).
4. Aavik A., Tartu University Hospital, verbal information.
5. Estonian Ministry of Social Affairs. Statistics. <http://www.sm.ee>
6. Nosach Y., CTDI and DLP measurements in Estonian computed tomography cabinets, Master Thesis (University of Tartu, Tartu, 2006).
7. Nosach Y., Kepler K., Vladimirov A., Implementation of Quality Control Measurement of CT Scanners in Estonian Hospitals, *IFMBE Proceedings*, 11, 1, 2658 - 2662, (2005).
8. Institute of Physics and Engineering in Medicine (IPEM), Report 91: Recommended Standards for the Routine Performance Testing of Diagnostic X-Ray Imaging Systems, (Institute of Physics and Engineering in Medicine, England, 2005).
9. British Institute of Radiology (BIR), Assurance of quality in the diagnostic imaging department, 2nd ed., (British Institute of Radiology, UK, 2001).
10. American Association of Physicists in Medicine (AAPM), AAPM report no. 74: Quality Control in Diagnostic Radiology, (Medical Physics Publishing, Madison, WI, USA, 2002).
11. Nordic Radiation Protection Co-operation (NRPC), No. 7. A Quality Control Programme for Radiodiagnostic Equipment: Acceptance tests, (National Institute of Radiation Hygiene, Herlev, Denmark, 1999).
12. International Electrotechnical Commission (IEC), IEC 61223-3-5, Evaluation and routine testing in medical imaging departments – Part 3 - 5: Acceptance tests - Imaging performance of computed tomography X-ray equipment. (European Committee for Electrotechnical Standardization, Brüssel, 2004)
13. Kalender W. A., *Computer Tomography*, (Publicis Corporate Publishing, Erlangen Germany, 2005).
14. Rasband W., ImageJ 1.38x, <http://rsb.info.nih.gov/ij/>

EVALUATION OF PATIENT DOSES IN CT EXAMINATIONS

Julius ŽILIUKAS*, Leonidas KRYNKE*, Diana ADLIENĖ**

* Radiation Protection Centre, Vilnius, Lithuania;

** Kaunas University of Technology, Kaunas, Lithuania

Abstract: The patient radiation doses from computed tomography (CT) examinations are one of the highest patient doses in diagnostic radiology. Evaluation of dose was done in some CT examinations. The results show that average patient doses for the same type of CT examination performed with different CT scanners may have big variations. The averages of dose length product values for head examination was 715 ± 229 mGy \times cm. The average DLP not exceed the European diagnostic reference levels but for establishment of national DRL require more detail and more wide evaluation.

Keywords: computed tomography, dose index, dose length product, diagnostic reference levels.

1. Introduction

The patient radiation doses from computed tomography (CT) examinations are one of the highest patient doses in diagnostic radiology and have significant influence to collective dose. Comparing with examinations of conventional radiology the CT examinations are not frequent examinations but every years the number of its increase, as number of CT scanners. There were 49 CT scanners for approximately 3.4 million of population at the beginning of 2008 in Lithuania. The two basic principles of radiation protection of the patient as recommended by ICRP are justification of practice and optimization of protection, including the consideration of dose reference levels [1]. There are established national diagnostic reference levels for radiography examinations but for CT examinations not yet in Lithuania. The aim of this work is to measure the computed tomography dose index (CTDI) of different CT scanners, calculate dose length product (DLP) for some most frequent CT examinations and compare it with European dose reference levels for adult patients [2].

2. Methods

For evaluation of radiation doses of different CT scanners the weighted $CTDI_w$ were measured. The measurements were performed using Barracuda Cabinet electrometer and pencil type ionization chamber DCT-10 with 10 cm active volume in length. The 16 cm and 32 cm in diameter respectively head and body phantoms with centre and clock wise four periphery holes were used. The CT scanners were selected randomly different

manufacturers and generations. All CT scanners operating in Lithuania has possibility to display $CTDI_w$ or $CTDI_{vol}$ and some of it additionally shows DLP for preset parameters of selected examination protocol. The measured $CTDI_w$ values were compared with CT scanner displayed values. The measured $CTDI_w$ values were normalized to 100 mAs - $_nCTDI_w$. The normalized $_nCTDI_w$ where appropriate, was compared with ImPACT CT dose calculator $_nCTDI_w$ value. For calculation of DLP, parameters of the standard examination protocols were collected, such as kV, mAs, collimation or slice thickness, number of rotations or number of slices, pitch and etc. From the image archives the scan parameters of patients of the head, lumbar spine and thorax examinations for calculating DLP collected also.

3. Results

The $CTDI_w$ measurements were performed for 15 CT scanners of Esprit, Emotion Duo, Emotion 6, Emotion 16, Balance, Sensation 16, Sensation 40 (Siemens), Mx8000, Brilliance 16 (Philips), Asteon Multi, Aquilion 16 (Toshiba) and HiSpeed CT/e (GE) models used in Lithuanian hospitals. Table 1 show the comparison between measured $CTDI_w$ values and CT scanner displayed for head protocol.

The accuracy of the measured and displayed values is within the 10 % for almost all scanners. For one scanner this inaccuracy was 13 %. According requirements in Lithuania [3] the $CTDI_w$ shall not exceed ± 20 % from the base line values. The same comparison of the measured and displayed values for body protocols

shows that the accuracy is also within 10 % except some cases where values differ up to 14.4 %.

Table 1. Comparison of measured and displayed CTDI_w values for head

| CT scanner | Measured CTDI _w , mGy | Displayed CTDI _w , mGy | Accuracy % |
|---------------|----------------------------------|-----------------------------------|------------|
| Esprit | 53.1 | 51.3 | 3.6 |
| Esprit | 55.3 | 56.7 | -2.4 |
| Emotion Duo | 54.6 | 59.17 | -7.7 |
| Emotion Duo | 56 | 59.17 | -5.4 |
| Emotion 6 | 59.2 | 59.4 | -0.3 |
| Emotion 16 | 24 | 22.3 | 7.5 |
| Sensation 16 | 73.5 | 71.68 | 2.5 |
| Sensation 40 | 52.5 | 52.29 | 0.4 |
| MX8000 | 36.7 | 32.5 | 13 |
| MX8000 | 68.6 | 65.5 | 4.8 |
| Brilliance 16 | 28 | 27.7 | 1.2 |
| Asteon Multi | 116.6 | 121.5 | -4 |
| Aquilion 16 | 51.1 | 56.6 | 9.8 |
| HiSpeed GE | 18.6 | 17.09 | 8.8 |
| Balance | 63.3 | 66.16 | -4.3 |

The measured CTDI_w values were normalized to nCTDI_w values and compared with ImPACT CT dose calculator values. Table 2 show the comparison between nCTDI_w measured and presented by ImPACT.

Table 2. Difference between nCTDI_w values from measured results and presented by ImPACT

| CT scanner | Measured nCTDI _w , mGy/100 mAs | ImPACT nCTDI _w , mGy/100mAs | Differ. % |
|--------------|---|--|-----------|
| Head | | | |
| Emotion Duo | 21 | 21.5 | 2.3 |
| Emotion Duo | 21.5 | 21.8 | 1.4 |
| Balance | 24.3 | 22.9 | -6.1 |
| Emotion 6 | 21.9 | 20.4 | -7.4 |
| Sensation 16 | 23 | 21.3 | -8.0 |
| Sensation 40 | 13.8 | 13.4 | -3.0 |
| MX8000 | 14.7 | 14.1 | -4.3 |
| Asteon Multi | 25.5 | 24.4 | -4.5 |
| Aquilion 16 | 31.1 | 32 | 2.8 |
| Body | | | |
| Emotion Duo | 10.1 | 10.1 | 0.0 |
| Balance | 13.1 | 12.6 | -4.0 |
| Emotion 6 | 10.4 | 10.1 | -3.0 |
| Sensation 16 | 6.3 | 6.8 | 7.4 |
| Sensation 40 | 6.8 | 6.5 | -4.6 |
| MX8000 | 7 | 7 | 0.0 |
| Asteon Multi | 11.4 | 11.5 | 0.9 |
| Aquilion 16 | 49.2 | 46.8 | -5.1 |

The differences between nCTDI_w values are some percents, in some case it fully coincident with presented by ImPACT and the maximum difference is 8 %. From here is possible to see that the measurement was done accurately.

Using the collected parameters of head examination protocols the DLP were calculated or fixed, if DLP were displayed. The difference between examination protocols and DLP values of different CT scanners are

quite different with minimal DLP 223 mGy×cm up to 1400 mGy×cm for standard head examination, usually included scan of base and cerebrum. There are important to mention that quality of image was not evaluated and might be in some cases poor as generation of CT scanners should influent also.

Using the measured CTDI_w values the DLP were calculated also. The calculated values of DLP using measured CTDI_w in some cases were less then displayed in some cases it were higher. It depend on standard examination protocol parameters of different CT scanner manufactures and models like collimation or slice thickness and recommended number of rotations or number of slices and pitch as measured CTDI_w also. The data of DLP displayed on CT scanner and DLP calculated using the measured CTDI_w and calculated averages using data of patients archive are presented in Fig.1.

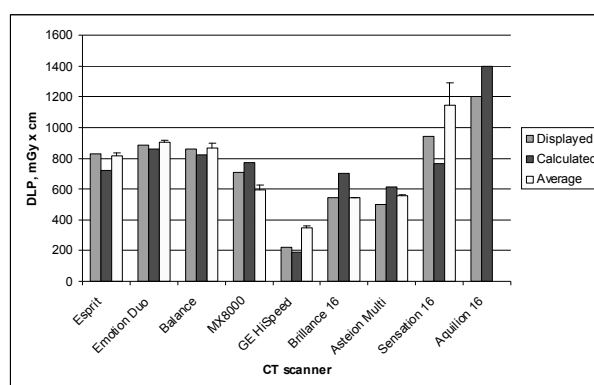


Fig 1. Displayed, calculated and average DLP of the CT head examinations

Additionally were calculated averages DLP of head examinations from different CT scanners using the data of parameters from patients archive and displayed CTDI_w or DLP. The number of patients was from 9 to 25 examined with one CT scanner for head examination. The results show that in almost all real head examinations the DLP are some higher than in examination protocols suggested by manufacture. The average of total head examinations is 715±229 mGy×cm, eliminating lower and higher average DLP.

The evaluation of CT head, spine and thorax examinations were made and averages of DLP were compared with diagnostic reference levels (DRL) of EU.

Table 3. Comparison of DLP values between average evaluated and European DRL

| CT examination | Average of DLP, mGy×cm* | DRL of EU for DLP, mGy×cm |
|----------------|-------------------------|---------------------------|
| Head | 715±229 | 1050 |
| Spine | 389±135 | 780 |
| Thorax | 338±223 | 650 |

* DLP data presented with confidence value of 95 %.

4. Conclusions

The CTDI_w displayed values are different from measured or presented by ImPACT.

For evaluation of patient doses in CT examination $CTDI_w$ should be measured and used for calculation of DLP as evaluation of image quality need especially where average DLP is comparably with average DLP values are low or high.

The average DLP values are less then European DRL but for establishment of national DRL require more detail evaluation of patient doses in CT examination.

5. References

1. European Guidelines on Quality Criteria for Diagnostic Radiographic Images, (Office for Official Publications of the European Communities, Luxembourg, Report EUR 16260, 1996, 80 psl.
2. Quality Criteria for Computed Tomography, (Office for Official Publications of the European Communities, Luxembourg, Report EUR 16262, 1999,107 psl.
3. Lithuanian Hygienic Standard HN 94:2004 „Quality Control in Conventional and Computed Tomography and Mammography Screening. Requirements and Evaluation Criteria”.

STABILITY CHECK OF X-RAY THERAPY UNIT: FROM THE FIFTIES UP TO TO-DAYS USE

Marius LAURIKAITIS*, Povilas GABRALEVIČIUS**

* Oncological Hospital of Kaunas Medical University Hospital, Volungių g. 16, LT- 45434 Kaunas, Lithuania;

** Kaunas University of Technology, Physics Department, Studentų g. 50, LT-51368 Kaunas, Lithuania

Abstract: The aim of this work was to investigate the stability of X-ray therapy apparatus, which is still in use from 1959 and to determine possible deviations from the average values of measurements. It was found that a tolerance of single dose measurements varied in the range of 5%. Stability check for the different operation conditions of the apparatus performed in the series of 10 measurements indicated deviations of the measured values in the range from -4.0 % to 3.2 %.

Keywords: Radiotherapy, superficial X-ray therapy, stability check.

1. Introduction

Kilovoltage X-ray equipment has been widely used in the past. Recently they have been replaced by electrons in most clinical applications. However, kilovoltage X-rays still have a role to play in the range of modalities available in radiotherapy [1].

The performance of a kilovoltage set may differ significantly with the age and type of the equipment and will generally be less than that achieved with megavoltage units. Often the kilovoltage equipment in a hospital is relatively old and therefore may not be equipped with certain safety features, for example a monitor chamber, and may be less reliable [1].

For older kilovoltage equipment calibration constancy checks needs to be made weekly and tolerance needs to be $\pm 5\%$ [1]. The newer X-ray therapy unit's dose stability needs to be checked weekly and tolerance needs to be $\pm 3\%$ [2].

Old superficial X-ray therapy unit RUM-7 has one big disadvantage comparing with the kilovoltage X-ray units used in now-days. Changes of kV and mA have to be performed manually by technicians. Modern equipment performs these changes automatically. Manual increase of kV and mA can cause some errors in the treatment procedure and corresponding doses to the patient.

The aim of this work was to investigate the stability of X-ray therapy apparatus RUM-7 under different operating conditions and to determine occurring deviations from the average value of measurements. The decision whether it is still possible to use this unit for

the treatment of patients or not has been made on the basis of the investigation results.

2. Material and methods

The investigation object was old X-ray therapy apparatus RUM-7, made in 1959 in Soviet Union (Russia) (Fig. 1). The unit generates superficial 40 kV and 10 mA X-rays. Stability tests were performed using 3 cm diameter cone (SSD = 7.5 cm) and 1 mm Al filter (PSS = 0.9 mm Al). Calibrated PTW-UNIDOS weblin electrometer (calibration certificate 2007-10-22), calibrated soft x-ray ionization chamber PTW 23342 (calibration certificate 2007-10-22) and soft X-ray slab phantom were used for the stability tests measurements. Ionization chamber is designed for the detection of low-



Fig. 1. The X-Ray therapy apparatus RUM-7 (1959, Soviet Union).

energy photons from 8 keV to 35 keV with 0.02 cm³ sensitive volume, vented to air. Geometry for dose measurements was set as it is recommended in IAEA TRS-398 dosimetry protocol – Code of practice for low energy kilovoltage X-ray beam [3].

Four different methods were used for stability checks:

1. Collecting of charge during the whole period of irradiation. The electrometer was collecting charge from ionization chamber during one minute (beam on) and was automatically stopped after the time elapsed. After that the procedure was repeated for one minute again. 10 measurements were performed at once and average value was calculated. Few series of measurements were performed per day to evaluate the stability of cold and warm unit. Comparison of measurements was possible since correction for different pressure and temperature conditions were made,
2. Elimination of the “beam on” effect. For the elimination of “beam on” effect X-ray therapy unit was turned on for more then one minute. When according to the unit-timer only one minute was left, the electrometer started to collect charge from ionization chamber. 10 measurements were made at once and average value was calculated. Few series of measurements were performed per day to evaluate the stability of cold and warm unit. Correction for different pressure and temperature were made.
3. Absolute dosimetry measurements. It was determined from absolute dose measurements that 40 sec. time is needed to give 5 Gy dose to the surface of the detector. X-ray unit was turned on for more then 40 sec. When only 40 sec. were left, the electrometer started to collect charge from ionization chamber. Irradiation doses were calculated from the results of measurements. 10 measurements were performed at once and average values were calculated.
4. Dose measurements at real treatment conditions. Irradiation time of 40 sec. was set by technician for the collection of 5 Gy dose. The electrometer collected the charge from ionization camber for 40 sec. and the dose to the detector was calculated. 10 measurements were performed at once and average value was calculated.

3. Results and discussion

The first stability check

This check was performed to find stability of the unit for a long “beam on” period. This method gives real dose rate measurements. Estimated deviations of stability in different measurements and series are presented in Fig. 2. Different series of measurements were checked. Measurements were performed at different conditions: cold and warm unit, different time of the day, different days. Each series consisted of 10 measurements.

It was found that the deviations of single measurements varied in the range of 5 %. The deviations from average value in different series varied from -4.0 % to 3.2 %.

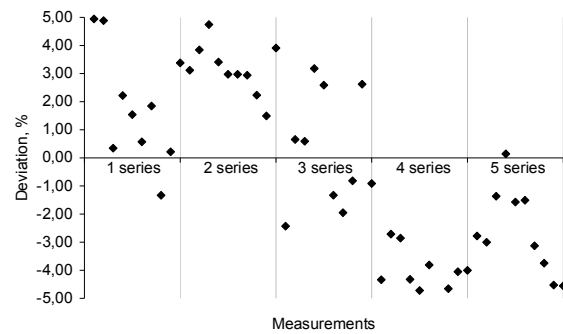


Fig. 2. Deviations from the average value in the first stability check.

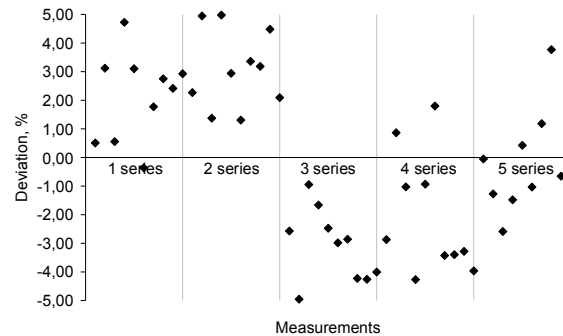


Fig. 3. Deviations from the average value in the second stability check.

The second stability check

This check was performed to find stability of the unit for a short “beam on” period. This method gives information about the stability of mechanical timer. Deviations of stability in different measurements and series are presented in Fig.3. Different series of measurements were checked. It was found that the deviations of a single measurement varied in the range of 5 %. The deviation from average value in different series varied from -3.1 % to 3.1 %.

Comparison of the two first stability checks has not shown big differences in the deviations for single measurements and measurements performed in series. Obtained results support possible use (if necessary) of a mechanical timer in the treatment procedures.

The third stability check

This check is the same as the second one just the time of treatment differs. According to the performed calculations the time needed to give 5 Gy dose is 40 sec. Fig. 4 represents deviations of doses during the different measurements and for different series of measurements. Deviations of doses in single measurements were estimated within 5 % range. The deviations of doses from average value in different series were found in the range of - 2.1 % to 2.1 %.

Comparing the results of the second and the third stability check it could be assumed that there were no changes in deviations for the single measurements and only small changes as compared to the average value for the measurements performed in series. Due to almost

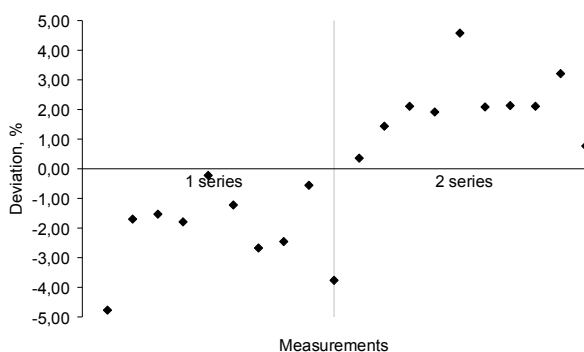


Fig. 4. Deviation of doses in the third stability check

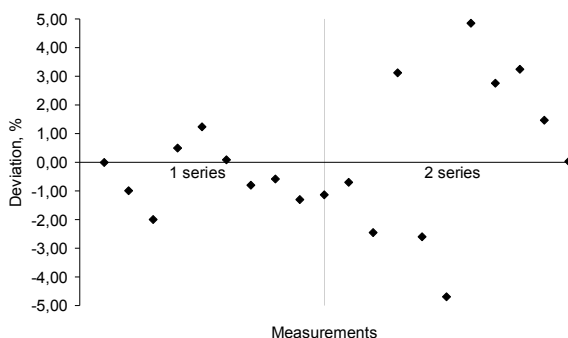


Fig. 5. The deviation of doses in the fourth stability check

the same results, just 2 series (cold one day, warm another day) of measurements were performed.

The fourth stability check

This check was performed under real patient's treatment conditions. The time of 40 sec. necessary to give 5 Gy dose to a patient was set manually by a technician operating the unit. Fig. 5 shows deviations of doses in different measurements and different series. Different

series of measurements were performed on different days when different technicians were operating the unit. The deviations of doses for single measurements were found being from the range of 5 %. The deviations of doses from the average value during the series of measurements varied from -0.5 % to 0.5 %. It was found, that one person was working more stable then the other however tolerance levels ($\pm 5 \%$) were not exceeded in both cases.

4. Conclusion

The old superficial kilovoltage X-ray therapy unit RUM-7 made in 1957 is still in the tolerance range of dose deviations. Despite of the fact, that parameters of the system are fluctuating during the operation of the unit due to a power supply system and generator, big differences in the parameters for cold and warm apparatus and the influence on measurements performed on different days were not found. The highest fluctuations in the treatment doses are attached to the manual changes of kV and mA. However the average deviation in this case is from 0.5 % range.

5. References

1. Ed. by Williams J.R., Thwaites D.I. Radiotherapy Physics in Practice, 1993. p. 95-112.
2. Evans P.A., Moloney A.J., Mountford P.J. Performance assessment of the Gulmay D3300 kilovoltage X-ray therapy unit. The British Journal of Radiology, 74, 2001. p. 537-547.
3. IAEA TRS No. 398. Absorbed Dose Determination in External Beam Radiotherapy. Viena: IAEA, 2000.

INVESTIGATION OF CALIBRATION FACTORS IN NUCLEAR MEDICINE

Eglė SKRIPKAITĖ*, Jurgita LAURIKAITIENĖ**, Gediminas ADLYS*

* Kaunas University of Technology, Studentų g. 50, LT-51368 Kaunas, Lithuania;

** Oncological Hospital of Kaunas Medical University, Volungių g. 16, LT-45434 Kaunas, Lithuania;

Abstract: The main goal in diagnostic examination of patient is to keep a minimum radiation dose to a patient and to get an adequate information for the determination of diagnosis. Due to this reason exact measurements of radionuclide activity in nuclear medicine is necessary. The main instrument for the activity measurement in nuclear medicine is dose calibrator at present time. Accuracy of the dose calibrator can be determined performing quality control tests. In many countries comparable measurements of radiopharmaceutical kit activity are performed in the centres, where they were produced and the results of measurements are sent to the end users. Using the results of measurements accuracy limits of the dose calibrators are set.

Analysis of calibration sources and investigation of the dose calibrators' quality parameters, geometry of measurement, accuracy, dual value estimation, the influence of container on the evaluation of source's activity, which are used for linearity and constancy tests are presented in this work. The results of investigation will be used for the further comparable measurements.

Dose calibrators Atomlab100 and PTW Curiecentor2, ^{137}Cs calibration source, $^{99}\text{Mo}/^{99\text{m}}\text{Tc}$ generator and others materials and equipment available at Oncological Hospital of Kaunas Medical University Hospital, Radiological Diagnostic department were used in this investigation.

Keywords: nuclear medicine, dose calibrator, $^{99\text{m}}\text{Tc}$, ^{137}Cs , quality control tests

1. Introduction

In any application involving the use of ionizing radiation in humans, risks and benefits must be properly evaluated and balanced. For example, in nuclear medicine: radionuclides are used in a variety of diagnostic and therapeutic procedures. Recently, interest has grown for diagnostic agents used for a number of applications in nuclear medicine. This has heightened interest in the need for radiation dose calculations and the use of different dose calibrators for estimation of patients' doses. Consideration of radiation dose in such studies is to minimize the dose to the patient, but to get the best image quality for diagnosis needs. Accurate radioactivity measurements in the clinic are vital for ensuring that administered doses of radiopharmaceuticals are safe and effective. This accuracy is achieved both in the development phase of the drug and in its clinical application, when the instrumentation used is calibrated in a proper way.

Use of radiopharmaceuticals in nuclear medicine. The range of radionuclides used in nuclear medicine has changed over the past decade. So just the most frequently used radionuclide in a Lithuanian hospitals, for diagnostic purposes were investigated.

Medical irradiation represents one of the main sources of exposure of the public to radiation. It is therefore important to measure the activity administered to a patient in vivo as accurately as possible, in order to reduce the received dose to the level, which is necessary, and for which an error could have serious consequences.. Almost as important is the need to ensure that sufficient dose to be effective is administered, thereby reducing the need for repeat treatments.

It is important to point out that in nuclear medicine used radiopharmaceuticals gives possibility to examine externally patient's organism inside processes without pain and other uncomfortable processes to the patient. Doses for the patients are small, so it does not influence the functions of the patient's metabolism. It helps to examine patient's organs functions, what is very useful, because in the most cases functional disorder appears earlier then structural changes of organs.

Comparable investigation. A measure of the potential level of the performance of operational radionuclide calibrators can be determined by conducting comparison exercises by expert and impartial laboratories. Such exercises can have the added advantage of enabling the calibration of particular calibrators to be checked and even determined more accurately. The National Institute of Standards and Technology has maintained a dedicated

program aimed at developing and distributing reference sources and providing calibration services to the nuclear medicine community in North America. The result has been an overall improvement in measurement protocols by isotope producers and radiopharmaceutical manufacturers. The current emphasis of the program is the development of secondary standards that can be used to enable a similar improvement in measurements in the clinic [2]. A regular program of such comparisons has been organized in the United Kingdom by the National Physical Laboratory (NPL) over the past 15 to 20 years, and follow-up workshops have been held for the participants to discuss the results and the potential avenues to performance improvements. The outputs from these comparisons, supplemented by regular dialogue and exchanges of information and experiences between the NPL and the user community, have identified a number of potential, but avoidable, sources of error (Fig.1).

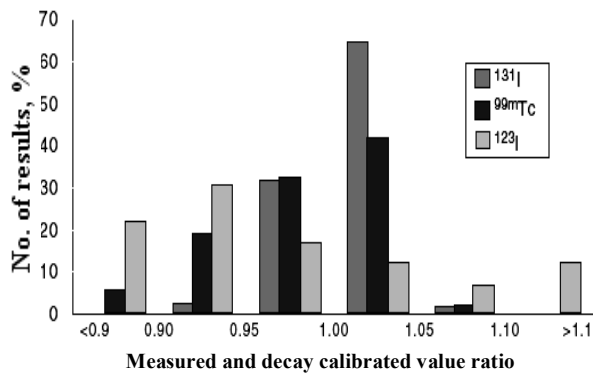


Fig. 1. Comparable results [1].

It is interesting to note that the three comparisons indicate varying levels of performance and, in particular, that there is a significant difference in the overall spread of the results between the three radionuclides. In the two extreme cases, all (100%) the results for ^{131}I lie within $\pm 10\%$ of the true (NPL) value, while for ^{123}I the corresponding figure is only 66%. The results depend on the energy linearity of radionuclides [2]. Knowing that results depends on materials and the wall thickness of dose calibrators, so the effective energy will depend on type of the dose calibrators. The results from comparisons in the Czech Republic [3-4], for example, show a remarkable similarity in spreads of results for both $^{99\text{m}}\text{Tc}$ and ^{131}I , also it was showed that Bqmeters are not so accurate as Curiementors [4] (Fig. 2). The mean values of deviations of measurements of activity in syringes are shifted from those in bottles by about 3–5%. The accuracy performance for diagnostic use should be such as to meet the $\pm 10\%$ criterion. According to this, the accuracy of calibration unit (radionuclide calibrators) can not exceed $\pm 5\%$ [1]. Radionuclide calibrators consisting of a well type ionization chamber and an electrometer are used in nuclear medicine for the determination of the activity of radioactive pharmaceuticals administered to patients. In order to maximize the safety of patients, it is important to ensure the long term accuracy of radionuclide calibrators.

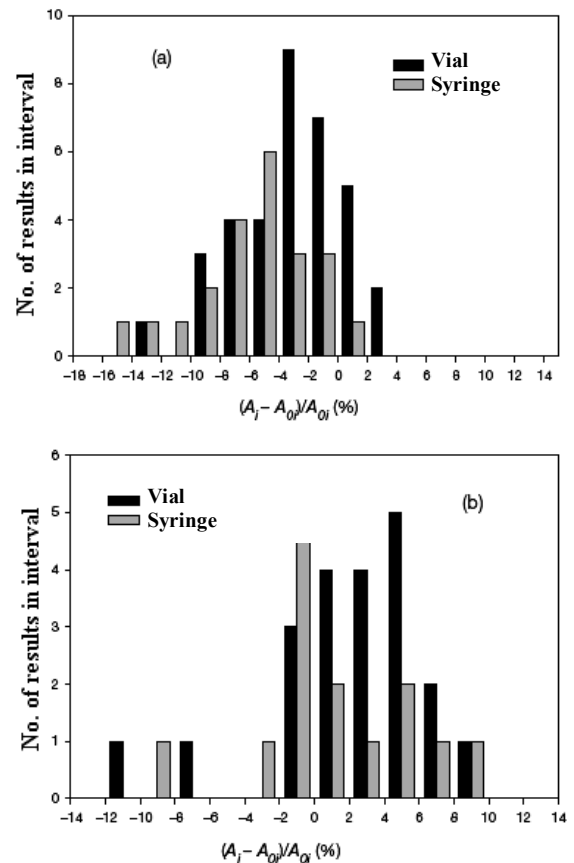


Fig. 2. Distribution of the results of the $^{99\text{m}}\text{Tc}$ comparison. (a) Curiementors. (b) Bqmeters. A_i : activity measured by the participant; A_{0i} : activity measured by the CMI [4].

In this paper calibration sources and dose calibrators' quality parameters, geometry of measurement, accuracy, dual value estimation, container's influence on the evaluation of sources activity for linearity and constancy tests are analyzed. Dose calibrators Atomlab100 and PTW Curiementor2, ^{137}Cs calibration source, $^{99}\text{Mo}/^{99\text{m}}\text{Tc}$ generator and others materials and equipment available at Oncological Hospital of Kaunas Medical University Hospital, Radiological Diagnostic department were used in this investigation

2. Materials and methods

Radionuclides. In this research only γ emitters: $^{99\text{m}}\text{Tc}$, and ^{137}Cs (Fig. 3) were used.

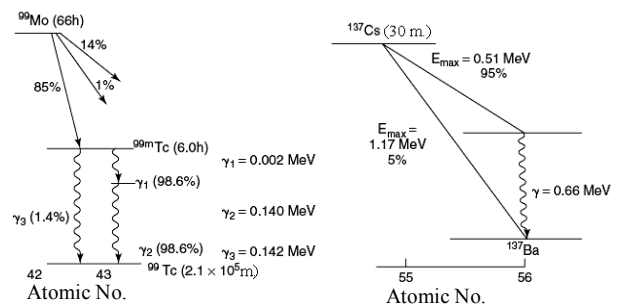


Fig. 3. ^{99}Mo and ^{137}Cs scheme [5].

The main advantage of ^{99m}Tc ($T_{1/2} = 6,007$ h, $E = 140$ keV) is its short half life. Concerning this reason it is widely used for diagnostic purposes. Almost 80 % of all radiopharmaceuticals, used in nuclear medicine is ^{99m}Tc labeled agents. ^{137}Cs ($T_{1/2}=30.17\text{y}$, $E=661.66$ keV) is mostly used as a calibration source [6].

Experimental equipment. Quality control measurements were performed in Radiology Department of Oncological Hospital of Kaunas Medical University, using two different types of dose calibrators.

Activities of the prepared radionuclides were measured using dose calibrators AtomLab100 and Curiementor2 with well-type reference ionising chamber (Fig. 4)

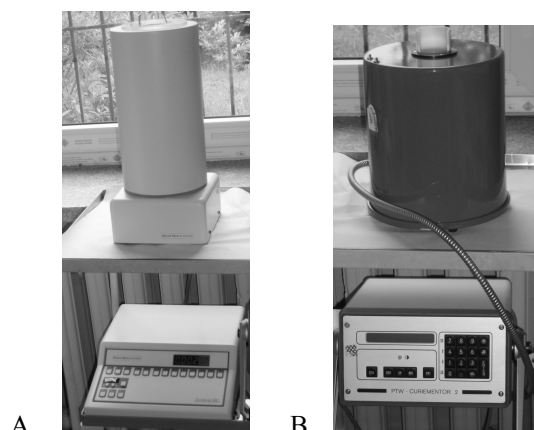


Fig. 4. A-AtomLab100 dose calibrator, B-Curiementor2 dose calibrator.

3. Results and discussion

Different tests were performed using equipment and methods as it is described in previous section.

Geometry test. This test shows dependency of measured activity on the volume and vial type/ geometry (Fig. 5). It was found that the volume correction factor (c_f) for “Syringe” and “Vial” tests varied between $0.95 \div 1.05$. In this case it could be assumed that there is no need for activity corrections concerning the geometry of the syringe, and the vial.

Dual value test. Dual value estimation (DV) test and evaluation of the influence of the source container was splitted into to tests: “Container without a source”, and “Container with a source”.

“Container without a source” test was performed in three steps: 1) measuring the activity of a source in a plastic syringe (PSA1); measuring the activity after the whole

content of the syringe was placed into container (CA) and measuring the activity of the empty syringe (PSA2). Results of measurements are presented in a **Table 1** Re-calculated dual value for this test in the case of dose calibrator AtomLab100 was:

$$CDV = DV \cdot \frac{PSA1 - PSA2}{CA} = 33.6 \cdot \frac{406 - 7.17}{402} = 33.3 \quad (1)$$

In the case of dose calibrator Curiementor2 it was found:

$$CDV = DV \cdot \frac{PSA1 - PSA2}{CA} = 33.6 \cdot \frac{359.3 - 6.7}{348.1} = 34.0 \quad (2)$$

The CDV value given by manufactures for ^{99m}Tc to the syringe gives is 33.6. It means that in daily practice personnel performing activity measurements in a syringe has to change the given value of 33.6 to 33.3 (AtomLab100), and 34.0 (Curiementor2).

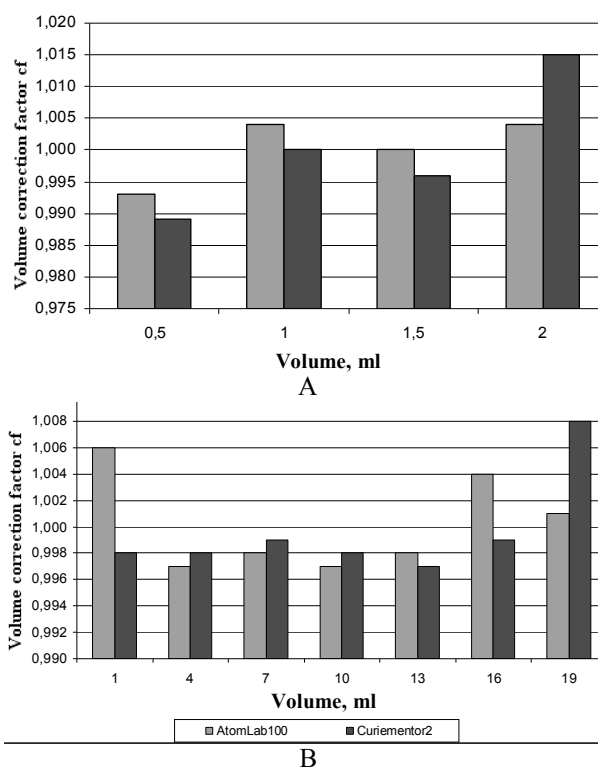


Fig. 5. Dependence of the Volume correction factor on the investigated volumes in: A - „Syringe“ and B - “Vial” tests.

Table 1. „Container without/ with source“ tests results.

| „Container“ without a source | PSA1, MBq | | CA, MBq | | PSA2, MBq | |
|------------------------------|------------|--------------|------------|--------------|--------------|--------------|
| | AtomLab100 | Curiementor2 | AtomLab100 | Curiementor2 | AtomLab100 | Curiementor2 |
| Syringe | 406 | 359,3 | - | - | 7,17 | 6,7 |
| Vial | - | - | 402 | 348,1 | - | - |
| „Container“ with a source | CA1, MBq | | PSA, MBq | | CA2, MBq | |
| | AtomLab100 | Curiementor2 | AtomLab100 | AtomLab100 | Curiementor2 | AtomLab100 |
| Syringe | 401 | 358,6 | - | 401 | 358,6 | - |
| Vial | - | - | 347 | - | - | 347 |

“Container with a source“ test is performed measuring activity of a source in a vial (CA1). After that the whole content of the vial is placed in a syringe, and its activity (PSA) is measured. Empty vial activity (CA2) is measured as well. Results of measurements are presented in a Table 1.

Re-calculated dual value for this test for dose calibrator AtomLab100 was found to be 33.8, and for Curiementor2 - 33.4. In this case personnel has to change given values to those, obtained from recalculations.

Linearity test. This test is performed using a vial with radiopharmaceutical ^{99m}Tc, which activity corresponds to activity used for diagnostic procedures. Measurements are performed periodically each hour during one day.

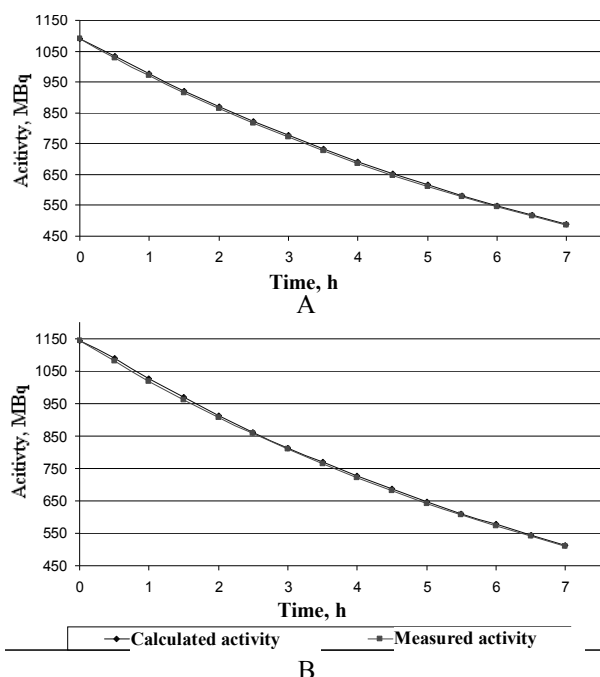


Fig. 6. Time dependence of measured and calculated activity for the dose calibrators: A - Atomlab100 and B - Curiementor2

Activity re-calculations were performed according the equation (3):

$$M_{0,t} = M \cdot (2)^{\frac{t}{T_{1/2}}} \tag{3}$$

here $M_{0,t}$ is re-calculated activity, which is taken as a reference value for the estimation of the calculation uncertainty P:

$$P = \left| \frac{M - M_{0,t}}{M_{0,t}} \right| \cdot 100 \% \tag{4}$$

here M – measured activity.

Table 2. Results of accuracy test

| Date, yy/mm/dd | Decay calibrated, [MBq] | Measured activity, M [MBq] | | Error P, % | |
|----------------|-------------------------|----------------------------|--------------|------------|--------------|
| | | AtomLaB100 | Curiementor2 | AtomLaB100 | Curiementor2 |
| 2008/04/15 | 15.609 | 15.47 | 15.67 | 0.90 | 0.39 |

It was found that the relative error was about 1% and didn't exceed tolerance limit of 3 % (Fig. 6).

Constancy test. This test is a usually made acceptance test of dose calibrator. It has to be performed at least one time before the measurement of patient's dose. Long term radiation source ¹³⁷Cs ($T_{1/2} = 30y.$) is used for this test. Tolerance limits of the activity are: between 14.63 MBq and 16.18 MBq for dose calibrator AtomLaB100, and between 14.74 MBq and 16.30MBq for Curiementor2: (Fig. 7).

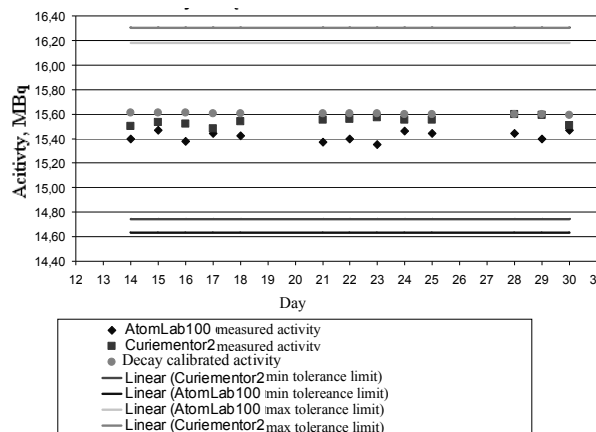


Fig. 7. Tolerance limits for dose calibrators AtomLab100 and Curiementor2

Performed measurements showed, that stability test is adequate to its requirements and do not exceed its tolerance limits.

Accuracy test. Accuracy test was performed using ¹³⁷Cs as a radiation source. Decay calibrated activity was calculated using equation:

$$A = A_0 e^{-\lambda t} \tag{5}$$

where $\lambda = 0.693/T_{1/2}$ Relative error P of the dose calibrators is calculated using Eq.(4). All results are presented in a Table 2.

The estimated error was very small in both cases and additional corrections were not necessary. Using calculations of the accuracy test it is possible to evaluate the changes of the absorbed dose, which is usually determined by accuracy to dose calibrators. ^{99m}Tc and sulfur colloid is usually used for the imaging of the liver, because it very fast localizes in there. It is accepted, that 85 % of the injected ^{99m}Tc is localized in the liver. Dose is calculated according the Eq.6:

$$\bar{D} = A_0 \tau S \tag{6}$$

where A_0 is initial activity at present time, τ , S is a dose corresponding to the accumulative activity unit (Table 3).

Table 3. Dose corresponding to the organ

| Organ | S , rad/ μ Ci·h |
|------------------|-----------------------|
| Large intestinal | $2.5 \cdot 10^{-6}$ |
| Kidney | $3.9 \cdot 10^{-6}$ |
| Liver | $4.6 \cdot 10^{-5}$ |
| Lungs | $2.5 \cdot 10^{-6}$ |

Calculated absorbed doses for liver (target organ), and to other near exposed organs are shown in a Table 4.

The results showed that according to the evaluated errors for dose calibrators, absorbed doses were increased negligible. For example, for the target organ – liver, the dose increases just in 0.07 mGy. For the other organs the maximum absorbed dose increase of 5 μ Gy was observed.

Table 4. Absorbed doses for organs

| Organ \ Absorbed dose | Absorbed dose *, Gy | Absorbed dose **, Gy | Absorbed dose ***, Gy |
|-----------------------|----------------------|----------------------|-----------------------|
| Liver | $7,34 \cdot 10^{-3}$ | $7,41 \cdot 10^{-3}$ | $7,37 \cdot 10^{-3}$ |
| Large intestine | $3,99 \cdot 10^{-4}$ | $4,03 \cdot 10^{-4}$ | $4,01 \cdot 10^{-4}$ |
| Kidney | $6,23 \cdot 10^{-4}$ | $6,28 \cdot 10^{-4}$ | $6,25 \cdot 10^{-4}$ |
| Lungs | $3,99 \cdot 10^{-4}$ | $4,03 \cdot 10^{-4}$ | $4,01 \cdot 10^{-4}$ |

* - absorbed dose, calculated without evaluation of devices percentage errors.

** - absorbed dose, calculated with evaluation of dose calibrator AtomLab100 percentage errors (accuracy test).

*** - absorbed dose, calculated with evaluation of dose calibrator Curiementor2 percentage errors (accuracy test).

4. Conclusions

1. Geometry test showed that correction factors of dose calibrators slightly differ, however remain between $0,989 \div 1,015$ for Curiementor2; and $0,993 \div 1,006$ for AtomLab100.

2. Estimated deviation from the reference dual value of container (CDV) was: for the vial type container - 0.89% for AtomLab100, and 1.19 % for Curiementor2:

for the syringe type - 0.60 % for both dose calibrator AtomLab100, and for Curiementor2.

3. Relative Error of the linearity test measurements did not exceed 1 % tolerance for both type calibrators.

4. Results of the accuracy test indicated only small deviations of the decay calculated activity: 0.39 % for Curiementor2 and 0.89 % for AtomLab100.

5. Relative uncertainty of the calculated absorbed doses was negligible for the liver as a target organ. The change of 0.07 mGy was observed for the liver as compared to the total absorbed dose of 7.34mGy.

5. References

1. Woods M.J, Baker M. Performance and quality control of radionuclide calibrators in nuclear medicine // Standards and codes of practice in medical radiation dosimetry – Vol. 2, (2003), p. 45-57. ISBN 92-0-111403-6.
2. Stabin M.G. Radiation dose assessment in nuclear medicine // Standards and codes of practice in medical radiation dosimetry – Vol. 2, (2003), p. 3-15. ISBN 92-0-111403-6.
3. Zimmerman B. E. Quality assurance programmes for radioactivity measurements in nuclear medicine // Standards and codes of practice in medical radiation dosimetry – Vol. 2, (2003), p. 17-27. ISBN 92-0-111403-6.
4. Olšovcová V. Activity measurements with radionuclide calibrators in the Czech Republic // Applied Radiation and Isotopes. – Vol. 60, No. 2-4, (2004), p. 535-538.
5. Kim J. H. An axis of rotation alignment system for high-resolution pinhole / Kim J. H., Lee J. S., Park M. J., Lee W. W., Kim S. M., Kim Y. K., Kim S. E., Lee D. S. // Nuclear Instruments and Methods in Physics Research Section A: Accelerators, Spectrometers, Detectors and Associated Equipment. – Vol. 589, No. 2 (2008), p. 338-344.
6. Podgorsak E.B. Radiation oncology physics: a handbook for teachers and students // International Atomic Energy Agency, Vienna (2005), p. 16-21, 77-81.

LIGHT RADIATION PARAMETERS OF HIGH INTENSITY USUAL LIGHT EMITTING DIODES

Virgilijus MINIALGA*

* Department of Physics, Kaunas University of Technology, Kaunas, Lithuania

Abstract: Solid state light sources become usual sources for public and home illumination. Big funds are assigned for investigations and production industry in solid state illumination because of comparatively high efficiency and long usage time.

For medical purposes these light sources will be used too. Several characteristics of several high intensity light emitting diodes are presented: intensity distribution and spectra. Light coherence length is evaluated for monochromatic light.

Keywords: LED, high intensity light, spectrum of light, light intensity distribution.

1. Introduction

High intensity solid state illumination devices are light emitting diodes (LED's) [1] and lasers. Semiconductor lasers usually are constructed in diode form (laser diodes – LD). They are very monochromatic sources and it is difficult to change wavelength of optical illumination.

For spectral investigations in medical applications wide spectrum light is necessary in some cases. Light emitting diodes can be used as alternative light sources. The intensity distribution in different directions and spectrum of radiation should be known.

2. Experimental setup

The intensity distribution in different directions was measured in 1m distance from LED. Calibrated photodiode was used for intensity measurements

The Horiba-Jobin Yvon spectrometer was used for spectrum of emitted light investigation. It was measured in 1m distance from LED in different directions from LED axis. The fiber optic input was used in this spectrometer. Diagram of experimental setup for spectrum distribution at different angles is presented in Fig.1. The input light was collected using optical fiber. This means that dimensions of point of measurement are approximately small parts of millimetres. Therefore high spatial resolution can be achieved.

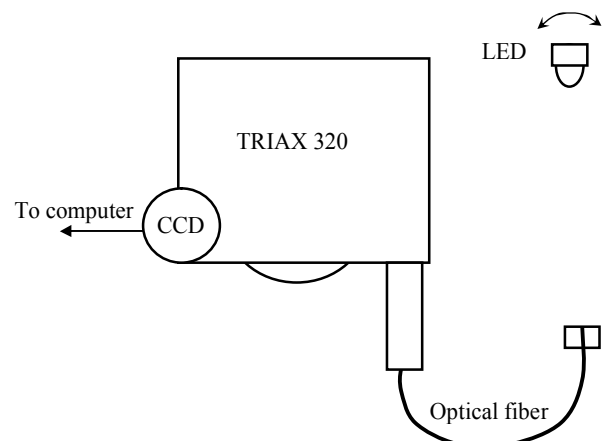


Fig. 1. Experimental setup for spectral investigations of emission of LED's; light source can be rotated around axes going through centre of diode

3. Experimental results

Several LED's were investigated in experiments. LED's of white light were of two types: cool light and warm light. Spectrum of cool light is shifted to blue side of spectrum and spectrum more red components are presented in warm light.

Spectra distribution in the centre of light cone and on the side of light cone of different LED's are presented in figures 2-7. The coherence length was calculated for colored sources for main visible line. Possibility of interferometric measurements can be evaluated using coherence length.

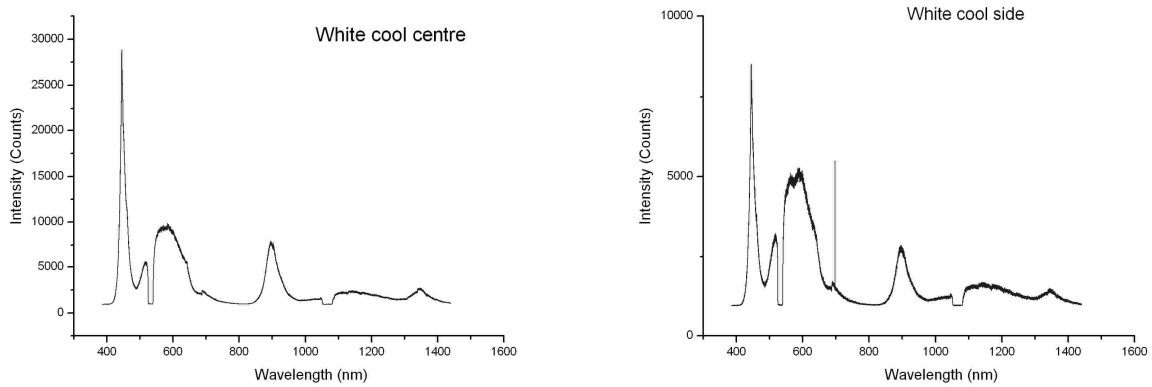


Fig. 2. Spectrum of white cool light in the centre (a) and on the side (b) of the light cone; the blue line is of comparatively high intensity

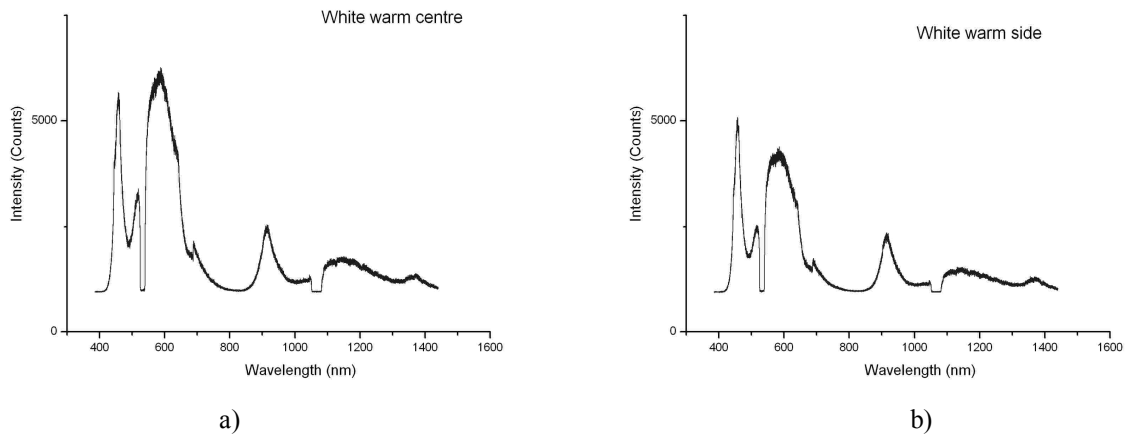


Fig. 3. Spectrum of white warm light in the centre (a) and on the side (b) of the light cone; the red band is of comparatively high intensity

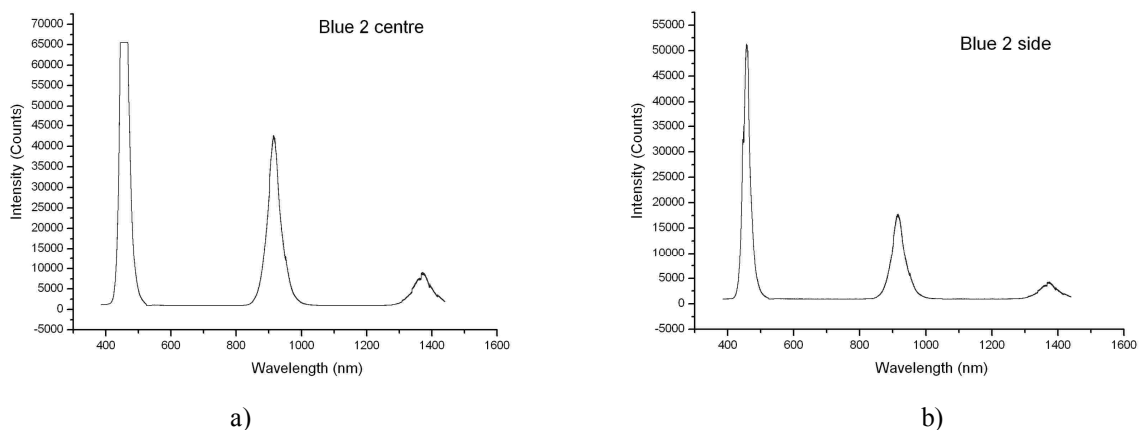


Fig. 4. Spectrum of blue light LED in the centre (a) and on the side (b) of the light cone; intensity of lines decreases on the side of light cone; coherence length evaluated for blue line is about $6 \mu\text{m}$

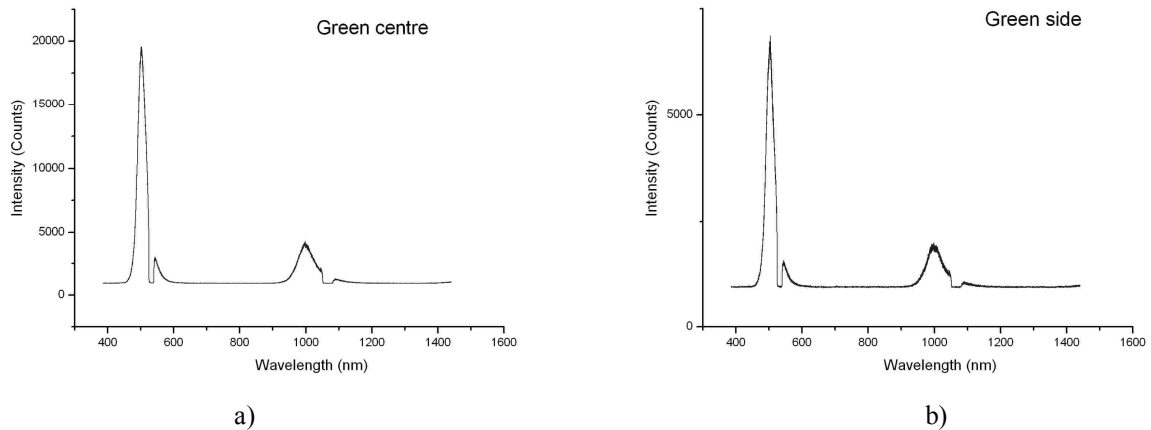


Fig. 5. Spectrum of green light LED in the centre (a) and on the side (b) of the light cone; intensity of lines decreases on the side of light cone; coherence length evaluated for green line is about $7 \mu\text{m}$

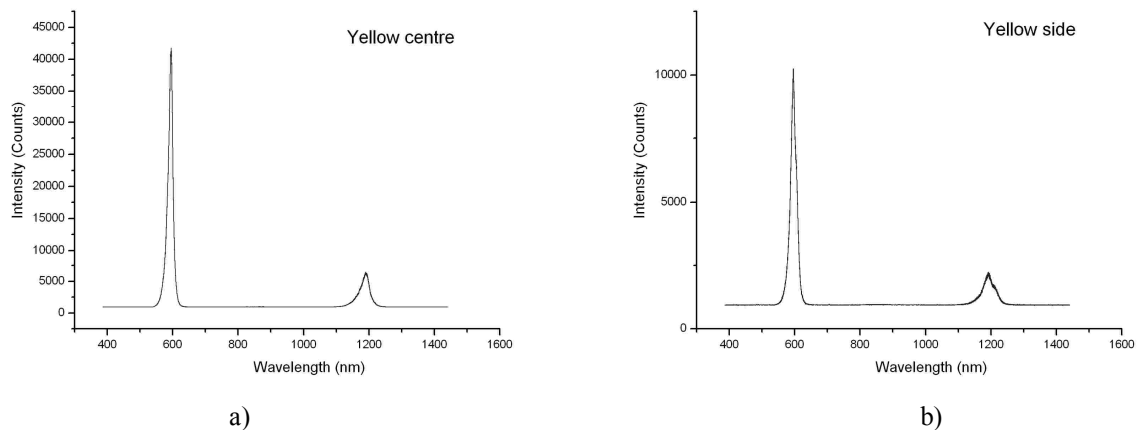


Fig. 6. Spectrum of yellow light LED in the centre (a) and on the side (b) of the light cone; intensity of lines decreases on the side of light cone; coherence length evaluated for yellow line is about $17 \mu\text{m}$

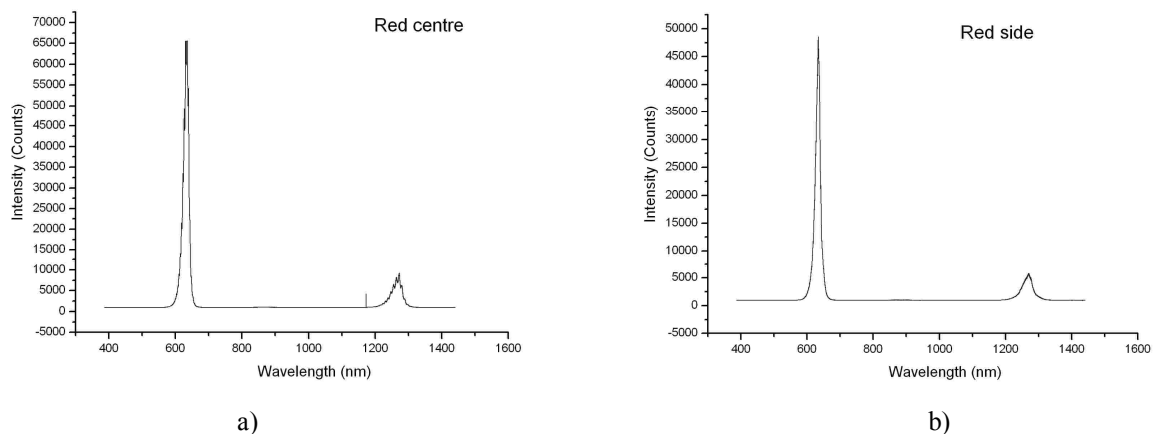


Fig. 6. Spectrum of red light LED in the centre (a) and on the side (b) of the light cone; intensity of lines decreases on the side of light cone; coherence length evaluated for red line is about $23 \mu\text{m}$

4. Conclusions

White light LED's are of two types: cool white light and warm white light. According to obtained spectra in cool white light spectra bands of blue side of spectrum is of higher intensity and in warm white light spectra bands of red side of spectrum is of higher intensity. Spectrum of light in the centre of light cone differs from spectrum

of light in the side of light cone. Angular position of LED is important in applications.

LED sources of comparatively monochromatic light show several bands in infrared region. If photo-receiver is sensitive to this part of spectrum the errors from infrared illumination can arrive. The coherence lengths are comparatively short in estimations for lines of highest intensity.

These peculiarities should be taken into account in construction of optical equipment for measurements using LED's.

5. References

1. Artūras Žukauskas, Michael S. Shur, Remis Gaska, Introduction to Solid-State Lighting, John Wiley & Sons, 2002. 224 p.

ACHIEVEMENTS ON PATIENT'S DOSE MEASUREMENTS DURING MAMMOGRAPHY SCREENING EXAMINATIONS: RESULTS AND PROBLEMS

Inga CIBULSKAITĖ^{**}, Diana ADLIENĖ^{*}, Jurgita LAURIKAITIENĖ^{***}, Marius LAURIKAITIS^{**},
Miglė ŠNIUREVIČIŪTĖ^{***}, Aušra URBONIENĖ^{***}, Birutė GRICIENĖ^{***}

^{*} Kaunas University of Technology, Kaunas, Lithuania;

^{**} Kaunas Medical University Hospital, Kaunas, Lithuania;

^{***} Radiation Protection Centre, Vilnius, Lithuania

Abstract: The results of three year experience on patient dose measurements during actual screening mammography examinations are presented in this paper. Determination of the 2.4 mGy average glandular dose reference level for mammography screening procedure in Lithuania is proposed.

Keywords: mammography, reference level, average glandular dose.

1. Introduction

Breast cancer still remains the most often oncological disease among women. The preventive breast cancer mammography screening programs helps in detection of the breast cancer in the early stage and so to prevent women against fatal outcome of this disease. National mammography screening program has been started in September 2005. Mammography screening program is addressed to the women in the age of 50-69 years. According to the screening protocol for mammography, X-ray exposures (Crano-Caudal (CC) projection and Medio-Lateral-Oblique (MLO) projection for each breast of the patient) are planned. Two independent radiologists-reviewers evaluate mammograms according to the standard BI-RADS evaluation system. The dose obtained during screening mammography procedure is especially important as it could be performed for possible healthy tissue. In all cases radiation dose to a patient should not exceed the reference level during radiological examinations.

There was a lack of information about doses received by woman during screening mammography examinations in Lithuania. Another very important question was: does the reference level adopted from the European guidelines is suitable for Lithuanian practice?

Due to these reasons, an investigation of patient's doses during mammography examinations in Lithuania was performed parallel to the National mammography screening program.

The aim of this work was to compare the results obtained in previous years investigating patient's doses during mammography screening examinations and to

propose the reference level for the average glandular dose for mammography screening examinations in Lithuania.

2. Instruments and methods

The dose to the breast of an individual patient depends on the characteristics of the equipment being used for the examination; technological factors, selected for the examination (X-ray tube voltage, X-ray tube output, anode/filter combination, X-ray attenuation, film/screen system, focal spot to the target distance, compression force); size and density of the patient's breast. Dosimetry method used for the measurements and estimation of the possible impact of human factor to the performed measurements are of great importance too.

Investigation of patients doses during mammography examinations were performed in 15 health care institutions in Lithuania: S.Kudirka Hospital (Alytus), Clinic "Bendrosios medicinos praktika" (Kaunas), Dainava Outpatient department (Kaunas), Kaunas Medical University Hospital, Division of the Kaunas Medical University Hospital Oncology Hospital, Dainava Outpatient Department (Kaunas), Šančiai Outpatient Department (Kaunas), Klaipėda University Hospital, Marijampolė Hospital, Panevėžys Hospital, Salvija medical centre (Kaunas), Šiauliai Hospital, Utena Health Care Centre, Antakalnis Outpatient Department (Vilnius), Centre Outpatient Department (Vilnius), Vilnius University Oncology Institute. Randomly selected groups consisting of 10-20 patients of different age and with different breast density and size were chosen for the investigation in each

institution. Mammography units “ALPHA RT” (Instrumentarium), “MAMMOMAT 100” (Siemens) or “MAMMO DIAGNOST U-M”, “PHILIPS MAMMO DIAGNOST” with a grid, Mo/Mo or Mo/Rh anode / filter combination; Kodak Min-RD, Cawo Mammo R200 film cassettes and Kodak X-Omat, Konica Minolta, CEA films were used for the screening procedures. Exposure parameters were registered for each patient together with the values of the compression force and the compressed breast thickness, age of the patient and other individual data. Entrance surface doses to patients breast were measured using LiF:Mg,Ti TLD dosimeters: pellets with a size of (3.2x3.2x0.9) mm³, calibrated and read out using a Harshaw TLD5500 (Harshaw Bicon Radiation measurement products, Ohio, US) at the Department of Medical Radiation Physics at Malmö University Hospital and tablets of ø5mm, which were calibrated at the SSL in Latvia and read out using Rados TLD system at Lithuanian Radiation Protection Centre. Depending on the type of the investigation, one to four dosimeters were placed on the breast surface at the reference point (central position, upper quadrant of the breast, 5-6 cm distance from the chest wall).

Average glandular dose (AGD), which is the main dosimetrical parameter in mammography examinations, expresses the dose absorbed in the patient’s breast tissue and is described as:

$$AGD = ESAKgc \tag{1}$$

ESAK is entrance surface air kerma; *g* is entrance air kerma to mean glandular dose conversion factor (corresponds to a breast glandularity of 50%); *c* is correction factor for any difference in breast composition from 50% glandularity; *s* is correction factor for different X-ray spectra.

The value of entrance surface air kerma (*ESAK*) could be obtained dividing the value of measured entrance surface dose (*ESD*) by backscattering factor, *B*, which corresponds to the dosimeter used (European protocol on dosimetry in mammography. EUR 16263EN):

$$ESD = B * ESAK \tag{2}$$

Approximately 270 patients have been examined and exposure doses to the patient’s breast during mammography examinations have been investigated.



Fig. 1. Front page of the database

3. Results

Results of measurements were included into database *MAMOLIT*. This database was created for the monitoring of patient doses received during mammography examinations in Lithuania (Fig.1).

The individual data of mammography patients, a date of mammography examination, health care institution, where the examination has been performed, equipment, which was used, technical and technological parameters of the exposure, are included into database together with the values of measured entrance surface doses, values of the necessary conversion factors, and the name of the person, who has performed dose measurements of patient. Database *MAMOLIT* calculates average glandular dose (AGD) for each patient and presents dose distributions in one institution or compares doses in different institutions. Patient’s dose distributions in two health institutions versus compressed breast thickness are presented in Fig 2 and Fig 3.

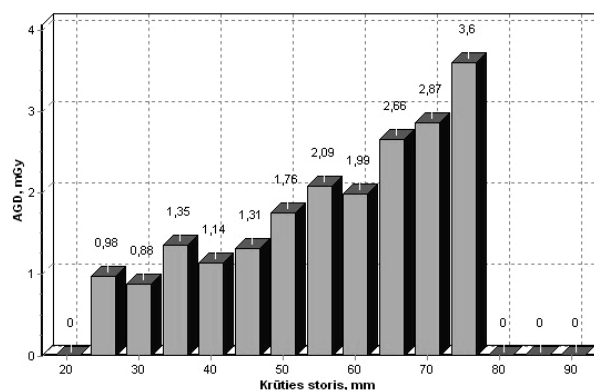


Fig. 2. Patient’s dose distributions versus compressed breast thickness in one of the health institutions

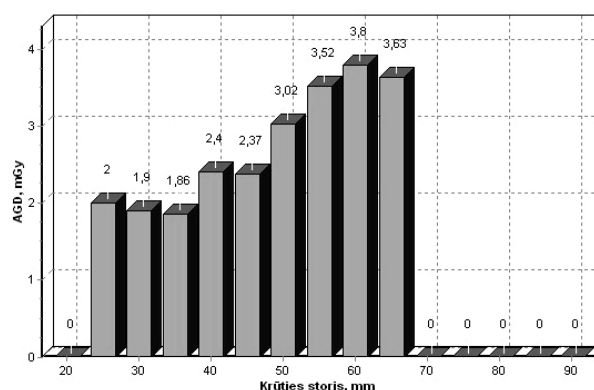


Fig. 3. Patient’s dose distributions versus compressed breast thickness in another health institution

Due to some reasons, that were not analysed broadly, there are some variation of the AGD from institution to institution (Fig 4). However in the bigger part of the institutions, average glandular doses for the particular compressed breast thicknesses are within the acceptable levels, stated in the Table 1 [2]. These levels were evaluated during phantom measurements and are mostly used for the quality control measurements of the mammography system.

Table 1. Maximum average glandular dose per PMMA thickness [1].

| Thickness of PMMA, cm | Equivalent breast thickness, cm | AGD _{max} to equivalent breasts, mGy |
|-----------------------|---------------------------------|---|
| 2 | 2.1 | < 1.0 |
| 3 | 3.2 | < 1.5 |
| 4 | 4.5 | < 2.0 |
| 4.5 | 5.3 | < 2.5 |
| 5 | 6.0 | < 3.0 |
| 6 | 7.5 | < 4.5 |
| 7 | 9.0 | < 6.5 |

The primary idea of patient’s dose measurements during mammography examinations was setting of the national dose reference levels in Lithuania and in each health care institution separately. Due to this reason the values of average glandular dose for a “standard” 55 mm compressed breast thickness (as for Lithuania), estimated in different hospitals were compared. According to the results of measurements national reference level of 2,4 mGy with the certainty of the third quartile was proposed for the average glandular dose absorbed in the patient’s breast during mammography screening examination. The level of 2,4 mGy is well promising result, since it means possible reduction of the existing 3 mGy reference level, which is defined in [3].

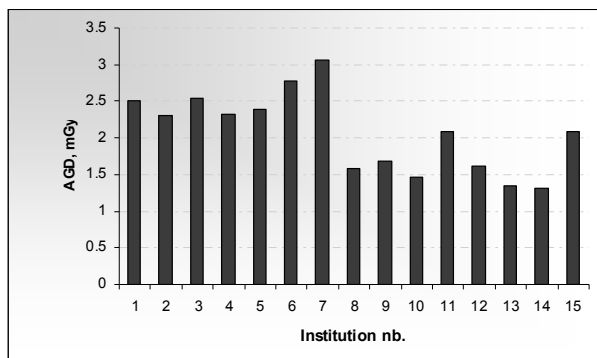


Fig.4. AGD for 55 mm thickness breast in different health institutions

The measurements in the most of the health care institutions were repeated in 2008. Comparison of the results states some decrease of the average glandular dose in the same health care institution (Fig.5 and Fig.6).

The improvement of the results have been achieved after regular quality control program was introduced and optimization of mammography screening procedure was performed.

Dose reference level is determined for only one exposure during mammography examinations. However it is to point out, that the total entrance surface dose at the point of measurement is more than twice higher during the whole screening procedure (4 exposures) as compared to one single exposure dose (Fig.7). It means that attention should be paid and optimization undertaken when performing complex mammography screening procedure

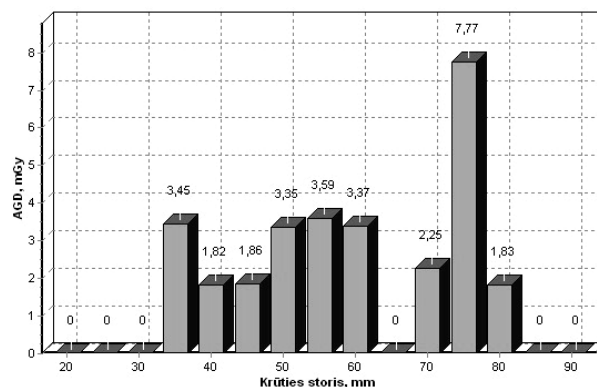


Fig.5. AGD versus compressed breast thickness in one of health care institutions in 2006

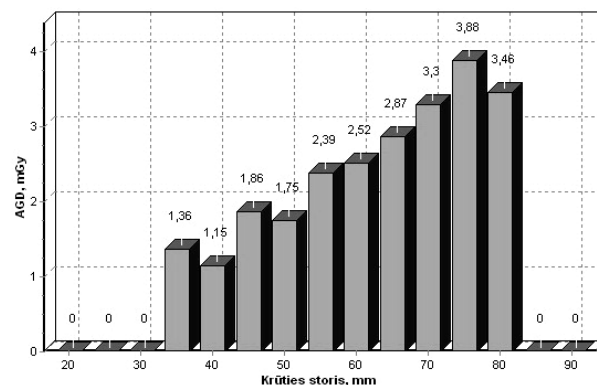


Fig.6. AGD versus compressed breast thickness in the same health care institution in 2008

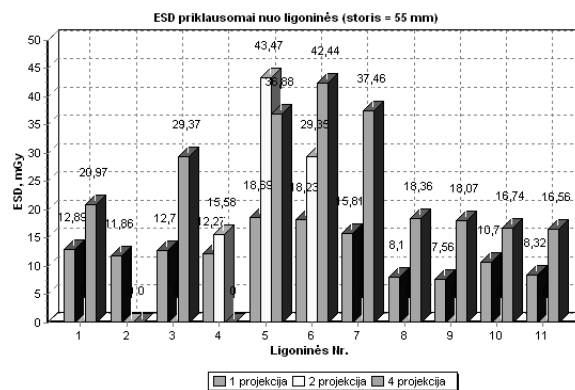


Fig.7. ESD distribution versus compressed breast thickness in one of health care institutions (1 and 4 exposures)

4. Summary

Average glandular dose to the patient’s breast obtained during mammography screening examination was estimated from the results of the entrance surface dose measurements with TLD dosimeters in 15 health institutions of Lithuania. In most of health care institutions dose measurements were performed repeatedly in 2008. All results of measurements together with other important data were included into data base **MAMOLIT** which allows to follow up dose levels in one separate health care institution and to compare the results obtained in different institutions.

National reference level of 2.4 mGy per exposure with the certainty of the third quartile for average glandular dose for mammography screening procedure was proposed.

Attention should be paid for the entrance surface dose at the point of measurement during the complex mammography screening examination, since measured values of ESD are more than 2 times higher than those obtained from one single exposure measurements

5. References

1. European protocol on dosimetry in mammography. EUR 16263EN. ISBN 92-827-7289-6. Luxemburg.
2. European guidelines for quality assurance in breast cancer screening and diagnosis. Fourth edition. European Commission. 2006.
3. Radiacinės saugos centro įsakymas. 2004 m. lapkričio 22 d. įsakymas Nr. 55 „Dėl Rekomenduojamų rentgeno diagnostikos apšvitos lygių“ (Žin., 2004, Nr. 172-6372).

THE ROLE OF THE INDEPENDENT DOSE CALCULATION ALGORITHM FOR CHECKING OF DOSE PLANS

Miglė ŠNIUREVIČIŪTĖ^{**}, Marius LAURIKAITIS^{***}, Jurgita LAURIKAITIENĖ^{***}, Tatjana ZAKREVSKAJA^{***},
Gediminas-Antanas ADLYS^{*}, Saulius RAILA^{*}, Diana ADLIENĖ^{*}

^{*} Kaunas University of Technology, Kaunas, Lithuania

^{**} Kaunas Medical University Hospital, Kaunas, Lithuania

^{***} Oncological Hospital of Kaunas Medical University Hospital, Kaunas, Lithuania

Abstract: The use of the new modern radiotherapy equipment does not exclude the requirement to deliver the prescribed dose to the patient. Despite of the fact that nearly all radiotherapy treatment procedures are computerized the errors may occur. If the deviation from the prescribed dose to the tumor is larger than 5%, it may influence the clinical outcome of the treatment. This may be prevented if dose plans are checked before the treatment using an independent dose calculation algorithm, which uses different input data than treatment planning system algorithms.

An independent dose calculation algorithm was developed and dose calculation program “Radiotherapy verification program 2008” was created for the case when medical linear accelerator is used for the treatment of cancer patients. Dose calculation model is based on the attenuation and scattering of the X-ray photons ion in biological tissue. Model includes application of the irradiation parameters determined during clinical measurements; Monte Carlo modeling results and results of the investigation performed using different dosimetry methods.

The aim of this work was to investigate possible optimization of dose planning performed for the patient’s treatment with high energy photons in linear accelerator.

The independent dose calculation algorithm was implemented for checking of dose plans prepared for the treatment of patients in linear accelerator CLINAC 2100D/C using 3D planning system ECLIPSE. Absolute dosimetry measurements were performed using ionization chamber PTW 31003 and PTW UNIDOS 10001 system; relative dosimetry measurements— using electrometer MULTIDOS and PTW ionization chamber (estimation of the irradiation dose, checking of the calibration and calculation doses, estimation of half value layer). Comparison of dose plans prepared using standard treatment planning system and plans established using independent dose calculation algorithm for two locations was performed. It was found, that in the case of breast cancer treatment with 6MeV photons deviations between planned and calculated dose varied from 3,0% to 7,9% and in the case of larynx – from 2,6% to 7,8%. Relative high deviations can be attributed to the fact that developed independent dose calculation algorithm is based on the evaluation of the interaction caused by monoenergetic photons. Spectral distribution of the photons generated in linear accelerator influences photon interaction processes with biological tissue additionally. More detailed investigation of the dynamical parameters of the irradiation field and inclusion of this information into dynamical dose calculation model would be of great advantage developing multifunctional dose calculation models, adopted for the optimization of dose plans in the case of linear accelerator as it is required by official EU institutions.

Obtained results of calculations are discussed in accordance with measured physical parameters and will be used for the optimization of the dose verification algorithm.

This work is supported by Lithuanian State Science and Studies Foundation.

Keywords: radiotherapy, dose planning, independent dose calculation algorithm

AUTHOR INDEX

- Adlienė D. 8, 19, 68, 83, 98, 102
Adlys G.A. 45, 89, 102
Andrijaitienė V. 68
Bagdonas S. 12, 15
Cibulskaitė I. 98
Čiburys A. 12
Dehtjars J. 27, 64
Druteikienė R. 41
Gabralevičius P. 86
Gadonas R. 12
Gricienė B. 98
Guobienė A. 19
Janutytė I. 15
Jašinskas V. 22
Johansson L. 52
Karabanovas V. 15
Kaškelytė D. 12
Katasevs A. 60
Kepler J. 78
Kepler K. 73, 78
Krynke L. 83
Kulvietis V. 15
Laurikaitienė J. 19, 89, 98, 102
Laurikaitis M. 86, 98, 102
Leide-Svegborn S. 49
Lukšienė B. 41
Mattsson S. 8, 49
Meijers A. 60, 64
Mikšys D. 72
Miller A. 64
Minialga V. 94
Nyström H. 56
Plaude S. 64
Poderys V. 22
Poļaka N. 27
Popov S. 60, 64
Prosyčėvas I. 19
Pruul I. 73
Puišo J. 19
Punys V. 32
Raila S. 102
Reisfeld R. 27
Romanova M. 27
Rotomskis R. 12, 15, 22
Saraidarov T. 27
Skripkaitė E. 89
Söderberg M. 49
Stenström K. 36
Streckytė G. 12
Sydoff M. 49
Sudnikovičs A. 27
Šniurevičiūtė M. 98, 102
Uusijärvi H. 49
Urbonienė A. 98
Vladimirov A. 73
Zakrevskaja T. 102
Zikas M. 32
Žemaitienė R. 22
Žiliukas J. 83

Instruction for the preparation of final papers for the conference proceedings

Only original works, nowhere else published before, dealing with the conference topics and prepared in compliance with the enclosed requirements will be accepted for the conference.

The paper must be written in English. The written material of the article should be prepared on a paper of A4 size using Microsoft Word for Windows text editor. The length of the paper must be of 4 or 6 pages.

The paper must be written in two columns in **Times New Roman fonts, single spacing and with no indentations**.

Margins on the first page are as follows: left, right and bottom margins – 2 cm, top margin – 6 cm wide. All **margins on the second and subsequent pages** are 2 cm wide.

On the first page title of paper ought to be placed at the distance of 6 cm from the top edge of the page. The title should be written in bold capital letters using Times New Roman 13-point font, single spacing and centered in the whole width of the page. Below the title there should be 2 empty, 10-point lines left.

In lines that follow in order the names of the authors and institutions are written (surname in capitals) using 10-point font with single spacing. Next, there are again 3 empty lines of a 10-point height.

Below, the actual text of the paper begins. The text is written in two columns with the space of 1 cm between them, using Times New Roman 10-point font, single spacing. The text should begin with an abstract (the word 'Abstract' written in 10-point bold italics) of a scope of not more than 10 lines (10-point font also). The abstract section is followed by keywords section written in the same way.

Titles of chapters should be written in 10-point bold type font with single spacing. They should be numbered by successive Arabic figures and centered in lines. **Titles of subsections** are to be written in 10-point bold type font with single-spacing as well, but they should be aligned with the left edge of the column. All titles are to be separated from the text by 1 (10-point) empty line above, and 1 (6-point) empty line below the title.

Contents of chapters and subsections must be aligned with both edges of each column without any additional spacing between lines.

Drawings, diagrams and photographs are to be considered as the same and referred to using abbreviations, for instance 'Fig.' and marked as Fig. along with the successive number. The drawings may be prepared by using of any technique (as black lines on a white background) and photographs must be black-and-white only. Captions of figures are to be written in 9-point font, single spacing. The font size on the figures should ensure them a good legibility. The space between figure and its caption should have the size of 6-point font. Above each figure and below its caption should be 1 empty line spacing (10-point).

Tables ought to be numbered by Arabic figures and referred to by the word, for instance: Table 1. The headings informing about the contents of tables should begin with the word 'Table' followed by the successive number and ought to be written in 9-point font and shifted towards the left margin. The heading should be separated from the table by 1, 6-point empty line.

Figures and tables should be not more than 8 cm wide and ought to be centered in column. In particular cases it is allowed to insert figures or tables that require the full width of page (maximum 17 cm). In such cases they should be centered on the full width of page together with captions or headings.

Mathematical equations ought to be centrally arranged in lines and numbered by successive Arabic figures using parentheses aligned with the right-side edge of the column. Symbols and variables in equations as well as in the text should be written in italics, while vectors and matrices in ordinary bold type. Equations ought to be separated from the text by 1 empty line (10-point).

After the actual text, the article should contain **references and sources** from which the information has been taken. The references must be numbered successively by Arabic figures and referred to in the text by these numbers in square brackets, for instance: [2]. Each successive reference should be written with single spacing and an incision of 0.5 cm in every successive line.

The enclosed **example of paper** provides the general arrangement and the main requirements for preparing the manuscript.

**TITLE OF PAPER WRITTEN IN BOLD CAPITAL LETTERS USING
13-POINT FONT, WITH SINGLE SPACING AND CENTERED**

2 empty lines using 10-point font with single spacing

First name and SURNAME*, First name and SURNAME**, First name and SURNAME***

*Institution of the Author; **Institution of the Author; ***Institution of the Author

3 empty lines using 10-point font with single spacing

Abstract: The text should begin with an abstract of a scope of not more than 10 lines (10-point font). The word ‘Abstract’ written in 10-point bold italics.

1 empty line using 10-point font with single spacing

Keywords: This section is written in the same way as the abstract section above.

1 empty line using 10-point font with single spacing

1. Introduction

The scope of the paper must not exceed 6 pages of A4 size and should have an even number of them. The paper should be created in MS Word for Windows (doc) formats.

1 empty line using 10-point font with single spacing

2. Page arrangement

Margins on the first page are as follows: left, right and bottom – 2 cm, top margin – 6 cm wide. All margins on the second and subsequent pages are 2 cm wide. The text of the paper is written in two columns with a space of 1 cm between them. An empty place should be leaved at the top of the first page.

1 empty line using 10-point font with single spacing

3. Illustrations, tables and equations

3.1. Tables

Tables ought to be numbered by Arabic figures and referred to in the text by the word, for instance: Table 1.

1 empty line using 10-point font with single spacing

Table 1. Recommended font types for tables

| Font type | Example |
|-----------------|--------------------|
| Times New Roman | 9-point / 10-point |
| Arial | 8-point / 9-point |

1 empty line using 10-point font with single spacing

3.2. Mathematical equations

Mathematical equations ought to be centrally arranged in lines and numbered by successive Arabic figures using parentheses aligned with the right-side edge of the column.

1 empty line using 10-point font with single spacing

$$u(t) = U_m \cdot \sin(\omega t + \varphi) \quad (1)$$

1 empty line using 10-point font with single spacing

3.3. Drawings, diagrams and photographs

Drawings, diagrams and photographs are considered as the same and referred to in the text using abbreviations, for example: Fig. 1.

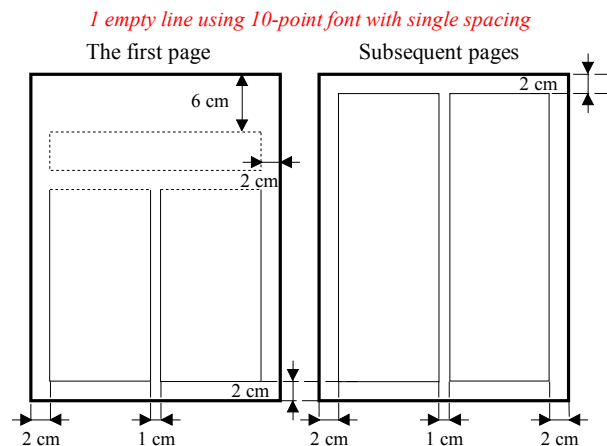


Fig. 1. Arrangement of printing area on an A-4 size page for the first and subsequent pages of manuscript

1 empty line using 10-point font with single spacing

4. Conclusions

The instruction for the preparation of final paper manuscripts for the international conference provides the essential arrangement and technical requirements for papers.

1 empty line using 10-point font with single spacing

5. References

1. Burinskiene V., Laurikaitis M. and Adliene D. Entrance Surface Dose Measurements with Thermoluminescence Dosimeters and Transmission Ionization Chamber. Proceedings of the 4th International Conference “Medical Physics in the Baltic States”, Kaunas, 2006. p. 85-87.
2. Cember H. Introduction to Health Physics. Third edition, McGraw-Hill, 1996. 393 p.